Quantum Monte Carlo Methods and Extensions for the 2D Hubbard Model

by

Joseph Paki

A dissertation submitted in partial fulfillment
of the requirements for the degree of
Doctor of Philosophy
(Physics)
in the University of Michigan
2019

Doctoral Committee:

Professor Emanuel Gull, Chair
Professor Eitan Geva
Professor Jennifer Ogilvie
Professor Kai Sun
Professor Liuyan Zhao

Joseph Paki

oryx@umich.edu

ORCID iD: 0000-0002-4936-218X

Acknowledgements

This thesis represents the end of one very long, challenging, and exciting journey and the start of another. As is usually the case in such ventures, I have quite a few people to thank for their help along the way.

I'm incredibly grateful to Dr. Emanuel Gull and his entire group for their support, guidance, and patience over the past six years. I've learned a great deal during this time about science and myself that has helped me chart a course for the future. A special shout out goes to Hanna Terletska and James LeBlanc for their endless generosity and engaging conversations.

I'd also like to thank the members of my committee, Dr. Eitan Geva, Dr. Jennifer Ogilvie, Dr. Kai Sun, and Dr. Liuyan Zhao, for their time, advice, and expertise.

No one reaches a graduate program in physics without the assistance of some wonderful teachers. Thanks to Dr. Peter Persans, Dr. Jim Napolitano, and Dr. Joel Giedt for showing me around the universe, and being there when I needed them. And I wouldn't want to skip my fourth grade math teacher, Mrs. Suppin. She is nearly single handedly the reason I can math well.

Some more gratitude goes to GEO, our graduate student union. Thanks to the union, I did not get trapped in a Parisian hospital. Solidarity forever!

And last but not least, my greatest love and thanks go out to my family, including my grandmoms, my aunt, my brother, and my parents. My mom was a die hard Trekie whose love for science fiction got me into science and whose compassion inspired me to use science for good. My dad's never ending push to get me everything I needed to succeed got me where I needed to go. It is terribly bittersweet to finish this without them, but I know they would be proud.

Live long, and prosper.

Table of Contents

List of Tables

List of Figures

List of Appendices

Abstract

This thesis will describe efforts to enhance our ability to simulate the 2D Hubbard model. Chapter 2 provides a background on the main computational techniques used throughout the work, including quantum Monte Carlo (QMC), dynamical mean field theory (DMFT), the dynamical cluster approximation (DCA), the continuous time auxiliary field algorithm (CTAUX), and the Maximum Entropy Method (MEM) for numeric analytic continuation.

Chapter 3 presents new work on applying Twisted Boundary Conditions to the DCA framework. This method is applied in a effort to access thermodynamic (i.e. large system) information about the Hubbard model without the immense computational expense required to simulate large lattices directly.

Chapter 4 describes efforts to study the extended 2D Hubbard model, which reintroduces non-local interactions between electrons that drive the formation of charge ordered phases. The work includes a thorough analysis of the phase diagram of the model away from half-filling, as well as analysis of the effect of non-local interactions on anti-ferromagnetic fluctuations and competition between the charge order and AFM states.

Chapter 5 includes a derivation of the dual fermions diagrammatic expansion and the dual fermions ladder approximation used to compute corrections to single site DMFT calculations. The method is applied to the 2D Hubbard model in order to study the evolution of its spectral function, Fermi surface, and momentum dependent mass renormalization as the temperature, interaction strength, and doping are changed. The great advantage of this method is that we are able to access arbitrary momenta throughout the Brillouin zone, in contrast to the limitation to a few cluster momenta that characterize cluster methods like DCA.

Chapter 1

Introduction

Out of the many fields that make up physics, condensed matter is rarely the one that grabs attention. Many have observed that condensed matter physics captures less prestige and interest than other fields of physics, both from the public [26] and scientists themselves [27, 1]. This may not be so surprising given popular portrayals of science - even among those who pursue a career in physics, students are often inspired more by the exotic aspects of fields such as particle physics (anti-matter!), astrophysics (black holes!), and plasma physics (big lasers! solar flares!) than by such mundane questions as the conductivity of copper. Indeed, in reference to solid state physics none other than Wolfgang Pauli once glibly wrote that, "one shouldn't wallow in dirt" [28].

In lieu of spectacle, condensed matter physicists often point to their field's role in the rapid and world changing technological developments of the 21st century. After all, despite Pauli's dismissal, most of our civilization has quite literally been built up out of dirt and the rich abundance of elements it contains [29]. Condensed matter can in some sense be thought of as the physics of construction, helping us to understand everything from the strength of steel to the clarity of glass to the magnetism of hard drives to the band gaps of semiconductors. Thanks to condensed matter physics, everyone has the power of a supercomputer in their pockets! (Imagine a physicist shaking an iPhone at a crowd of under-enthused undergraduates.)

As the last example may demonstrate, although emphasizing the concrete products of scientific investment to the public (and aspiring students) is certainly worthwhile, it is very rarely inspiring to the yet-to-be-engaged. Our species is remarkably adept at normalizing the remarkable, such that appealing to the wonders of univer-

Figure 1.1: 'Map of Physics', by Bernard Porter, 1939. Illustration of how physics was perceived in the pre-WW2 period, as a mostly disconnected realm of fields defined by various phenomena. Condensed matter might be thought of as challenging such a categorization, as it draws upon many such fields to describe the behavior of individual systems. From [1].

sally accessible commercial products is unlikely to spark the same interest as gravitational waves or supernovae. Indeed, it has been suggested that focusing on how a science adds mundane 'furniture' to our lives may in fact be counter-productive, or at least severely undercuts the promises of a 'tomorrow made better by science' found in popular science stories and science fiction [27].

Similar feelings also contributed to condensed matter's struggle for respectability within the physics community [30]. While the fields that would eventually become known as condensed matter grew tremendously in the post-war years, much of this work was geared towards applications and seen by some as a corruption of the traditional pursuit of knowledge for knowledge's sake. Furthermore, condensed matter began to challenge the reductionist view of physics, conceptualized as the dissection and categorization of physical phenomena by narrow, well-defined, and 'fundamental' fields. Some were wary that condensed matter made a mess of their hard won map that neatly carved up the physical world, Fig. 1.1.

Although the public's perception of condensed matter physics may remain lackluster, its position within physics has changed dramatically. Today condensed matter is the largest discipline in physics and produces nearly a quarter of the physics PhD's earned in the US each year [31]. While much of this growth continues to be spurred by an interest in 'mundane applications', changes in community conceptions of what physics is and surprising developments in condensed matter research have also contributed.

1.1 Quantum Condensed Matter

Currently one of the most exciting fields in physics is quantum condensed matter, which studies the many-body quantum mechanics describing materials. The goal in this field is to predict (and ideally understand) the physical phenomena a material exhibits given the types and positions of the elements it contains. For example, we would like to be able to predict whether a material is a conductor or an insulator, whether it exhibits magnetism, what its optical properties are, and what types of phase transitions occur.

In the case of a material the problem to solve consists of ions and electrons interacting via the Coulomb potential. The basic physics of this system is described by quantum mechanics via the many-body Schrodinger equation, $i\hbar\partial_t\Psi = \hat{H}\Psi$. The dominant terms in the Hamiltonian are as follows.

$$\begin{aligned} \hat{H} = &-\frac{\hbar^2}{2m_e}\sum_i \nabla_i^2 - \sum_{i,I}\frac{Z_I e^2}{|r_i - R_I|} + \frac{1}{2}\sum_{i\neq j}\frac{e^2}{|r_i - r_j|} \\ &- \sum_I \frac{\hbar^2}{2M_I}\nabla_I^2 + \frac{1}{2}\sum_{I\neq J}\frac{Z_I Z_J e^2}{|R_I - R_J|} \end{aligned} \tag{1.1}$$

In the above the electrons are denoted by lower case i and the ions by upper case I. This Hamiltonian includes, in the order the terms appear, the electrons' kinetic energy, the Coulomb potential between ions and electrons, between potential between electrons, the kinetic energy of the ions, and the potential between ions. Additional terms can be added to include interactions with external fields, and relativistic effects such as spin-orbit coupling can typically be easily included via modifications of the ion-electron potential [32]. In practice the Born-Oppenheimer approximation is often employed, in which the motion of the heavy ions is neglected. Thus, the essential problem is described by the first three terms of Eq. 1.1.

Although it is easy to write down the theory for such a condensed matter system, it is notoriously difficult to solve it. Two fundamental challenges are the Pauli exclusion principle and the interactions between electrons. The Pauli exclusion principle demands that electrons, as fermions, exist in anti-symmetrized states, such that no single particle state can hold more than one electron. This ultimately contributes to an exponential scaling in the amount of space required to simply write down a single many-body wavefunction, much less perform calculations with excited states. Meanwhile, the interactions between electrons couple their degrees of freedom, resulting in a horrifically tangled system that can only be solved exactly, even with advanced computers, in extreme limits.

Remarkably, the challenges posed by electron interactions can be overcome in many materials by a wide range of 'independent-particle' methods, such as the band theory of solids, density functional theory (DFT), and Fermi liquid theory. These methods approximate the system of interacting electrons by replacing it with a system of weakly interacting 'quasi-particles' [32, 33, 34]. On a microscopic level these quasi-particles are typically complex collective modes of the charge and spin degrees of freedom of the electrons, but at the macroscopic level these modes behave as new particles that are weakly correlated with each other and can be used to understand the material's physics.

The band theory of solids [35] is an independent particle method that enabled scientists to understand the behavior of a wide variety of crystalline systems, including most of the materials underlying modern digital technology. Band theory proceeds from the assumption that electrons travel in a static potential throughout the system, exposed only to the periodic potential generated by the attractive Coulomb potential of the ions. The interactions between electrons are ignored, and it is assumed that the system is infinite in extent. Despite these seemingly dramatic assumptions, band theory accurately describes the formation of electronic energy bands in many solids, such as silicon as shown in Fig. 1.2. It also provided the incredibly fruitful theoretical arena in which many fundamental concepts, such as band gaps, Fermi surfaces, and renormalized masses, were first understood. Furthermore, the band theory provided

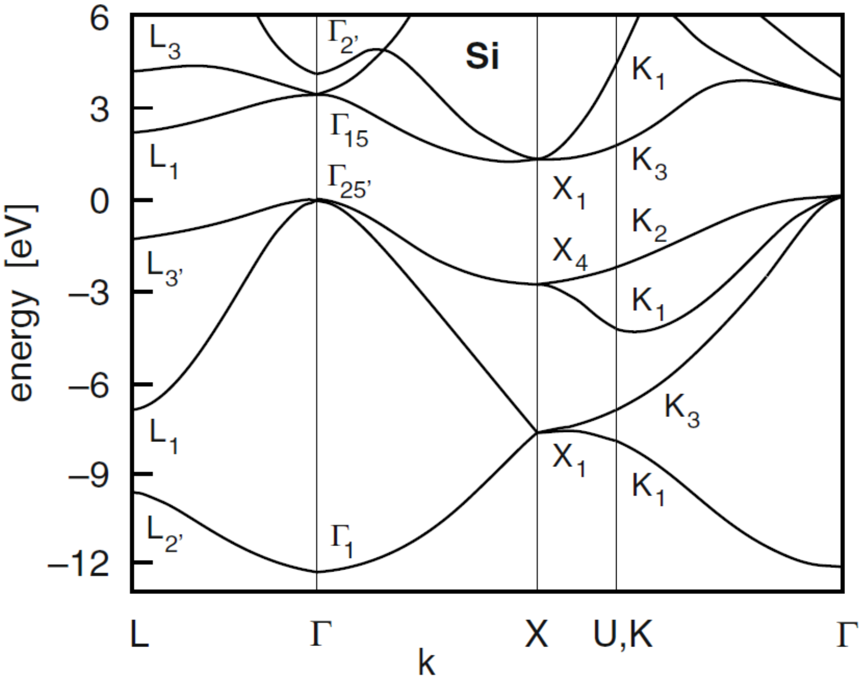

Figure 1.2: Band structure of silicon. Figure taken from [2].

a simple way to predict whether a material was an insulator or a conductor based on the number of valence electrons per unit cell. On the other hand, the failure of band theory for certain systems is one of the motivators for methods that better account for the interactions between electrons. For example, band theory predicts NiO and MgO to be metallic when experiments show them to be strong insulators even in the absence of magnetic ordering [36].

Another important example of the independent particle framework is the Fermi Liquid Theory, which was developed to describe liquid ^{3}He but can also be used to describe the physics of most metals at low temperature [3]. The theory makes use of the idea that interacting systems can often be adiabatically connected with their non-interacting limit, and thus must preserve the same conservation laws. For systems in which this applies, called Fermi liquids, the quasi-particles correspond one-to-one with the non-interacting single particle states, and their coherence is maintained by the limited phase space for scattering around the Fermi surface, as shown in Fig. 1.3. The system can then be described in single particle terms, in which the net effects of interactions are accounted for with quasi-particles that seem just like electrons with modified, or 'renormalized', masses. The Fermi liquid picture

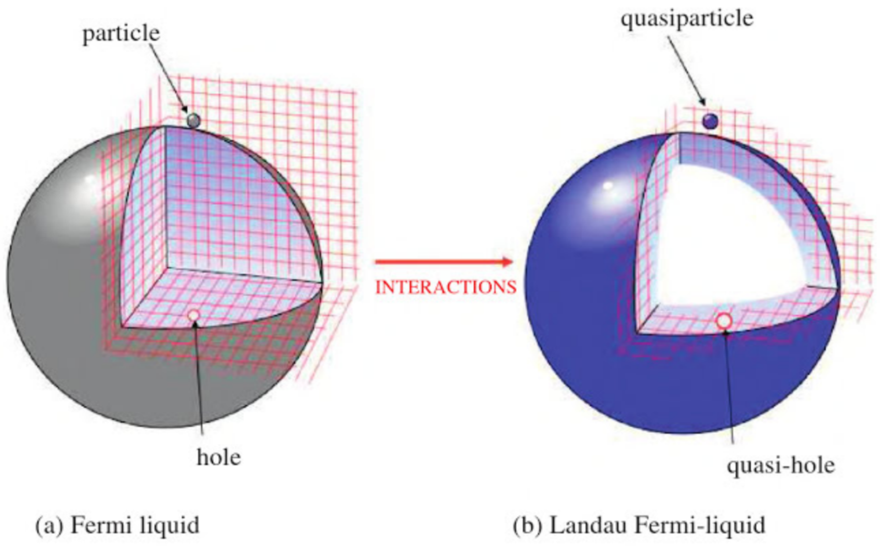

(a) Fermi liquid

(b) Landau Fermi-liquid

Figure 1.3: (a) In the non-interacting Fermi liquid, a stable particle can be created anywhere outside the Fermi surface, a stable hole excitation anywhere inside the Fermi surface. (b) When the interactions are turned on adiabatically, particle excitations near the Fermi surface adiabatically evolve into quasiparticles, with the same charge, spin and momentum. Quasiparticles and quasiholes are only well defined near the Fermi surface of the Landau Fermi liquid. Figure and caption taken from [3].

has been very successful in understanding the physics of many of the materials that enable 21st century technology. For example, it provides an appealing explanation for the seemingly unlikely success of band theory, which as previously noted entirely ignores electron interactions [35].

Another critically important independent particle method is density functional theory (DFT) [37, 38], which expresses correlation and exchange energies as functionals of the electronic density and replaces interactions between electrons with an effective potential. DFT has spread throughout many fields of science and engineering since the required computational power has become widely available, and with it scientists have made tremendous progress in simulating many different types of systems, from semi-conducting crystals to biological molecules [39].

However, as our ability to create and study ever more complex materials has developed over the past several decades, scientists have discovered a wide range of materials whose properties seem to require descriptions beyond the independent particle frameworks. As described in the next section, these systems challenge us to create new methods for tackling the quantum many-body problem.

Category	Example Materials	Phenomena
Transition Metal Oxides		
Cuprates	$La_{2-x}Sr_xCO_4$, $YB_2Cu_3O_{6+\delta}$	SC, AF, PG, CO
Manganites	$La_{1-x}Sr_xMnO_3$	FM, AF, CMR
Ruthenates	Sr_2RuO_4	SC, AF, FM
Transition Metal Dichalcogenides	MoS_2	CO, SC, FM
Heavy Fermions	$CeCu_2Si_2$, UPd_2Al_3	PG, AF, SC
Actinides / Rare-Earths	PuO_2	complex structure
Iron Pnictides	$LaOFeAs$, $Sr2ScFePO3$	AF, SC
Organic Superconductors	Bechgaard and Fabre salts, $RbCs_2C_{60}$	AF, CO, SC

Table 1.1: Brief overview of some of the systems and materials that are often referred to as 'strongly correlated'. An attempt is made here to indicate the category each system is commonly ascribed, but clean separations are often difficult due to the many overlapping properties displayed by strongly correlated materials. Furthermore, not all phenomena are exhibited by every material in a given class. The key for the phenomena is as follows: SC = Super conductivity, AF = antiferromagnetism, FM = ferromagnetism, CO = charge order, PG = Pseudo-Gap, CMR = Colossal Magnetoresistance.

1.2 Strongly Correlated Materials

The last couple of decades have seen explosive growth in the field of 'strongly correlated materials'. While there is no precise definition of what counts as a strongly correlated system, they are generally systems in which the interactions between electrons play an unusually large role in dictating their properties [36, 40, 41]. It is worthwhile noting that the descriptor 'strongly correlated' can be a bit misleading - as fermions, even non-interacting electrons are bound by the Pauli exclusion principle, which already introduces quite a bit of correlation between the particles. Strongly correlated materials are those in which the interactions between electrons introduce significant correlations in addition to the Pauli exclusion principle. One quantitative way of capturing this distinction is to compare the actual correlation in the system to what might be expected from a Hartree-Fock computation [32, 41].

Table 1.1 provides a highly abbreviated and rough overview of some of the materials commonly thought of as strongly correlated. Strongly correlated materials include the cuprates [42], heavy fermion materials [43], manganites [11], and actinides [44]. More generally, many transition metal oxides and dichalcogenides are typically classified as strongly correlated materials. [11] A common feature in many strongly correlated materials are open d or f electron shells, which confine the electrons much

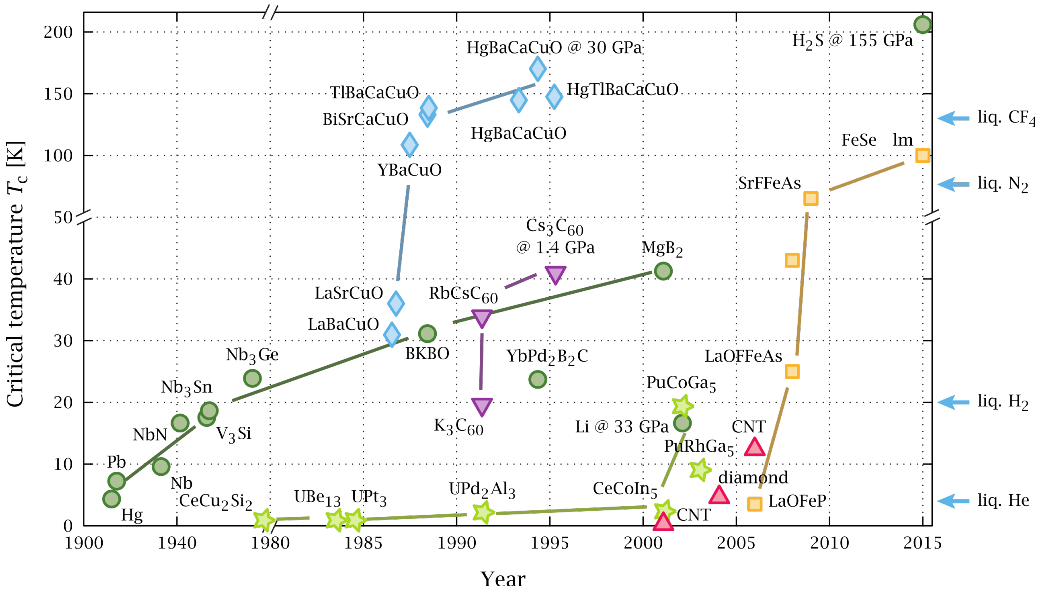

Figure 1.4: Timeline of the discovery of various superconductors. Superconductors described by BCS theory are green circles, cuprates are blue diamonds, iron based superconductors are yellow squares, organics superconductors are purple triangles, heavy fermion systems are green stars, and carbon nanotubes are red triangles. Figure from [4].

more narrowly than the s and p orbitals found earlier in the periodic table. This confinement leads to a much stronger Coulomb interaction between the electrons, such that independent and mean field methods fail to describe their dynamics [36]. This confinement is often described alternatively in terms of narrow electronic bands in momentum space, since the Fourier transform of a heavily localized quantity will typically be nearly flat in momentum space.

Strongly correlated systems are interesting because they display a great many physical phenomena, some entirely novel and some familiar with a new twist. These phenomena include high temperature superconductivity [45], pseudogaps [46], metal-insulator or Mott transitions [47], charge order [12], and various magnetic phases. Probably the most exciting development is the discovery of radically new systems that exhibit superconductivity, including not only the critical temperature, T_C, record breaking cuprates but also many organic, heavy fermion, and iron based systems. Fig. 1.4 shows the progression in T_C over the last century.

Moreover, the energy scales for the charge, spin, and orbital degrees of freedom are often comparable in these materials, such that the different phases compete with each other and give rise to complex phase diagrams. As seen in Fig. 1.5,

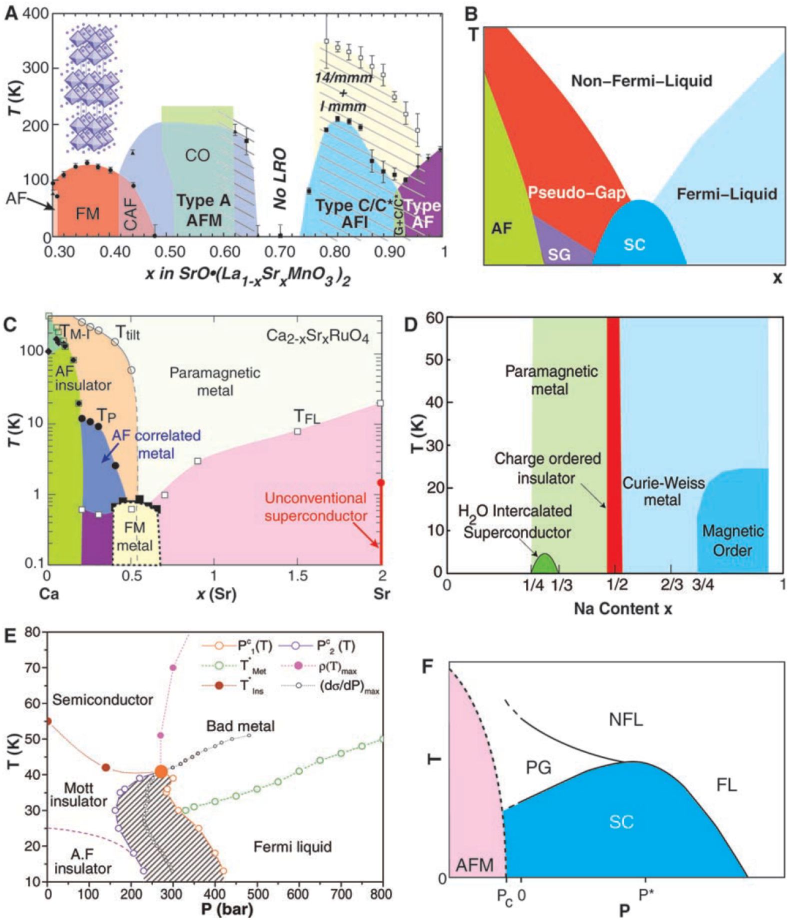

Figure 1.5: Phase diagrams of representative materials of the strongly correlated electron family (notations are standard and details can be found in the original references). (A) Temperature versus hole density phase diagram of bilayer manganites [5], including several types of antiferromagnetic (AF) phases, a ferromagnetic (FM) phase, and even a globally disordered region at $x \approx 0.75$. (B) Generic phase diagram for HTSC. SG stands for spin glass. (C) Phase diagram of single layered ruthenates [6, 7], evolving from a superconducting (SC) state at $x = 2$ to an AF insulator at $x = 0$ (x controls the bandwidth rather than the carrier density). Ruthenates are believed to be clean metals at least at large x, thus providing a family of oxides where competition and complexity can be studied with less quenched disorder than in Mn oxides. (D) Phase diagram of Co oxides [8], with SC, charge-ordered (CO), and magnetic regimes. (E) Phase diagram of the organic k-(BEDTTTF) 2Cu[N(CN)2]Cl salt [9]. The hatched region denotes the coexistence of metal and insulator phases. (F) Schematic phase diagram of the Ce-based heavy fermion materials [10]. Figure and caption taken from [11].

many strongly correlated systems move through dramatic phases changes due to very small changes in external parameters such as the applied pressure, magnetic field, temperature, or chemical doping [48]. Although the complexity of these emerging phenomena make the systems quite difficult to study, they may also provide routes for new technological applications. High temperature superconductivity and its use in generating strong magnetic fields and transmitting power are the obvious applications [49], but phenomena such as colossal magnetoresistance, the Mott metal-insulator transition, and the electronic properties of transition metal dichalcogenides [50] are promising for constructing products such as advanced sensors, flexible electronics, energy efficient windows, and next generation transistors.

The key properties that make these materials both interesting and difficult to describe theoretically are emergence and complexity [11, 51, 52]. Emergence has become a central topic in physics over the last several decades, and it represents a significant paradigm shift away from the reductionist approach that dominated the field's infancy [53]. Generally, emergence describes the appearance of behaviors and properties in a composite system that are not exhibited by the constituent parts. Classic examples include the flocking of behavior in birds, ant colonies, and superconductivity. In each of these cases, knowing a great deal about the individual parts (a bird, an ant, an electron) may not help in predicting the emergent behaviors of the collective.

One implication of emergence in quantum condensed matter is that single particle methods are doomed to failure in cases where the properties of materials are fundamentally connected to the interactions of electrons. Such properties are tied to the detailed behavior of collections of electrons, rather than the independent behaviors of electrons or even quasi-particles.

It can be very difficult to predict when a material will exhibit such strongly correlated behavior, that is, when an independent particle approach will be sufficient and when a more detailed many-body approach is required. As mentioned above, one marker is the presence of electrons in more localized orbitals (open d and f shells), since this results in a larger Coulomb integration [36]. Studying such systems requires moving beyond independent particle methods, as supported by some prominent experimental systems. For example, the most important independent particle method of the 21st century, band theory, predicts that the undoped cuprates are metals when in reality they are Mott insulators [42]. Many materials exhibit so-called 'non-Fermi liquid' behavior, such as the linear in temperature of resistivity

($\rho \propto T$) of the cuprates in the 'strange metal' phase [54, 46]. Fermi liquid theory predicts $\rho \propto T^2$. [3]

Another common phenomena in strongly correlated systems is spontaneous symmetry breaking in the spatial distribution of charges, or charge ordering. These charge order states were first observed in magnetites in 1939 [55], and are characterized periodic modulations in the electron density across the material driven by repulsive Coulomb interactions. Such states have since been found in Wigner crystals, [56, 57] manganites, [58, 59, 60, 61] cobaltates,[62] nickelates, [63, 64, 65, 66] two-dimensional organic materials, [67, 68, 69, 70] in $\mathrm{La}_{1-x}\mathrm{Sr}_x\mathrm{FeO}_3$, [71, 72] layered dichalcogenides, [73] and quasi-one-dimensional [74, 75] systems.

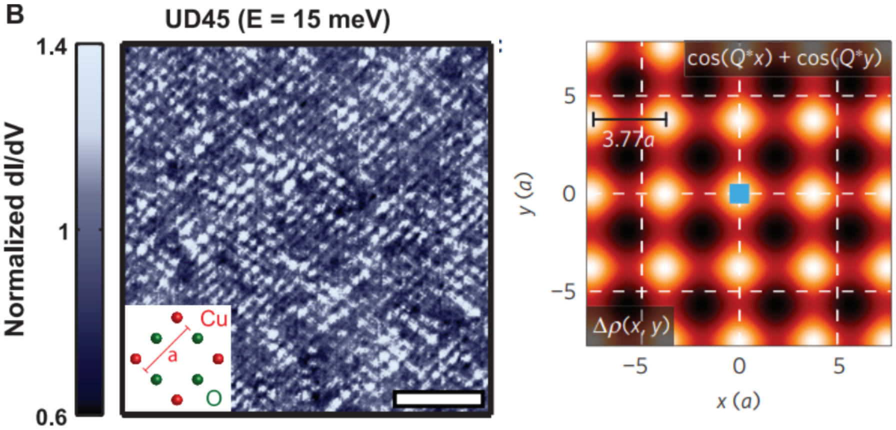

Figure 1.6: Experimental data revealing charge order in the cuprates. The left figure is an STM conductance map of at an underdoped sample of $Bi_2Sr_2CaCu_2O_{8+\delta}$ at $T = 30K$. [12] The right figure shows RXS data for an underdoped single-layer compound $Bi_2Sr_{1.2}La_{0.8}CuO_{6+\delta}$, with hole doping $p \approx 0.11$ and $T_C = 15K$. Both reveal a checkerboard charge order pattern in the electron distribution. [13]

Charge order has also recently been seen in a variety of superconducting systems, including the high T_c cuprates and organic superconductors. [12, 76, 77, 13, 78, 79, 80] In particular, charge order seem to be ubiquitous in the cuprates, and it remains an open question as to whether the phase has a common origin across the different cuprates and how the phase interacts with superconductivity. This is one of the motivations for studying the extended Hubbard model in this thesis.

1.3 Simulation Methods and the Hubbard Model

A great many theoretical techniques have been developed to study strongly correlated materials, each with different constraints on their applicability and computational advantages. Some of these methods include density functional theory (DFT) [38], dynamical mean field theory (DMFT) [81], density matrix renormalization group theory (DMRG) [82], dual fermions (DF) [83], diagrammatic Monte Carlo [84], coupled cluster theory [85], diagram approximations such as the random phase approximation (RPA) and GW methods [86], diffusion Monte Carlo [87], path integral Monte Carlo [88]. Sometimes these methods can also be fruitfully combined, such as by combining GW with DFT [38] or applying dual fermions to a DMFT starting point [89].

However, there does not exist a general purpose method that can provide accurate results for arbitrary real materials. Part of the difficulty is the complexity of real materials, which may include many electronic bands and complex arrangements of atoms. These circumstances have motivated researchers to develop model system to peal away some of the complexity of real materials while maintaining the essential electron correlations responsible for interesting behavior.

One of the most popular minimal models for studying strongly correlated behavior is the Hubbard model [90]. With the language of second quantization and a transformation to a basis of Wannier states one can write the many-body Hamiltonian 1.1 as follows [91].

$$\hat{H} = \sum_{ii'} c^{\dagger}_{i\sigma} t_{ii'} a_{i'\sigma} + \sum_{ii'jj'} U_{ii'jj'} a^{\dagger}_{i\sigma} a^{\dagger}_{i'\sigma'} a_{j'\sigma'} a_{j\sigma} \tag{1.2}$$

This Hamiltonian can be interpreted as describing electrons (corresponding to the creation and annihilation operators $c/c^{\dagger}$) moving around a lattice of sites and orbitals labeled by i via the hopping terms, $t_{ii'}$, and interacting with each other via the interaction terms, $U_{ii'jj'}$.

The original Hubbard model consisted of including only one orbital per site, nearest neighbor hoppings ($t_{ii'} = t\delta_{i+1,i'}$ and $t_{ii} = \mu$), and same site density density interactions, $U_{ii'jj'} = U\delta_{ii'jj'}$. However, even this heavily simplified model displays a complex phase diagram, including antiferromagnetic, charge order, Mott insulating, and superconducting phases [92]. In particular, the qualitative similarity between the 2D Hubbard model and the cuprates, and the hope that the model can be used to explain the superconducting pairing mechanism, have driven an immense amount of interest in the model over the last three decades. However, the model has also proven very difficult to solve in general, particularly at low temperatures and for large systems [93]. Reference [16] provides an extensive review and comparison of numerical methods used to study this simplest version of the Hubbard model.

This thesis will describe efforts to enhance our ability to simulate the 2D Hubbard model. Multiple theoretical and numerical methods are explored to address different physical phenomena (i.e. charge order) and numerical challenges (i.e. finite size effects). Chapter 2 provides a background on the main computational techniques used throughout the work, including quantum Monte Carlo (QMC), dynamical mean field theory (DMFT), the dynamical cluster approximation (DCA), the continuous time auxiliary field algorithm (CTAUX), and the Maximum Entropy Method (MEM) for numeric analytic continuation.

Chapter 3 presents new work on applying Twisted Boundary Conditions to the DCA framework. This method is applied in a effort to access thermodynamic (i.e. large system) information about the Hubbard model without the immense computational expense required to simulate large lattices directly.

Chapter 4 describes efforts to study the extended 2D Hubbard model, which reintroduces non-local interactions between electrons that drive the formation of charge ordered phases. The work includes a thorough analysis of the phase diagram of the model away from half-filling, as well as analysis of the effect of non-local interactions on anti-ferromagnetic fluctuations and competition between the charge order and AFM states.

Chapter 5 includes a derivation of the dual fermions diagrammatic expansion and the dual fermions ladder approximation used to compute corrections to single site DMFT calculations. The method is applied to the 2D Hubbard model in order to study the evolution of its spectral function, Fermi surface, and momentum dependent mass renormalization as the temperature, interaction strength, and doping are changed. The great advantage of this method is that we are able to access arbitrary momenta throughout the Brillouin zone, in contrast to the limitation to a few cluster momenta that characterize cluster methods like DCA.

1.4 Publications

This thesis is based on work from the following publications.

1. H. Terletska, T. Chen, J. Paki, and E. Gull. Charge Ordering and Nonlocal Correlations in the Doped Extended Hubbard Model. Physical Review B 97, (2018). [94]

2. Joseph Paki, Hanna Terletska, Sergei Iskakov, Emanuel Gull. Charge order and antiferromagnetism in the extended Hubbard model. Submitted to Physical Review B, arXiv:1904.02249 (2019). [95]

3. Alexander Gaenko, Andrey E Antipov, G. Carcassi, T. Chen, Xi Chen, Qiaoyuan Dong, Lukas Gamper, Jan Gukelberger, Ryo Igarashi, Sergei Iskakov, Joseph Paki, Emanuel Gull. Updated Core Libraries of the ALPS Project. Computer Physics Communications, 213 (2017). [96]

4. Markus Wallerberger, Sergei Iskakov, Alexander Gaenko, Joseph Kleinhenz, Igor Krivenko, Ryan Levy, Jia Li, Hiroshi Shinaoka, Synge Todo, Tianran Chen, Xi Chen, James P. F. LeBlanc, Joseph E. Paki, Hanna Terletska, Matthias Troyer, Emanuel Gull. Updated Core Libraries of the ALPS Project. Submitted Computer Physics Communications, arXiv:1811.08331 (2018). [97]

5. Hanna Terletska, Joseph Paki, Emanuel Gull. The Mott Transition in the 2D Extended Hubbard Model. In preparation.

Chapter 2

DMFT and Quantum Monte Carlo

In this chapter we review the numerical methods utilized in our work. We start with the overview of the the Dynamical Mean Field Theory (DMFT) [81], a self-consistency scheme that is currently one of the central methods for obtaining information about strongly correlated electron systems [36]. The primary computational challenge that arises in the DMFT framework is the need to solve a quantum impurity problem, which in this work is accomplished via Quantum Monte Carlo (QMC) and the Continuous Time Auxiliary Field algorithm (CT-AUX) [24]. This chapter presents an introduction to and schematic derivation of these methods.

This chapter also describes how to extend the CT-AUX algorithm to handle the broken symmetry phases that arise when studying charge order, [14] as well as how to apply an efficient Monte Carlo update procedure, known as submatrix updates, [25, 98] to the resulting algorithm. Finally, although these QMC methods work in the imaginary time framework, is is often desirable to obtain real frequency information that can be better related to experiments and physical intuition. The chapter closes with an introduction to the Maximum Entropy method, [99, 100] which was used to perform numerical analytic continuation to QMC data throughout this thesis.

2.1 Dynamical Mean Field Theory

The DMFT was developed as a means of investigating strongly correlated quantum lattice models that overcame the exponential barriers limiting application of methods such as exact diagonalization and lattice Monte Carlo [81]. Exact diagonalization methods, while numerically exact, become computationally intractable for even a small number of system sites. Traditional Monte Carlo methods, which directly sample Feynman diagrams, suffer from a fermion sign problem (discussed later in this chapter) that prevents access to interesting parameter regimes, such as larger interaction strengths or lower temperatures [32, 101, 16].

DMFT attempts to overcome these challenges by mapping an interacting lattice model onto an impurity embedded in an effective medium in a self-consistent manner. While the lattice model is infinite in extent and may contain correlations over all length scales, the impurity model is much simpler, consisting of a small number of sites (or an impurity cluster) coupled to a bath of non-interacting states. The basic idea is to treat the interactions between particles on the cluster exactly and choose the coupling between the cluster and bath sites in such a way as to mimic the effects of the rest of the lattice in the original problem on the cluster. Thus, local correlations (those constrained to lengths scales within the cluster) are treated non-perturbatively, while longer range correlations are treated in a mean field manner [36].

The impetus for the development of DMFT came from the observation that in the limit of infinite dimensions, $d \to \infty$, the self-energy of a lattice model becomes momentum independent, that is, $\Sigma(\omega, k) \to \Sigma(\omega)$ [102, 41]. This is equivalent to the statement that in infinite dimensions, all correlations become local, i.e. the physics of the system is dictated by the interactions between particles on the same lattice sites. Although realistic systems are certainly not infinite dimensional, the idea of treating long range correlations via mean field in exchange for simulating short range correlations exactly caught on and lead to the development of single-site DMFT [81, 36]. In this theory a single site from the original lattice problem is coupled to a non-interacting bath, and a set of self-consistency conditions assert that quantities calculated from this impurity problem (Green's functions, self-energies, etc.) will match the actual local quantities on the full lattice problem.

Although successful, the single-site DMFT was limited in its application to systems where only local quantum fluctuations were important. This motivated the development of DMFT extensions where non-local correlations could be introduced in a controlled manner [14]. The obvious path forward was to replace the single site impurity with a small cluster of sites, and this eventually led to the development of cluster methods such as the Dynamical Cluster Approximation (DCA) and the Cellular DMFT (CDMFT). Here we will focus on the DCA, in which self-consistency conditions demand that quantities calculated on the cluster impurity agree with the corresponding quantities on the full lattice at some subset of momentum space points, K.

2.2 Dynamical Cluster Approximation

We will now describe how DCA is derived for the general 2D extended Hubbard model [103]. The derivation is relevant to all of the work presented in this thesis, as the various models studies (i.e. Hubbard model with only local interactions, the extended Hubbard model with nearest neighbor interactions) are simply special cases of the general extended Hubbard model, as determined by the interaction coefficients $U_{ij}^{\sigma\sigma'}$ and the hopping matrix t_{ij}. Furthermore, the single site DMFT, which is the starting point for the dual fermions work presented in Chapter 5, is just the $N_C = 1$ limit of DCA. This derivation follows that of Maier [14].

The general extended Hubbard model is described by the following lattice Hamiltonian.

$$H = \sum_{ij\sigma} t_{ij} c_{i\sigma}^{\dagger} c_{j\sigma} + \frac{1}{2} \sum_{ij\sigma\sigma'} U_{ij}^{\sigma\sigma'} n_{i\sigma} n_{j\sigma'} \tag{2.1}$$

In this Hamiltonian $n_{i\sigma} = c_{i\sigma}^{\dagger} c_{i\sigma}$ is the number operator for each lattice site and $c_{i\sigma}^{\dagger}$, $c_{i\sigma}$ are electron creation and annihilation operators. Parameter t_{ij} describes how electrons hop between lattice sites, $U_{ij}^{\sigma\sigma'}$ describe how electrons interact with each other, and $t_{ii} = \mu$ is the chemical potential that controls the equilibrium number of electrons on the lattice.

The starting point for DCA [14] is to split the lattice into clusters of N_C sites, each with linear dimension L_C. As shown in Fig. 2.1, the real and momentum space coordinates are split into inter- and intra-cluster coordinates, $\mathbf{x} = \mathbf{X} + \tilde{\mathbf{x}}$ and $\mathbf{k} = \mathbf{K} + \tilde{\mathbf{k}}$. We will wind up relating cluster quantities calculated at the cluster momenta $\mathbf{K}$ to lattice quantities at the same subset of momentum space points.

One of our central objectives in many-body calculations is to obtain the single-particle Green's functions, G, and self-energies, Σ, which tell us how particles propagate and interact through the system. In the imaginary time formalism these Green's functions are defined as follows.

$$G_{ij\sigma}(\tau) = -\langle T_{\tau} c_{i\sigma} c_{j\sigma}^{\dagger} \rangle \tag{2.2}$$

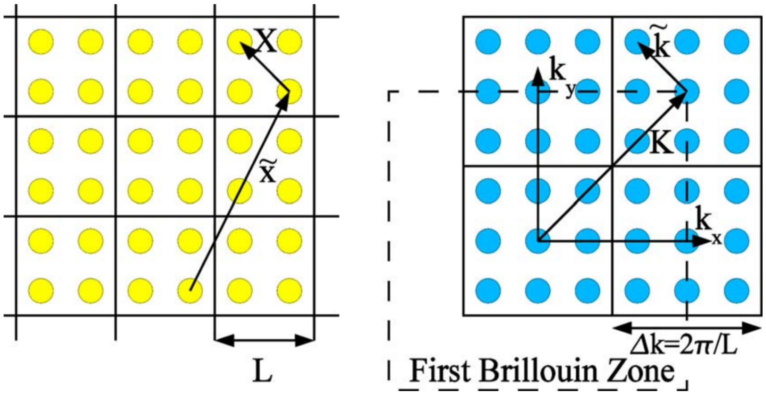

Figure 2.1: Example of how the real space (left) and momentum space (right) coordinates are defined in DCA for $N_C = 4$. The positions of lattice sites within a cluster, $\mathbf{X}$, are reciprocal to the momenta at which cluster quantities are calculated, $\mathbf{K}$. The superlattice vectors, $\tilde{\mathbf{x}}$, are reciprocal to the momentum vectors that are averaged over (i.e. coarse grained) in the DCA algorithm, $\tilde{\mathbf{k}}$. Figure taken from [14].

$$G_{ij\sigma} = \int_0^\beta d\tau e^{i\omega_n \tau} G_{ij\sigma}(\tau) \tag{2.3}$$

The Fourier transform of the imaginary time Green's function involves the fermionic Matsubara frequencies, $\omega_n = \frac{(2n+1)\pi}{\beta}$, where $\beta = 1/T$ is the inverse temperature [3].

2.2.1 Diagrammatic Derivation

One way of obtaining the DCA approximation for these functions is by studying the Luttinger-Ward functional, $\Phi[\mathbf{G}, \mathbf{U}]$, which depends on both the Green's function and the base interactions, $\mathbf{U}$. The functional is defined as the sum of all closed, bold, 2 particle irreducible (2PI) Feynman diagrams generated by the Hamiltonian. By 'bold', we mean that the Green's function lines appearing in the diagrams are fully interacting, or 'dressed', Green's functions, G, rather than the non-interacting Green's functions, G_0. 2PI simply means that only diagrams that can not be broken up by cutting 2 Green's function lines are included, which implies that derivatives of the functional will result in contributions to the single particle self-energy, Σ. An example of a 2PI diagram is shown in Fig. 2.2. The Luttinger-Ward functional is often used as a starting place for Green's function approximations because it provides some guarantees with respect to obeying Ward identities (i.e. conservation laws) [104, 14].

The grand potential function, Ω, is often a starting point in statistical mechanics for calculating the thermodynamic properties of a system. It can be expressed in terms of Φ via a linked cluster expansion as follows [3].

$$\Omega[G, U] = -k_B T\{\Phi[G, U] - \mathrm{Tr}\ln(-G) - \mathrm{Tr}(\Sigma G)\} \tag{2.4}$$

It can be shown that in order for physical quantities calculated from derivatives of Ω to be consistent with those computed from G, we need Ω to be stationary with respect to G.

$$\begin{aligned} \frac{\delta\Omega}{\delta G} &= -k_B T\left(\frac{\delta\Phi}{\delta G} + G^{-1} - \Sigma - \frac{\delta\Sigma}{\delta G}G\right) \\ &= -k_B T\left(\frac{\delta\Phi}{\delta G} - \Sigma\right) \\ &= 0 \end{aligned} \tag{2.5}$$

Where we have used the Dyson equation, $G_0^{-1} - G^{-1} = \Sigma$. Thus, we see that stationarity requires that,

$$G_0^{-1} - G^{-1} = \Sigma = \frac{\delta\Phi}{\delta G} \tag{2.6}$$

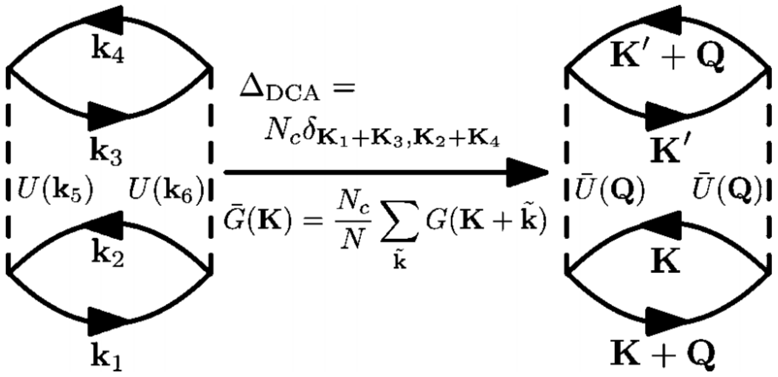

Figure 2.2: Example of how the DCA approximation modifies contributions to the Φ functional. On the right is a second order diagram that contributes to Φ for the lattice Hubbard model. On the right is the result from coarse graining and relaxing the momentum conservation constraints at the vertices. Figure taken from [14].

An example of a diagram that contributes to Φ is shown in Fig. 2.2. We can use the momentum space Feynman rules to translate this diagram, D, into a mathematical expression [3]. Note that we suppress frequency and spin factors in order to focus on the momentum dependence.

$$\begin{aligned} D \propto \frac{1}{N^6} \sum_{k_1k_2k_3k_4k_5k_6} & G(k_1)G(k_2)U(k_5)U(k_6)G(k_3)G(k_4) \\ & \cdot \Delta(-k_1, k_2, -k_5)\Delta(k_1, -k_2, -k_6)\Delta(k_5, -k_3, k_4)\Delta(k_6, k_3, -k_4) \end{aligned} \tag{2.7}$$

The Laue function, Δ, is responsible for enforcing momentum conservation at each of the vertices. Its usual definition is

$$\Delta(k_1, \dots, k_n) = \sum_x e^{ix(k_1+\dots+k_n)} = N\delta_{k_1+\dots+k_n}. \tag{2.8}$$

The fundamental approximation in DCA is to relax the momentum conservation requirement. Instead of requiring that the full lattice momenta, $k = K + \tilde{k}$, are conserved at each vertex, DCA requires only that the cluster momenta, K, are conserved. The DCA Laue function is thus defined as

$$\Delta_{DCA}(K_1 + \tilde{k}_1, \dots, K_n + \tilde{k}_n) = N_C\delta_{K_1+\dots+K_n}, \tag{2.9}$$

where N_C is the size of the cluster, and also the number of cluster momenta. If we use this definition for the Laue function to calculate diagrams, then the sums in expressions such as 2.8 can be broken up into sums over cluster momenta K and $\tilde{k}$.

$$\frac{1}{N}\sum_{k_1} G(k_1) = \frac{1}{N_C}\sum_{K_1} \frac{N_C}{N} \sum_{\tilde{k}_1} G(K_1 + \tilde{k}_1) \tag{2.10}$$

The sums over $\tilde{k}$ can now be performed freely. Thus, the DCA approximation amounts to replacing the Green's function and interaction lines in Φ diagrams with new coarse-grained, or momentum averaged, functions $\bar{G}$ and $\bar{U}$.

$$\bar{G}(K) = \frac{N_C}{N}\sum_{\tilde{k}} G(K + \tilde{k}) \tag{2.11}$$

$$\bar{U}(K) = \frac{N_C}{N}\sum_{\tilde{k}} U(K + \tilde{k}) \tag{2.12}$$

We can then define the cluster self-energy, Σ_C, as follows.

$$\Sigma_C(K) = \frac{\delta\Phi[\bar{G},\bar{U}]}{\delta\bar{G}(K)} \tag{2.13}$$

We can also define the DCA approximation of the lattice grand potential, $\Omega[\bar{G},\bar{U}]$. This functional should be stationary we respect to the true lattice Green's function, $G(k = K + \tilde{k})$.

$$\begin{aligned}\frac{\Omega[\bar{G}(K),\bar{U}(K)]}{\delta G(k)} &= -k_B T\left(\frac{\Phi[\bar{G}(K),\bar{U}(K)]}{\delta G(k)} + \frac{1}{\bar{G}(K)}\frac{\delta\bar{G}(K)}{\delta G} - \Sigma\frac{\delta\bar{G}(K)}{\delta G} - \frac{1}{\bar{G}(K)}\frac{\delta\bar{G}(K)}{\delta G}\right)\\ &= -k_B T\left(\Sigma_C(K) - \Sigma(k)\right) = 0\end{aligned} \tag{2.14}$$

This means that the lattice self-energy is assuming to be equal to the cluster self-energy in the DCA approximation, $\Sigma(k) = \Sigma_C(K)$. In other words, the lattice self-energy is a piece-wise constant function in DCA, with the value at momentum k set equal to the value of the cluster self-energy at the closest K point. We can then use the Dyson equation to define the following self-consistency condition for the coarse grained Green's function, $\bar{G}$.

$$\bar{G}(K) = \frac{N_C}{N}\sum_{\tilde{k}} G(K+\tilde{k}) = \frac{N_C}{N}\sum_{\tilde{k}}\left(G_0^{-1}(K+\tilde{k}) - \Sigma_C(K)\right)^{-1} \tag{2.15}$$

Where the non-interacting lattice Green's function is $G_0^{-1}(K+\tilde{k}) = \left(z - \epsilon_{K+\tilde{k}} + \mu\right)^{-1}$, where $\epsilon_{K+\tilde{k}}$ is the lattice dispersion and z is the frequency, in either real or Matsubara frequency.

2.2.2 Effective Cluster Action

We will now express our DCA framework in terms of an effective action, as is needed for the application of Quantum Monte Carlo methods such as CT-AUX [105]. In the last section we saw that the Green's function of the cluster, $G_C(K)$, is equal to the coarse grained lattice Green's, $\bar{G}(K)$. This allows us to define the non-interacting Green's function on the cluster, $\mathcal{G}(K)$.

$$G_C(K) = \bar{G}(K) = \left(\mathcal{G}^{-1}(K) - \Sigma_C(K)\right)^{-1} \tag{2.16}$$

The action corresponding to a cluster model, S_C, with non-interacting Green's function $\mathcal{G}$ and bare interaction parameters $\bar{U}$ is given by

$$\begin{aligned} S_C[c, c^*] = &- \int_0^\beta d\tau \int_0^\beta d\tau' \sum_{ij\sigma} c^*_{i\sigma}(\tau)\mathcal{G}_{ij\sigma}(\tau - \tau')c_{j\sigma}(\tau') \\ &+ \frac{1}{2}\int_0^\beta d\tau \sum_{ij\sigma\sigma'} \bar{U}^{\sigma\sigma'}_{ij} c^*_{i\sigma}(\tau)c^*_{j\sigma'}(\tau)c_{j\sigma'}(\tau)c_{i\sigma}(\tau) \end{aligned} \tag{2.17}$$

It is important to note that $\mathcal{G}(K)$ is not the same thing as the lattice non-interacting Green's function, $G_0(k)$. The $\mathcal{G}(K)$ incorporates both the free propagation of electrons in the cluster as well as the effects of the self-consistency constraints from DCA. This is easier to understand if we look at the cluster Hamiltonian corresponding to the action 2.17. It can be shown that the Hamiltonian for the cluster, $\mathcal{H}_C$ which fulfills the DCA relationships is as follows [14].

$$\begin{aligned} \mathcal{H}_C &= H_{C,0} + H_{C,I} \\ &= \sum_{K\sigma}(\bar{\epsilon}_K - \mu)c^\dagger_{K\sigma}c_{K\sigma} + \sum_{k\sigma}\lambda_{k\sigma}a^\dagger_{k\sigma}a_{k\sigma} \\ &+ \sum_{K\tilde{k}\sigma}\left(V_K(\tilde{k})c^\dagger_{K\sigma}a_{K+\tilde{k}\sigma} + H.C.\right) \\ &+ \sum_{KK'Q\sigma\sigma'} \frac{\bar{U}^{\sigma\sigma'}(Q)}{2N_C} c^\dagger_{K+Q\sigma}c^\dagger_{K'-Q\sigma'}c_{K'\sigma}c_{K\sigma} \end{aligned} \tag{2.18}$$

This effective Hamiltonian, in which the $c/c^\dagger$ are now creation and annihilation operators, gives us a clear physical interpretation for the DCA algorithm. We are replacing our original lattice problem with an Anderson impurity problem, [106] a cluster of sites coupled to a non-interacting bath. The cluster is embedded in this medium is such a way as to match the lattice coarse grained Green's function with the cluster Green's function. We can think of adjusting the coupling between the cluster and the bath, V_K, and the bath energy levels, $\lambda_{k\sigma}$, until we achieve a $\mathcal{G}$ and Σ_C that fulfills the DCA self-consistency conditions. However, this is only required for methods that need an explicit form for the non-interacting cluster Hamiltonian, $H_{C,0}$, such as exact diagonalization. In the next section and the derivation for CT-AUX, we'll see that we only need to choose and adjust $\mathcal{G}$ directly, without reference to the underlying Hamiltonian model, in order to achieve self-consistency.

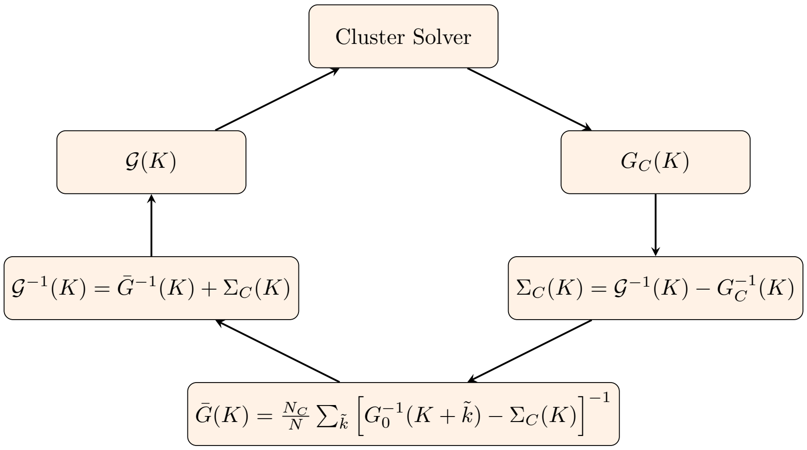

Figure 2.3: The DCA self-consistency loop. Starting with a guess for the non-interacting cluster Green's function, $\mathcal{G}$, we iteratively solve the impurity problem to obtain the cluster Green's function and check if it agrees with the coarse grained lattice Green's function, $\bar{G}$. If they do not agree, we recompute $\mathcal{G}$ and try again.

2.2.3 Self-consistency Loop

At this point the lattice problem, which has an infinite number of degrees of freedom, as been reduced to a cluster problem with some self-consistency constraints and a finite number of degrees of freedom. Our goal is to find a non-interacting cluster Green's function, $\mathcal{G}$, such that when we solve the cluster problem described by 2.17 we obtain a cluster Green's function that agrees with the coarse grained lattice Green's function. To recap, the basic self-consistency conditions are as follows, with energy dependence, z, restored.

$$G_C(z,K) = \left(\mathcal{G}^{-1}(z,K) + \Sigma_C(z,K)\right)^{-1} \tag{2.19}$$

$$\bar{G}(z,K) = \frac{N_C}{N}\sum_{\tilde{k}}\left(G_0^{-1}(z,K+\tilde{k}) - \Sigma_C(z,K)\right)^{-1} \tag{2.20}$$

$$G_C(z,K) = \bar{G}(z,K) \tag{2.21}$$

This constitutes a complex set of nonlinear equations that we can solve via a self-consistency cycle that we repeat until convergence is reached. Here are the steps in this process [14].

1. Guess a starting $\mathcal{G}$. This can be anything, although convergence is often sped up by guessing well. Starting with the lattice free Green's function or the atomic solution are common starting choices. In the case of competing broken symmetry phases, we can also modify our starting $\mathcal{G}$ to probe for stable phases.
2. Solve the cluster problem with $\mathcal{G}$ as the input free cluster Green's function, obtaining the full cluster Green's function G_C.
3. Compute the cluster self-energy, $\Sigma_C = \mathcal{G}^{-1} - G_C^{-1}$. We can then compute the coarse grained lattice Green's function, $\bar{G}$.
4. Check if $\bar{G} = G_C$ up to some small tolerance. If self-consistency has not been reached, compute a new $\mathcal{G} = (\bar{G}^{-1} + \Sigma_C)^{-1}$ and repeat the cycle.

This process is depicted in Fig. 2.3. Although the problem had been made much simpler by restricting the degrees of freedom to the cluster, solving the interacting cluster problem is still a very challenging task. Later we will discuss how to use Quantum Monte Carlo, via the CT-AUX algorithm, to efficiently solve the cluster problem.

2.2.4 Renormalization of Interaction

We have seen that the effective cluster problem we need to solve in DCA involves coarse grained interaction coefficients, $\bar{U}(K)$.

$$\bar{U}(K) = \frac{N_C}{N} \sum_{\tilde{k}} U(K + \tilde{k}) \tag{2.22}$$

It is important to understand how to map the lattice interaction parameters, U_{ij}, from the Hamiltonian given by Eq. 2.1 to the cluster interaction parameters used in the cluster solver, $\bar{U}(X)$, which typically works in real space. If we assume that the lattice interactions are transitionally invariant, then we can set $U(x) = U(X + \tilde{x}) = U_{ij}$, where $x = |x_i - x_j|$. We can then use cluster Fourier transforms to write $\bar{U}(X)$ in terms of $U(x)$.

$$
\begin{aligned}
\bar{U}(X') &= \frac{1}{N_C}\sum_{K} e^{iK\cdot X'}\bar{U}(K) \\
&= \frac{1}{N_C}\sum_{K} e^{iK\cdot X'}\frac{N_C}{N}\sum_{\tilde{k}}\sum_{X\tilde{x}} e^{-i(K+\tilde{k})\cdot X} e^{-k\tilde{k}\cdot\tilde{x}}U(x) \\
&= \frac{1}{N}\sum_{X\tilde{x}}\sum_{K} e^{iK\cdot(X'-X)}\sum_{\tilde{k}} e^{-i\tilde{k}\cdot(X+\tilde{x})}U(x) \\
&= \frac{N_C}{N}\sum_{\tilde{k}}\sum_{\tilde{x}} e^{-i\tilde{k}\cdot(X+\tilde{x})}U(x)
\end{aligned}
\tag{2.23}
$$

Where we have used that $\sum_K e^{iK\cdot(X'-X)} = N_C\delta_{X',X}$. This thesis will deal will Hubbard models with both on site, $U(x=0)=U$, and nearest neighbor, $U(x=\hat{i})=V$, interactions. ($\hat{i}$ is a unit vector to any of a site's neighbors.) The cluster equivalents of these terms, $\bar{U}(X'=0)$ and $\bar{U}(X'=\hat{i})$, take on the following forms.

$$
\begin{aligned}
\bar{U}(X'=0) &= \frac{N_C}{N}\sum_{\tilde{k}}\sum_{\tilde{x}} e^{i\tilde{k}\cdot\tilde{x}}U(\tilde{x}) \\
&= \frac{N_C}{N}\sum_{\tilde{k}} U(x=0) \\
&= U
\end{aligned}
\tag{2.24}
$$

$$
\begin{aligned}
\bar{V} &= \bar{U}(X'=\hat{i}) \\
&= \frac{N_C}{N}\sum_{\tilde{k}}\sum_{\tilde{x}} e^{i\tilde{k}\cdot(\hat{i}+\tilde{x})}U(\hat{i}+\tilde{x}) \\
&= \frac{N_C}{N}\sum_{\tilde{k}\cdot\hat{i}} e^{-i\tilde{k}\cdot\hat{i}}U(x=\hat{i}) \\
&= V\frac{N_C}{N}\sum_{\tilde{k}} e^{-i\tilde{k}\cdot\hat{i}}
\end{aligned}
\tag{2.25}
$$

Where we have assumed that our Hamiltonian does not include long range interactions between the same site in different clusters, $U(i+\tilde{x}) = U(i)\delta_{0,\tilde{x}}$. Thus, we see that the local interactions are that same for the lattice and cluster, but the nearest neighbor interactions are modified. We can carry out the calculation for $\bar{V}$.

$$
\begin{aligned}
\bar{V} &= V\frac{N_C}{N}\frac{N}{(2\pi)^d}\sum_{\tilde{k}} e^{i\tilde{k}\cdot\hat{i}}\frac{(2\pi)^d}{N} \\
&= V\frac{N_C}{(2\pi)^d}\prod_j \int_{\tilde{k}_j=-\frac{\pi}{L_C}}^{\frac{\pi}{L_C}} e^{i\tilde{k}_i} d\tilde{k}_j \\
&= V\frac{N_C}{2\pi L_C^{d-1}}\int_{\tilde{k}_i=-\frac{\pi}{L_C}}^{\frac{\pi}{L_C}} e^{i\tilde{k}_i} d\tilde{k}_i \\
&= V\frac{L_C}{\pi}\sin\left(\frac{\pi}{L_C}\right)
\end{aligned}
\tag{2.26}
$$

Where L_C is the linear dimension of the clusters. We see that as the cluster sizes become very large, the cluster interaction parameters approach those of the lattice, as expected. This interaction renormalization is important when applying DCA to model Hamiltonian that include non-local interactions, such as for the charge order model studied in Chapter 4 [107, 108].

2.3 CT-AUX Algorithm

This section describes the Continuous Time Auxiliary Field (CT-AUX) algorithm that is used as the DMFT impurity solver throughout this work [105, 23]. We'll derive the algorithm for the single-band 2D extended Hubbard model, described by the following Hamiltonian.

$$
H = H_0 + H_{int} \tag{2.27}
$$

$$
H_0 = -t\sum_{\langle ij\rangle\sigma}\left(c_i^\dagger c_j + h.c.\right) - \mu\sum_{i\sigma} n_{i\sigma} + \frac{K}{\beta} \tag{2.28}
$$

$$
H_{int} = \frac{1}{2}\sum_{ij\sigma\sigma'} U_{ij}^{\sigma\sigma'}\left(n_{i\sigma}n_{j\sigma'} - \frac{n_{i\sigma}+n_{j\sigma'}}{2}\right) - \frac{K}{\beta} \tag{2.29}
$$

The parameters t, μ, $U_{ij}^{\sigma\sigma'}$ are the terms that describe electrons hopping between lattice sites, the chemical potential, and the density-density interactions between electrons, respectively. The symbol $\langle ij\rangle$ means that electrons can only hop between nearest neighbor sites. The constant $\frac{K}{\beta}$ has been introduced for future convenience.

In this thesis we study models in which electrons can interact with energy U if they are on the same site, and with energy V if they are on neighboring sites.

$$U_{ij}^{\sigma\sigma'} = \begin{cases} U & i = j,\ \sigma = -\sigma' \\ V & \langle ij \rangle \\ 0 & otherwise \end{cases} \tag{2.30}$$

The Hamiltonian for a given system can be used to construct the partition function, $Z = \mathrm{Tr}\, e^{-\beta H} = \mathrm{Tr}\, e^{-\beta(H_0 + H_{int})}$, where we have separated the Hamiltonian into interacting, H_{int}, and non-interacting parts, H_0.

We are now going to use the interaction picture to expand the partition function into a series. In the interaction picture, time dependent operators are defined as

$$O(\tau) = e^{\tau H_0} O e^{-\tau H_0} \tag{2.31}$$

Now we define a new operator, $A(\beta)$.

$$A(\beta) = e^{\beta H_0} e^{-\beta H} \tag{2.32}$$

$$Z = \mathrm{Tr}\, e^{-\beta H} = \mathrm{Tr}\left[e^{-\beta H_0} A(\beta)\right] \tag{2.33}$$

If we differentiate $A(\beta)$, we get

$$\frac{dA}{d\beta} = H_0 A(\beta) - H A(\beta) = -H_{int}(\beta) A(\beta) \tag{2.34}$$

$$A(\beta) = T_\tau e^{-\int_0^\beta d\tau H_{int}(\tau)} \tag{2.35}$$

Where T_τ is the time ordering symbol. Inserting this into the partition function yields,

$$Z = \mathrm{Tr}\left[e^{-\beta H_0} T_\tau e^{-\int_0^\beta d\tau H_U(\tau)}\right] \tag{2.36}$$

Now we expand the exponential and take care of the time ordering explicitly in the integrals and get

$$Z = \sum_{k=0}^{\infty} \int_0^\beta d\tau_1 \dots \int_{\tau_{k-1}}^{\beta} \mathrm{Tr}\left[e^{-\beta H_0} e^{\tau_k H_0}(-H_{int}) \dots e^{-(\tau_2-\tau_1)H_0}(-H_{int}) e^{-\tau_1 H_0}\right]. \tag{2.37}$$

We now rewrite the interaction term, H_{int}.

$$-H_{int} = \left(\frac{K}{4\beta N_c^2}\right) \sum_{ij\sigma\sigma'} \left(1 - \frac{4\beta N_c^2}{2K} U_{ij}^{\sigma\sigma'} \left(n_{i\sigma} n_{j\sigma'} - \frac{n_{i\sigma} - n_{j\sigma'}}{2}\right)\right) \tag{2.38}$$

Where N_c is the number of cluster sites. To each term in this sum we can apply the following Hubbard-Stratonivich transformation, [23] which allows us to replace quadratic terms in the creation and annihilation operators in exchange for introducing new, classical auxiliary spin variables, s.

$$1 - C\left(n_{i\sigma} n_{j\sigma'} - \frac{n_{i\sigma} - n_{j\sigma'}}{2}\right) = \frac{1}{2} \sum_{s=\pm 1} e^{\gamma_{ij}^{\sigma\sigma'} s(n_{i\sigma} - n_{j\sigma'})} \tag{2.39}$$

$$\gamma_{ij}^{\sigma\sigma'} = 1 + \frac{C}{2} \tag{2.40}$$

Each of the operators $n_{i\sigma}$ can only assume the values zero or one, so one can directly verify this relation for the four possible local states (possible occupations of site i). Applying this transformation to H_{int} yields the following.

$$-H_{int} = \left(\frac{K}{4\beta N_c^2}\right) \sum_{ij\sigma\sigma'} \left(\frac{1}{2} \sum_{s=\pm 1} e^{\gamma_{ij}^{\sigma\sigma'} s(n_{i\sigma} - n_{j\sigma'})}\right) \tag{2.41}$$

Where for the 2D extended Hubbard model the $\gamma_{ij}^{\sigma\sigma'}$ are given by

$$\cosh(\gamma_{ij}^{\sigma\sigma'}) = \left(\begin{array}{cc} 1 + \frac{\beta N_c^2 U}{K} & i = j,\ \sigma = -\sigma' \\ 1 + \frac{\beta N_c^2 V}{K} & \langle ij \rangle \\ 1 & otherwise \end{array}\right. \tag{2.42}$$

Plugging this into the partition function yields,

$$Z = \sum_{k=0}^{\infty} \sum_{\substack{s_l = \pm 1 \\ l=1,\dots,k}} \sum_{\substack{i_l, j_l, \sigma_l, \sigma_l' \\ l=1,\dots,k}} \int_0^\beta d\tau_1 \dots \int_{\tau_{k-1}}^{\beta} \left(\frac{K}{8\beta N_c^2}\right)^k Z_k(\{s_l, \tau_l, i_l, j_l, \sigma_l, \sigma_l'\}), \tag{2.43}$$

where

$$Z_k(\{s_l,\tau_l,i_l,j_l,\sigma_l,\sigma'_l\}) = \mathrm{Tr}\left[e^{-\beta H_0}\prod_{l=k}^{1} e^{\tau_l H_0} e^{\gamma_{i_l j_l}^{\sigma_l\sigma'_l} s_l (n_{i_l\sigma_l} - n_{j_l\sigma'_l})} e^{-\tau_l H_0}\right]. \tag{2.44}$$

We can apply the identity

$$e^{\gamma_{ij}^{\sigma\sigma'} s n_{i\sigma}} = e^{\gamma_{ij}^{\sigma\sigma'} s} - \left(e^{\gamma_{ij}^{\sigma\sigma'}} - 1\right) c_{i\sigma} c^{\dagger}_{i\sigma} \tag{2.45}$$

to rewrite $Z_k(\{s_l,\tau_l,i_l,j_l,\sigma_l,\sigma'_l\})$ as a quantity that can be evaluated via Wick's theorem. Since $n_{i\sigma}$ and $n_{j\sigma'}$ commute except when $i = j$ and $\sigma = \sigma'$ (which is prohibited by the form of the interaction, $U_{ii}^{\sigma\sigma} = 0$), we obtain

$$\begin{aligned} Z_k(\{s_l,\tau_l,i_l,j_l,\sigma_l,\sigma'_l\}) = \mathrm{Tr}\Bigg[& e^{-\beta H_0}\prod_{l=k}^{1} e^{\tau_l H_0}\left(e^{\gamma_{i_l j_l}^{\sigma_l\sigma'_l} s_l} - \left(e^{\gamma_{i_l j_l}^{\sigma_l\sigma'_l}} - 1\right) c_{i_l\sigma_l} c^{\dagger}_{i_l\sigma_l}\right) \\ & \times \left(e^{-\gamma_{i_l j_l}^{\sigma_l\sigma'_l} s_l} - \left(e^{-\gamma_{i_l j_l}^{\sigma_l\sigma'_l}} - 1\right) c_{j_l\sigma'_l} c^{\dagger}_{j_l\sigma'_l}\right) e^{-\tau_l H_0}\Bigg] \end{aligned} \tag{2.46}$$

The above trace is performed against the non-interacting Hamiltonian, H_0, and so via Wick's theorem will result in a combination of non-interacting Green's functions, $g_{i_l j_l}^{\sigma_l\sigma'_m}$, or rather, the Green's functions corresponding to propagation under H_0.

$$g_{i_l j_l}^{\sigma_l\sigma'_m}(\tau_l - \tau_m) = \langle T_\tau c_{i_l\sigma_l}(\tau_l) c^{\dagger}_{j_m\sigma'_m}(\tau_m)\rangle \delta_{\sigma_l\sigma'_m} \tag{2.47}$$

The delta function comes from the fact that there are no spin flipping terms in the Hamiltonian, so there is no Green's function that describes an electron arriving at a site with a different spin than when it left.

One can show that the terms in the partition function, Z_k, can be written as the determinant of a $2k$ by $2k$ matrix $N^{(2k)}$ [32, 23, 109].

$$Z_k(\{s_l,\tau_l,i_l,j_l,\sigma_l,\sigma'_l\}) = \det[(N^{(2k)})^{-1}] \tag{2.48}$$

$$(N^{(2k)})^{-1}_{ij\sigma\sigma'} = e^{\Gamma_{ij}^{\sigma\sigma'}} - G^{ij}_{0\sigma\sigma'}\left(e^{\Gamma_{ij}^{\sigma\sigma'}} - I\right) \tag{2.49}$$

$$e^{\Gamma_{ij}^{\sigma\sigma'}} = \begin{pmatrix} \begin{pmatrix} e^{\gamma_{i_1 j_1}^{\sigma_1\sigma_1'} s_1} & 0 \\ 0 & e^{-\gamma_{i_1 j_1}^{\sigma_1\sigma_1'} s_1} \end{pmatrix} & & 0 \\ & \ddots & \\ 0 & & \begin{pmatrix} e^{\gamma_{i_k j_k}^{\sigma_k\sigma_k'} s_k} & 0 \\ 0 & e^{-\gamma_{i_k j_k}^{\sigma_k\sigma_k'} s_k} \end{pmatrix} \end{pmatrix} \tag{2.50}$$

$$G_{0\sigma\sigma'}^{ij} = \begin{pmatrix} \begin{pmatrix} g_{i_1 i_1}^{\sigma_1\sigma_1}(\tau_1-\tau_1) & g_{i_1 j_1}^{\sigma_1\sigma_1'}(\tau_1-\tau_1) \\ g_{j_1 i_1}^{\sigma_1'\sigma_1}(\tau_1-\tau_1) & g_{j_1 j_1}^{\sigma_1'\sigma_1'}(\tau_1-\tau_1) \end{pmatrix} & & \begin{pmatrix} g_{i_1 i_n}^{\sigma_1\sigma_n}(\tau_1-\tau_n) & g_{i_1 j_n}^{\sigma_1\sigma_n'}(\tau_1-\tau_n) \\ g_{j_1 i_n}^{\sigma_1'\sigma_n}(\tau_1-\tau_n) & g_{j_1 j_n}^{\sigma_1'\sigma_n'}(\tau_1-\tau_n) \end{pmatrix} \\ \vdots & \ddots & \vdots \\ \begin{pmatrix} g_{i_n i_1}^{\sigma_n\sigma_1}(\tau_n-\tau_1) & g_{i_n j_1}^{\sigma_n\sigma_1'}(\tau_n-\tau_1) \\ g_{j_n i_1}^{\sigma_n'\sigma_1}(\tau_n-\tau_1) & g_{j_n j_1}^{\sigma_n'\sigma_1'}(\tau_n-\tau_1) \end{pmatrix} & & \begin{pmatrix} g_{i_n i_n}^{\sigma_n\sigma_n}(\tau_n-\tau_n) & g_{i_n j_n}^{\sigma_n\sigma_n'}(\tau_n-\tau_n) \\ g_{j_n i_n}^{\sigma_n'\sigma_n}(\tau_n-\tau_n) & g_{j_n j_n}^{\sigma_n'\sigma_n'}(\tau_n-\tau_n) \end{pmatrix} \end{pmatrix} \tag{2.51}$$

Since the Green's functions are zero whenever the spin arguments are unequal, the $(N^{(2k)})^{-1}$ matrix can be block diagonalized into spin up, $(N_\uparrow^{(n)})^{-1}$, and spin down, $(N_\downarrow^{(m)})^{-1}$, parts. This means that the determinant can be written as

$$\det[(N^{(2k)})^{-1}] = \det[(N_\uparrow^{(n)})^{-1}]\,\det[(N_\downarrow^{(m)})^{-1}]. \tag{2.52}$$

Note that $2k = n + m$, and that in cases where there is no interaction between electrons on different sites, $V = 0$, the two spin blocks are the same size, $n = m = k$. This is easiest to see from the definitions of $(N^{(2k)})^{-1}$ and $\gamma_{ij}^{\sigma\sigma'}$. Whenever $U_{ij}^{\sigma\sigma'} = 0$, then $\gamma_{ij}^{\sigma\sigma'} = 0$. When $V = 0$, all γ elements with $\sigma = \sigma'$ will be zero, and so for all vertices we will have $\sigma = -\sigma'$, and thus all off two by two Green's function blocks will only have two non-zero elements.

Our final expression for the partition function expansion is thus

$$\begin{aligned} Z &= \sum_{k=0}^{\infty} \sum_{\substack{s_l=\pm 1 \\ l=1,\dots,k}} \sum_{\substack{i_l,j_l,\sigma_l,\sigma_l' \\ l=1,\dots,k}} \int_0^\beta d\tau_1 \dots \int_{\tau_{k-1}}^\beta \left(\frac{K}{8\beta N_c^2}\right)^k Z_k(\{s_l,\tau_l,i_l,j_l,\sigma_l,\sigma_l'\}) \\ &= \sum_{k=0}^{\infty} \sum_{\substack{s_l=\pm 1 \\ l=1,\dots,k}} \sum_{\substack{i_l,j_l,\sigma_l,\sigma_l' \\ l=1,\dots,k}} \int_0^\beta d\tau_1 \dots \int_{\tau_{k-1}}^\beta \left(\frac{K}{8\beta N_c^2}\right)^k \det[(N_\uparrow^{(n)})^{-1}]\,\det[(N_\downarrow^{(m)})^{-1}] \end{aligned} \tag{2.53}$$

It is now possible to compute the partition function by sampling this series with Quantum Monte Carlo methods [105]. We sample from all possible configurations, where each configuration is a set of k vertices, $v = \{v_l\}$. Each vertex is defined by the spin, sites, auxiliary spin, and imaginary time indices, $v_l = [i_l.j_l, \sigma_l, \sigma'_l, s_l, \tau_l]$. From a given set of vertices we can construct the $(N_\uparrow^{(n)})^{-1}$ and $(N_\downarrow^{(m)})^{-1}$ vertices. In the next section we will look at how to implement the Quantum Monte Carlo procedure for sampling this partition function and performing measurements of quantities such as the interacting Green's function, $G_\sigma(x_1, \tau_1; x_2, \tau_2)$.

2.4 Quantum Monte Carlo

Monte Carlo is a technique used for computing integrals and sums over large dimensional state spaces [105, 38]. Although deterministic techniques such as Runge-Kutta can compute such quantities efficiently in low dimensions, the computational expense of achieving a result with a given accuracy becomes intractable as the number of dimensions increases. On the other hand, the error of a Monte Carlo calculation goes like $N^{-1/2}$ regardless of the dimension of the state space, where N is the number of Monte Carlo samples. This scaling makes Monte Carlo the tool of choice for many computations involving a large dimensional state space, such as are found when simulating quantum mechanical systems.

2.4.1 Monte Carlo Introduction

As an introduction to how Monte Carlo techniques work, consider the integral of some function $f(x)$ over some volume Ω. This integral can be written as a sum over a large number of random samples of the variables, x_i.

$$\frac{1}{\Omega} \int f(x) dx = \lim_{N \to \infty} \frac{1}{N} \sum_{i=1}^{N} f(x_i) \tag{2.54}$$

Note that although this is written as an integral over some volume of space, this statement holds more abstractly with x representing various configurations of all the variables that $f(x)$ depends on, and Ω is some measure of the volume of that configuration space. Furthermore, the integral should be interpreted as an integration over all continuous variables and sums over all discrete variables that influence the value of f.

If the samples x_i are generated in a uniform and independent manner, then the error in a Monte Carlo estimation of the integral as a function of the number of samples is

$$\Delta_N = \sqrt{\frac{var(f)}{N}} = \sqrt{\frac{\langle f^2\rangle - \langle f\rangle^2}{N-1}}. \tag{2.55}$$

When the variance of the function is large, i.e. it is a strongly peaked function, then we would have to perform many samples in order to achieve some accuracy. We can address this issue via importance sampling, where instead of sampling the state space uniformly we sample according to a probability distribution, $\rho(x)$.

$$\frac{1}{\Omega}\int f(x)dx = \frac{1}{\Omega}\int \frac{f(x)}{\rho(x)}\rho(x)dx = \lim_{N\to\infty}\frac{1}{N}\sum_{i=1}^{N}\frac{f(x_i)}{\rho(x_i)} \tag{2.56}$$

$$\Delta_N^{\rho} = \sqrt{\frac{var(f/\rho)}{N}} = \sqrt{\langle\frac{(f/p)^2\rangle - \langle f/p\rangle^2}{N-1}} \tag{2.57}$$

Thus, if we generate Monte Carlo samples according to a probability distribution that matches the peaks and valleys of $f(x)$, we can achieve a specified accuracy with fewer samples, N.

2.4.2 Markov Chains and the Metropolis Algorithm

In order to implement an efficient Monte Carlo algorithm with importance sampling, we need to generate Monte Carlo samples x_i according to some probability distribution $\rho(x)$. Let's suppose that we generate these samples via a Markov Chain, where the next sampled configuration x_{i+1} depends on only the current configuration x_i [110].

$$x_0 \to x_1 \to x_2 \to \ldots x_k \to x_{k+1} \ldots \tag{2.58}$$

Such a Markov chain is fully described by a transition matrix W_{xy}, which tells us the probability of moving to state y from state x. We would like to assign transition probabilities to W_{xy} such that if we keep generating new sample points x_i, the asymptotic distribution of these samples will approach $p_x \to \rho(x)$, where p_x is the probability of being in state x. It is well known that this occurs is W satisfies two conditions:

1. W is ergodic: any state y can be reached from any state x via the Markov chain. Technically this means that there exists some finite m for which W^m_{xy} is non-zero.
2. W satisfies detailed balance: this is basically a restatement of Bayes theorem, stating that the rate of moving to state y from state x is balanced by the rate of moving to state x from state y.

   $$\frac{W_{xy}}{W_{yx}} = \frac{p_y}{p_x} \tag{2.59}$$

   Strictly speaking, this condition is actually stronger than than the minimal equilibrium requirement that $\sum_x W_{xy} = p_y$, but in practice most algorithms make use of the detailed balance condition due to the popularity of the Metropolis algorithm.

The first condition, ergodicity, is typically easy to fulfill and verify via the types of updates proposed during the Markov chain. The second condition, detailed balance, can be fulfilled via the Metropolis algorithm [111].

The Metropolis algorithm splits the transition probability into two pieces, a probability to propose a given move $x \to y$ and a probability to accept this move.

$$W_{xy} = W_{proposal}(x \to y) W_{acceptance}(x \to y) \tag{2.60}$$

The proposal probability, $W_{proposal}$, is problem dependent and is chosen to ensure ergodicity. The Metropolis algorithm defines the acceptance probability as

$$W_{acceptance}(x \to y) = \min\left(1, \frac{p_y W_{proposal}(y \to x)}{p_x W_{proposal}(x \to y)}\right). \tag{2.61}$$

One can show that these definitions of the transition matrix fulfill detailed balance by substituting them into Eq. 2.59.

2.4.3 Quantum Monte Carlo for Partition Functions

We would like to use Monte Carlo methods to sample and compute the partition function. The basic idea is to sample terms in the expansion of the partition function according to their weight. In other words, we treat the terms of the partition function as a probability distribution.

$$Z = \sum_{k=0}^{\infty} \sum_{\substack{s_l=\pm 1 \\ l=1,\ldots,k}} \sum_{\substack{i_l,j_l,\sigma_l,\sigma_l' \\ l=1,\ldots,k}} \int_0^{\beta} d\tau_1 \ldots \int_{\tau_{k-1}}^{\beta} d\tau_k Z p_k(\{s_l, \tau_l, i_l, j_l, \sigma_l, \sigma_l'\}) \tag{2.62}$$

$$p_k(\{s_l, \tau_l, i_l, j_l, \sigma_l, \sigma_l'\}) = \left(\frac{K}{8\beta N_c^2}\right)^k Z_k(\{s_l, \tau_l, i_l, j_l, \sigma_l, \sigma_l'\}) \left(\prod_{i=1}^{k} d\tau_i\right) /Z \tag{2.63}$$

Note that in order to normalize the probability distribution, we need to divide by the total partition function, Z. Because of the way in which updates will be computed, this will not pose an obstacle.

However, a critical difficulty is that because of the fermionic nature of the partition function, the terms p_k (which are ultimately expressed as determinants) can take on negative values. This prevents us from treating the terms as a probability distribution, and is the source of the well known ”fermion sign problem” that ultimately imposes limits on the applicability of Monte Carlo methods [101]. We proceed by sampling not according to the weights of the partition function terms, but rather by their absolute value.

$$\rho_k(\{s_l, \tau_l, i_l, j_l, \sigma_l, \sigma_l'\}) = \|p_k(\{s_l, \tau_l, i_l, j_l, \sigma_l, \sigma_l'\})\| \tag{2.64}$$

We can now define a Markov Chain that will sample terms in the partition function according to the probability distribution, $\rho(x) = \rho_k(\{s_l, \tau_l, i_l, j_l, \sigma_l, \sigma_l'\})$, where x now stands in for the total configuration of vertex parameters and there number, k.

According to the Markov Chain methodology, we must construct updates that move between configurations that are both ergodic and satisfy detailed balance. In our case the configurations are sets of vertices defined by auxiliary spins, imaginary times, cluster sites, and spins. For this thesis we use three different types of updates to fulfill the Markov conditions: vertex insertions, vertex removals, and vertex auxiliary spin flips.

2.4.4 Vertex Auxiliary Spin Flips

For this update we pick one vertex, v_i, from the current configuration and attempt to flip its auxiliary spin, s_i. According to the Metropolis algorithm, we first need to define a probability for proposing such a move, $W_{proposal}(s_i \to -s_i)$. If we pick the spin to flip randomly and there are k vertices, then this proposal probability is simply $W_{proposal}(s_i \to -s_i) = W_{proposal}(-s_i \to s_i) = \frac{1}{k}$. The acceptance probability is then given by

$$W_{acceptance}(s_i \to -s_i) = \min\left(1, \frac{\rho(-s_i)}{\rho(s_i)}\right) = \min\left(1, \left\| \frac{\det[(N^{(2k)})^{-1}(-s_i)]}{\det[(N^{(2k)})^{-1}(s_i)]} \right\|\right). \tag{2.65}$$

In practice we do not store the full N matrix, but rather its block diagonalized spin components, $\det[(N^{(2k)})^{-1}] = \det[(N_\uparrow^{(n)})^{-1}] \det[(N_\downarrow^{(m)})^{-1}]$. The acceptance probability in terms of these matrices depends on the spins, σ_i and σ_i', of the vertex v_i associated with s_i.

When $\sigma = \sigma_i = \sigma_i'$, the acceptance formula is

$$W_{acceptance}^{\sigma=\sigma_i=\sigma_i'}(s_i \to -s_i) = \min\left(1, \left\| \frac{\det[(N_\sigma^{(k)})^{-1}(-s_i)]}{\det[(N_\sigma^{(k)})^{-1}(s_i)]} \right\|\right), \tag{2.66}$$

whereas when $\sigma = \sigma_i = -\sigma_i'$, the acceptance probability is

$$W_{acceptance}^{\sigma=\sigma_i=-\sigma_i'}(s_i \to -s_i) = \min\left(1, \left\| \frac{\det[(N_\sigma^{(n)})^{-1}(-s_i)] \det[(N_{-\sigma}^{(m)})^{-1}(-s_i)]}{\det[(N_\sigma^{(n)})^{-1}(s_i)] \det[(N_{-\sigma}^{(m)})^{-1}(s_i)]} \right\|\right), \tag{2.67}$$

2.4.5 Vertex Insertion and Removal

We need to be careful when computing the proposal probabilities for adding or removing a vertex. If configuration x has k vertices and $x = \{v_l\} = \{s_l, \tau_l, i_l, j_l, \sigma_l, \sigma_l'\}$ and $y = \{v_l\} + v = \{s_l, \tau_l, i_l, j_l, \sigma_l, \sigma_l'\} + (s, \tau, i, j, \sigma, \sigma')$, then we need to compute $W_{proposal}(x \to y)$ for insertion and $W_{proposal}(y \to x)$ for removal.

When we choose a new vertex to add to the configuration $v = (s, \tau, i, j, \sigma, \sigma')$, there is a 1/2 probability of choosing one of the two values of s, σ, and σ'. There is also a $1/N_c$ probability of choosing each of the values of i and j. Finally, there is a

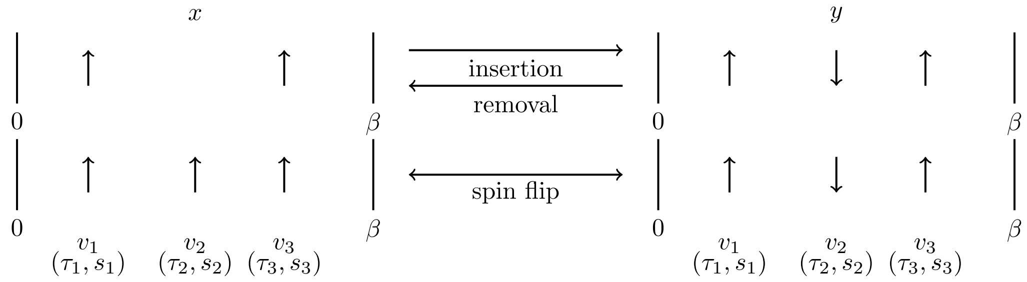

Figure 2.4: Example of how spin flip and removal/insertion updates change the vertex configuration during the CT-AUX Monte Carlo simulation. Each vertex has parameters $v = (s, \tau, i, j, \sigma, \sigma')$, but the site indices and electron spins have been suppressed in this figure for clarity.

probability of $d\tau/\beta$ of choosing τ. Thus, the proposal probability for insertion is

$$W_{proposal}(x \to y) = \frac{1}{8N_c^2}\frac{d\tau}{\beta}. \tag{2.68}$$

The proposal probability for removal, $W_{proposal}(y \to x)$, is much simpler. Since we choose one vertex from $k+1$ vertices to remove, it is just

$$W_{proposal}(y \to x) = \frac{1}{k+1} \tag{2.69}$$

Using the Metropolis algorithm again, we obtain an expression for the acceptance probability

$$\begin{aligned} W_{acceptance}(x \to y) &= \min\left(1, \frac{p_y W_{proposal}(y \to x)}{p_x W_{proposal}(x \to y)}\right) \\ &= \min\left(1, \frac{8N_c^2 \beta \rho(y)}{d\tau(k+1)\rho(x)}\right) \\ &= \min\left(1, \frac{8N_c^2\beta}{d\tau(k+1)} \frac{\left(\frac{K}{8\beta N_c^2}\right)^{k+1} Z_{k+1}(y)\left(\prod_{i=1}^{k+1} d\tau_i\right)}{\left(\frac{K}{8\beta N_c^2}\right)^{k} Z_k(x)\left(\prod_{i=1}^{k} d\tau_i\right)}\right) \\ &= \min\left(1, \frac{K}{k+1}\left\|\frac{\det[(N_\uparrow)^{-1}(y)]\det[(N_\downarrow)^{-1}(y)]}{\det[(N_\uparrow)^{-1}(x)]\det[(N_\downarrow)^{-1}(x)]}\right\|\right) \end{aligned} \tag{2.70}$$

The acceptance probability for removal involves the inverse of the expression on the right side of min, with $k \to k-1$.

2.4.6 Measurement and the Sign Problem

During the Monte Carlo simulation of a system we perform measurements of physical quantities such as the density, the magnetization, or the single particle Green's function. Most observables, $\hat{\mathcal{O}}$, can be expressed as statistical expectation values weighted by the partition function, and thus can be expressing in similar expansions.

$$\langle\hat{\mathcal{O}}\rangle = \frac{1}{Z}\sum_{k=0}^{\infty}\sum_{\substack{s_l=\pm1\\ l=1,\dots,k}}\sum_{\substack{i_l,j_l,\sigma_l,\sigma_l'\\ l=1,\dots,k}}\int_0^{\beta}d\tau_1\dots\int_{\tau_{k-1}}^{\beta}d\tau_k\hat{\mathcal{O}}Zp_k(\{s_l,\tau_l,i_l,j_l,\sigma_l,\sigma_l'\}) \tag{2.71}$$

Let us write this more simply and recognize that we actually sample the distribution according to $\rho(x) = \|p(x)\|$, so that $p(x) = \rho(x)\mathrm{sign}(p(x))$.

$$\begin{aligned}\langle\hat{\mathcal{O}}\rangle &= \frac{\int\mathcal{O}(x)p(x)dx}{\int p(x)dx}\\ &= \frac{\int\mathcal{O}(x)\rho(x)\mathrm{sign}(p(x))dx}{\int\rho(x)\mathrm{sign}(p(x))dx}\\ &= \frac{\int\mathcal{O}(x)\rho(x)\mathrm{sign}(p(x))dx}{\int\rho(x)dx}/\frac{\int\rho(x)\mathrm{sign}(p(x))dx}{\int\rho(x)dx}\\ &= \langle\mathcal{O}(x)\mathrm{sign}(p(x))\rangle|_{\rho(x)}/\langle\mathrm{sign}(p(x))\rangle|_{\rho(x)}\end{aligned} \tag{2.72}$$

Thus, in order to compute the Monte Carlo estimate of observables, through out the simulation we must accumulate the values of $\mathcal{O}(x)\mathrm{sign}(p(x))$ and $\mathrm{sign}(p(x))$, and divide them at the end. The fermion sign problem occurs whenever the average sign, $\mathrm{sign}(p(x))$, becomes small. In this case we need to divide all of our results by a small number, which exponentially increases the number of measurements we need to make in order to achieve a specified level of accuracy.

The sign problem does not occur at half filling when $V = 0$, nor in single site DMFT [81]. However, the average sign often decreases dramatically when the cluster size, N_c, is increased, when the temperature, $\beta = 1/T$ is lowered, or when the interaction strengths increase. A general and efficient 'solution' to the sign problem is highly unlikely, since it has been shown to belong to the NP complexity class [112]. Nonetheless, the sign problem creates the major limitation in QMC simulations, and many techniques and special cases have been explored to try to suppress it [101].

The single particle Green's function can be measured with the following formula, which follows from expanding the statistical expression for the Green's function, $G = \langle cc^\dagger \rangle = \frac{\mathrm{Tr}\left[cc^\dagger e^{-\beta H}\right]}{Z}$ and then Fourier transforming [109, 25].

$$G(i\omega_n) = \mathcal{G}^0(i\omega_n) - \frac{\mathcal{G}^0(i\omega_n)^2}{\beta} \sum_{pq} e^{i\omega_n \tau_p} M_{pq} e^{-i\omega_n \tau_q} \tag{2.73}$$

$$M_{pq} = \left[\left(e^{\Gamma_{ij}^{\sigma\sigma'}} - 1 \right) N^{(2k)} \right]_{pq} \tag{2.74}$$

2.5 Maximum Entropy

A significant challenge in extracting physical results from Quantum Monte Carlo calculations performed with the CT-AUX method is that the algorithm works in imaginary time, τ, and imaginary (Matsubara) frequency, $i\omega_n = i\frac{(2n+1)\pi}{\beta}$, space. This presents an issue because experiments obviously obtain real time and real frequency data, and physical interpretation and intuition can be difficult with imaginary axis data. This section describes the Maximum Entropy Method (MEM) for numerical analytic continuation used throughout this thesis to obtain real frequency data, following references [100, 99]. All such results were obtained with the 'MaxEnt' code [100].

Specifically, one of the outputs from a DMFT calculation is the Matsubara frequency Green's function, $G(i\omega_n)$, or its transform into imaginary time, $G(\tau)$. These are related through a Fourier transform [91].

$$G(i\omega_n) = \int_0^\beta e^{i\omega_n \tau} G(\tau) \tag{2.75}$$

These Green's function will typically have other indices as well, such as lattice site, spin, or momentum, but for now we simply focus on the time-like index. Most numerical analytic continuation methods treat these different components independently, i.e. $G(\tau, k_1)$ is continued independently of $G(\tau, k_2)$.

While there are some physical quantities that can be directly extracted from imaginary axis data, such at the density $n = \langle c^\dagger c \rangle = G(\tau = 0^-)$, many quantities require access to real frequency data. Via complex analysis one can show that the imaginary time and imaginary frequency data can be related to the real frequency Green's functions as follows [3].

$$G(i\omega_n) = -\frac{1}{\pi}\int_{-\infty}^{\infty} \frac{Im[G(\omega)]}{i\omega_n - \omega} \tag{2.76}$$

$$G(\tau) = \frac{1}{\pi}\int_{-\infty}^{\infty} \frac{Im[G(\omega)]e^{\tau\omega}}{1 + e^{-\beta\omega}} \tag{2.77}$$

In the above, $Im[G(\omega)]$ is the imaginary part of the the real frequency Green's function. It is related to the spectral function, $A(\omega)$, which describes how many states are available at different energies in a system, via

$$A(\omega) = -\frac{1}{\pi}Im[G(\omega)]. \tag{2.78}$$

We can write these equation in a more general form as

$$G_n = \int_{-\infty}^{\infty} d\omega K_n(\omega)A(\omega) \tag{2.79}$$

where G_n is for example $G(i\omega_n)$ or $G(\tau_n)$, and $K_n(\omega)$ is called the kernel.

The spectral function, and real frequency Green's functions generally, are key quantities to obtain in order to analyze the physics of simulations and compare them to real world experiments. This would not be very difficult if we had analytic expressions for the imaginary axis Green's functions, since analytic continuation is typically a straightforward and well-defined procedure when given specific functions.

Unfortunately, since the imaginary axis Green's function data we obtain from Quantum Monte Carlo codes are obtained from averages of M samples, the data is only known to a certain precision and contains statistical noise [100]. If $G_n^{(i)}$ is the i-th sample of G_n then the Monte Carlo estimate of this quantity is

$$\bar{G}_n = \frac{1}{M}\sum_{i=1}^{M} G_n^{(i)}, \tag{2.80}$$

with correlations between data points characterized by a covariance matrix, C_{nm}.

$$C_{nm} = \frac{1}{M(M-1)}\sum_{i=1}^{M}(G_n - G_n^{(i)})(G_m - G_m^{(i)}) \tag{2.81}$$

In practice the real space frequencies are discretized, so we are trying to solve for $A_m = A(\omega_m)$ from the following matrix equation obtained by discretizing 2.79.

$$\bar{G}_n = K_{nm} A_m \tag{2.82}$$

Where $K_{nm} = K_n(\omega_m)\Delta\omega$. The most obvious way to solve this equation is to compute $A = K^{-1}\bar{G}$, but this problem turns out to be very ill-conditioned because the elements of the matrix K become very small for large values of τ or ω. This means that the determinant of K will be very small, which in turns means that K^{-1} will be ill-defined. (Since matrix inverses are proportional to $\det(A)^{-1}$.) Another way of expressing this problem is that given some error range for $\bar{G}$, described by C_{nm}, many different A could yield $\bar{G}$ to within this error range because the high frequency components are minimized by the small values contained in K. Thus, the small statistical uncertainty in $\bar{G}_n$ leads to a very large uncertainty in A_m under straightforward inversion [100].

The Maximum Entropy Method uses Bayesian statistics to define a process for obtaining a spectral function A that maximizes the conditional probability of A given the imaginary axis data $\bar{G}$, $P(A|\bar{G})$ [99]. According to Bayes theorem, this conditional probability is given by

$$P(A|\bar{G}) = P(\bar{G}|A)P(A)/P(\bar{G}). \tag{2.83}$$

Since we are typically continuing a single set of data $\bar{G}$, the prior probability $P(\bar{G})$ is constant throughout the calculation and can be ignored.

When A is positive definite and $\int d\omega A(\omega) < \infty$, as is the case for fermionic spectral functions, it can be interpreted at an unnormalized probability distribution. One can then argue that the prior probability for such a distribution, $P(A)$, can be expressed as a function of the entropy relative to a default model, $d(\omega)$ [113]. The prior probability is then conditional on the unknown model, $d(\omega)$, and the parameter α as follows.

$$P(A|d,\alpha) = e^{\alpha S} \tag{2.84}$$

$$S = \int d\omega \left(A(\omega) - d(\omega) - A(\omega)\ln\left[A(\omega)/d(\omega)\right]\right) \tag{2.85}$$

Although we have introduced two unknowns into our probability, the default model and α, this form has three benefits [99]. One is that it enforces the positivity of $A(\omega)$, as is physically required. The second is that by maximizing this entropy term, spurious correlations in the data will be minimized. This encapsulates the assumption that in the absence of more data about A beyond that given by $\bar{G}$, it is most reasonable to assume that its various components are uncorrelated. The third benefit is that through the default model $d(\omega)$ we are able to inject physically known requirements, such as the behavior of the function at large frequencies.

The likelihood function, $P(\bar{G}|A)$, can be found via the Central Limit Theorem when the different measurements of $\bar{G}_n$ are uncorrelated. Although this assumption is not generally true, it can be achieved by carefully rebinning the data and increasing the number of Monte Carlo steps between measurements. In this case the likelihood function is

$$P(\bar{G}|A) = e^{-\chi^2/2}, \tag{2.86}$$

where

$$\chi^2 = \sum_n \left(\frac{\bar{G}_n - K_{nj} A_j}{\sigma_n}. \right)^2 \tag{2.87}$$

Maximizing this term simply corresponds to a least squares fit of the data, and so this term pushes A is more closely reproduce the data points $\bar{G}$. An important assumption in the above is that the covariance matrix is diagonal, i.e. the different components of $\bar{G}$ are uncorrelated. Although this might not be true for the original data, it is often possible to rotate into a basis where C_{nm} is diagonal in order to cleanly measure the difference between the data and the spectral function. [99]

The probability of A given the data $\bar{G}$, the default model $d(\omega)$, and the parameter α, is then given by

$$P(A|G, d, \alpha) \propto e^{\alpha S - \chi^2/2}. \tag{2.88}$$

In order to maximize this probability, we are then looking for the spectral function $\hat{A}(\alpha)$ that maximizes the cost function, Q.

$$Q = \alpha S - \chi^2/2 \tag{2.89}$$

The role of α is clearly to balance the importance of fitting the data precisely and suppressing spurious correlations through the entropy term. For each value of α we expect to get a different optimal spectral function, $\hat{A}(\alpha)$, so a method for choosing α

is required. In this work we make use of Bryan's method for constructing the optimal spectral function, $\bar{A}$, as a weighted average over the candidate spectral functions.

$$\bar{A} = \int d\alpha \hat{A}(\alpha) P(\alpha|\bar{G}, d) \tag{2.90}$$

More details on this method, including the conditional probability of α, $P(\alpha|\bar{G}, d)$, can be found in the original work [114]. In theory a comparable method for picking the default model can be used, but in practice it has been found that robust spectra only weakly depend on the default model [99]. In practice we simply run the algorithm with several different noninformative default models and check that the physical results do not change. "Noninformative" simply means that the default models do not contain strong correlations, for example a flat spectral function or a broad Gaussian.

Chapter 3

Twisted Boundary Conditions

This chapter describes work on applying the methods of twisted boundary conditions (TBC) to the DCA framework in order to control finite size effects. We present detailed derivations of how TBC can be applied and the requisite modifications to the DCA numerics. We also present some comparisons between results from exact diagonalization, second order perturbation theory, and DCA.

3.1 Introduction

There has been a lot of effort put into understanding the properties of the Hubbard model. One barrier that remains to be overcome is that methods such as Quantum Monte Carlo (QMC) are still limited to relatively small clusters, with at most 100 sites at high temperatures. In particular, DCA works by segmenting momentum space into patches and averaging quantities such as the self energy over each patch [14]. Increasing the momentum resolution of such simulations by increasing cluster size requires an exponential increase in computational time, especially when the fermion sign problem arises. This means that finite size errors are one of the dominant uncertainties in many types of many-body computations [32, 115]. One idea to bypass this challenge is to utilize twisted boundary conditions (TBC) to shift the characteristic momentum of cluster states by an arbitrary amount, allowing one to gain information about other momentum points without increasing the cluster size [15].

The use of twisted boundary conditions is pervasive in computational physics, including exact diagonalization [18], diffusion Monte Carlo [116], density function theory [38], and lattice gauge theory [117]. If we simulate a finite system (a supercell) that is understood to be a subsystem of a larger lattice, then we can look for solutions to the electron density that are periodic in the supercell vectors, $\vec{L}_m$. Bloch's theorem then tells us that the solution wavefunctions are characterized by a supercell momentum, $\vec{K}$.

$$\Psi_{\vec{K}}(\vec{r}_1 + \vec{L}_m, \vec{r}_2, \ldots, \vec{r}_N) = e^{i\vec{K}\cdot\vec{L}_m}\Psi_{\vec{K}}(\vec{r}_1, \vec{r}_2, \ldots, \vec{r}_N) \tag{3.1}$$

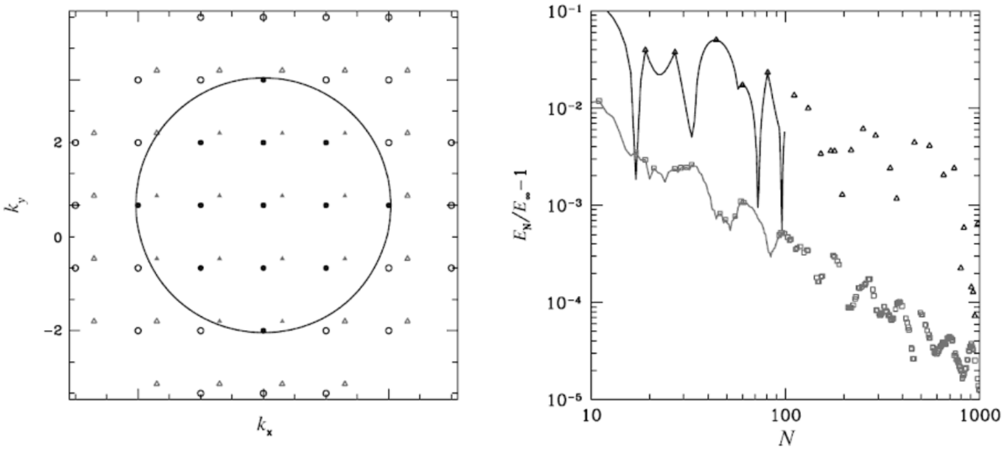

Figure 3.1: Example of how averaging over twisted boundary conditions can help reduce finite size errors. Left: The occupied states (filled symbols) in a system of 13 non-interacting fermions, compared to the infinite system Fermi surface (solid line). Circles correspond to periodic boundary conditions (PBC), triangles to TBC with $\phi = 2\pi(0.3, 0.15)$. Right: The error in the energy comparing PBC (upper symbols) and averaging over TBC (lower symbols) in 3D. The TBC curve fluctuates much less with the number of electrons, making a thermodynamic extrapolation easier [15].

The phase $\theta_m = \vec{K}\cdot\vec{L}_m$ then tells us the phase an electron picks up when it loops around the supercell in the finite simulation. Periodic boundary conditions (PBC) correspond to $\vec{\theta} = 0$, and nonzero $\vec{\theta}$ are twisted boundary conditions.

One can show that the single particle states are shifted in momentum by the TBC used [32]. This implies that be averaging over these boundary conditions one can sample the Brillouin zone more evenly, approximating the momentum space integrals of the infinite system. Fig. 3.1 demonstrates this idea for a system of non-interacting electrons.

In this chapter we will describe efforts to apply twisted boundary conditions to the Hubbard model in the Dynamical Cluster Approximation (DCA) framework. Some examples of the finite size errors that occur in DCA are shown in Fig. 3.2. Along the way we will show that solving the Hubbard model with TBC is equivalent to solving the Hubbard model with periodic boundary conditions and a multiplicative phase factor on the hopping parameter t. The later model is shown to be equivalent (in a particular gauge) to adding a vector potential to the Hubbard model, which allows us to use gauge invariance to show how to change between boundary conditions.

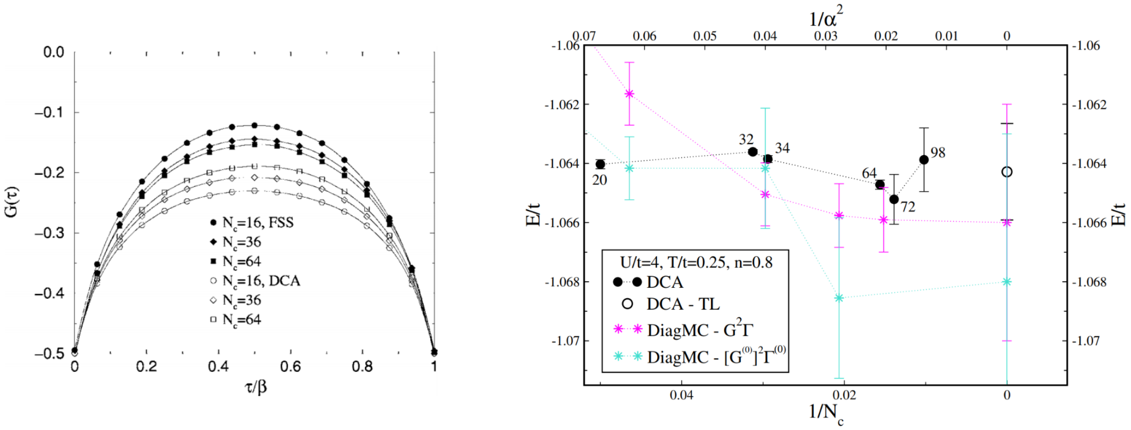

Figure 3.2: Two examples of the finite size error in DCA. Left: Change in the imaginary time Green's, $G(k, \tau)$, function at $k = (0, \pi)$ versus cluster size for a half-filled 2D Hubbard model with $U = 4.4t$ and $\beta = 4/t$. DCA (open symbols) is compared with finite-size quantum Monte Carlo (filled symbols). These two methods have the opposite convergence behavior - DCA underestimates and FSS overestimates gaps at small cluster sizes. [14] Right: Change in the energy computed by DCA versus the cluster size for a 2D Hubbard model with $U/t = 4$, $T/t = 0.25$ and $n = 0.8$. Also included are results from different forms of diagrammatic Monte Carlo [16].

3.2 Hubbard Model

The Hubbard model consists of a lattice of discrete sites that electrons can exist on and move between [90]. Up to two electrons (spin up and down) can exist on each site. Electrons that occupy the same site interact via a repulsive energy U. The ability for electrons to move between two adjacent sites (nearest neighbor hopping) is modeled by a hopping energy t. There is also a chemical potential μ that controls how many electrons are in the system (the density). The Hubbard Hamiltonian is given by

$$H = -\sum_{<ij>\sigma}(t_{ij}c^\dagger_{i\sigma}c_{j\sigma} + t_{ji}c^\dagger_{j\sigma}c_{i\sigma}) - \mu\sum_{i\sigma} n_{i\sigma} + U\sum_i n_{i\uparrow}n_{i\downarrow} \tag{3.2}$$

The sums run over all the lattice indices, i, and spins, $\sigma = \uparrow, \downarrow$. The symbol $< ij >$ means that only terms with sites i and j adjacent to each other are included. The number operator $n_{i\sigma} = c^\dagger_{i\sigma}c_{i\sigma}$ gives 1 when there is an electrons with spin σ on site i and 0 otherwise. Note that in order for the Hamiltonian to be Hermitian ($H = H^\dagger$), we need $t_{ji} = t^*_{ij}$. As it stands, half-filling occurs when $\mu = U/2$. It is convenient to fix the occurrence of half-filling at $\mu = 0$ by writing the Hamiltonian as

$$H = -\sum_{<ij>\sigma}(t_{ij}c^\dagger_{i\sigma}c_{j\sigma} + t^*_{ij}c^\dagger_{j\sigma}c_{i\sigma}) - \mu\sum_{i\sigma} n_{i\sigma} + U\sum_i(n_{i\uparrow} - \frac{1}{2})(n_{i\downarrow} - \frac{1}{2}) \tag{3.3}$$

The non-interacting Hubbard model occurs when $U = 0$, and half-filling is $\mu = 0$.

$$H = -\sum_{<ij>\sigma}(t_{ij}c^\dagger_{i\sigma}c_{j\sigma} + t^*_{ij}c^\dagger_{j\sigma}c_{i\sigma}) \tag{3.4}$$

In this work we have in mind a 2D square lattice that has $N = LxL$ sites with the topology of a torus.

3.3 Adding a Vector Potential

It is typically the case that the hopping parameter is real, $t = t_{ij} = t^*_{ij}$, in which case t is just some amplitude for an electron to hop between lattice sites and would be calculated from a tight-binding calculation [91]. However, in the presence of a magnetic field, $\vec{B} = \vec{\nabla} \times \vec{A}$, such amplitudes are multiplied by the exponential of the line integral of the vector potential along the hopping path. This so-called Peierls substitution [118, 119, 120] is given by,

$$t_{ij} \to |t_{ij}|e^{-i\frac{e}{\hbar}\int_i^j \vec{A}\cdot\vec{dl}}. \tag{3.5}$$

It remains true that $t_{ij} = t^*_{ji}$, but the hopping parameter is now generally complex.

If there is no magnetic field then $\vec{B} = \vec{\nabla} \times \vec{A} = 0$, which means that we can write,

$$\vec{A} = \vec{\nabla}\chi. \tag{3.6}$$

where χ is any scalar function. Then we have,

$$t_{ij} \rightarrow |t_{ij}| e^{-i\frac{e}{\hbar}(\chi_j - \chi_i)}, \tag{3.7}$$

Now let's suppose that χ is not single valued, but instead increases by,

$$\Delta_x \chi = \chi_{i+L\vec{x}} - \chi_i = \int_i^{i+L\vec{x}} \vec{A} \cdot \vec{dx} = \Phi_x \tag{3.8}$$

and

$$\Delta_y \chi = \Phi_y \tag{3.9}$$

whenever you loop around the lattice in the x or y direction. For linear χ we then have

$$\chi_j - \chi_i = \chi_{x_j y_j} - \chi_{x_i y_i} = (x_j - x_i)\frac{\Phi_x}{L} + (y_j - y_i)\frac{\Phi_y}{L} \tag{3.10}$$

Let's assume that $|t_{ij}| = t$ for all bonds. Since we only have nearest neighbor hopping, we find that there are now two different hopping parameters for vertical and horizontal bonds.

$$t_x = te^{-i\frac{e}{\hbar}\frac{\Phi_x}{L}} = te^{-i\theta_x} \tag{3.11}$$

$$t_y = te^{-i\frac{e}{\hbar}\frac{\Phi_y}{L}} = te^{-i\theta_y} \tag{3.12}$$

Plugging this into our Hamiltonian and labeling lattice sites as $i = (n, m)$, we obtain

$$H = -t \sum_{(n,m)\sigma} (e^{-i\theta_x} c^\dagger_{(n,m)\sigma} c_{(n+1,m)\sigma} + e^{i\theta_x} c^\dagger_{(n+1,m)\sigma} c_{(n,m)\sigma} + e^{-i\theta_y} c^\dagger_{(n,m)\sigma} c_{(n,m+1)\sigma} + e^{i\theta_y} c^\dagger_{(n,m+1)\sigma} c_{(n,m)\sigma}) \tag{3.13}$$

Now we transform the Hamiltonian into momentum space via a Fourier transform.

$$c^{\dagger}_{(n,m)} = \sum_{(k_x,k_y)} e^{i(k_x n + k_y m)} c^{\dagger}_{(k_x,k_y)} \tag{3.14}$$

with $k_x, k_y = k\frac{2\pi}{L}$, where k is an integer. Making the transformation, the Hamiltonian becomes

$$\begin{aligned} H = -t \sum_{(k_x,k_y)} & e^{-i(k_x+\theta_x)} c^{\dagger}_{(k_x,k_y)} c_{(k_x,k_y)} + e^{i(k_x+\theta_x)} c^{\dagger}_{(k_x,k_y)} c_{(k_x,k_y)} \\ & + e^{-i(k_y+\theta_y)} c^{\dagger}_{(k_x,k_y)} c_{(k_x,k_y)} + e^{i(k_y+\theta_y)} c^{\dagger}_{(k_x,k_y)} c_{(k_x,k_y)} \end{aligned} \tag{3.15}$$

Combining the phase factors via Euler's identity results in a fairly simple result for the Hamiltonian.

$$H = -2t \sum_{(k_x,k_y)} (cos(k_x + \theta_x) + cos(k_y + \theta_y)) c^{\dagger}_{(k_x,k_y)} c_{(k_x,k_y)} \tag{3.16}$$

Defining the new single particle dispersion as

$$\epsilon_{\vec{k}} = -2t(cos(k_x + \theta_x) + cos(k_y + \theta_y)). \tag{3.17}$$

Our final non-interacting Hamiltonian is given by

$$H = \sum_{(k_x,k_y)} \epsilon_{(k_x,k_y)} c^{\dagger}_{(k_x,k_y)} c_{(k_x,k_y)} = \sum_{\vec{k}} \epsilon_{\vec{k}} c^{\dagger}_{\vec{k}} c_{\vec{k}}. \tag{3.18}$$

Thus, the net effect of the twisted boundary conditions is to shift the momenta appearing in the single particle dispersion.

3.4 TBC on Betts Clusters

DCA makes use of finite size clusters of different sizes and geometries, typically referred to as Betts clusters [121]. Let's say the the lattice vectors for a cluster are $\vec{a}_1$,$\vec{a}_2$. Normal periodic boundary conditions are then defined by

$$\psi(\vec{x} + u_1\vec{a}_1 + u_2\vec{a}_2) = \psi(\vec{x}). \tag{3.19}$$

Where u_1,u_2 are integers. For arbitrary boundary conditions, we'd like the wave function to pick up a phase when an electron follows one of the lattice vectors around the lattice.

$$\psi(\vec{x} + u_1\vec{a}_1 + u_2\vec{a}_2) = e^{i(u_1\theta_1 + u_2\theta_2)}\psi(\vec{x}) \tag{3.20}$$

Or more compactly

$$\psi(\vec{x} + A\vec{u}) = e^{i\left(\vec{\theta}\cdot\vec{u}\right)}\psi(\vec{x}) \tag{3.21}$$

Where $A = [\vec{a}_1, \vec{a}_2]$ is a matrix of the lattice vectors.

The wavefunction for an arbitrary state α can be expressed as

$$\begin{aligned}
\psi(\vec{x}) &= \langle \vec{x} | \alpha \rangle \\
&= \langle 0 | c_{\vec{x}} | \alpha \rangle \\
&= \left\langle 0 | c_{\vec{x}} \sum_i a_i c^{\dagger}_{\vec{k}_i} | 0 \right\rangle \\
&= \sum_i a_i \left\langle 0 | c_{\vec{x}} c^{\dagger}_{\vec{k}_i} | 0 \right\rangle \\
&= \sum_i a_i \left\langle 0 | c_{\vec{x}} \sum_{\vec{y}} c^{\dagger}_{\vec{y}} e^{i\vec{k}_i\cdot\vec{y}} | 0 \right\rangle \\
&= \sum_i a_i \left\langle 0 | e^{i\vec{k}_i\cdot\vec{x}} | 0 \right\rangle
\end{aligned} \tag{3.22}$$

Thus

$$\begin{aligned}
\psi(\vec{x} + A\vec{u}) &= \sum_i a_i \left\langle 0 | e^{i\vec{k}_i\cdot(\vec{x}+A\vec{u})} | 0 \right\rangle \\
&= e^{i\left(\vec{\theta}\cdot\vec{u}\right)}\psi(\vec{x}) \\
&= \sum_i a_i \left\langle 0 | e^{i\vec{k}_i\cdot\vec{x}} | 0 \right\rangle e^{i\left(\vec{\theta}\cdot\vec{u}\right)}
\end{aligned} \tag{3.23}$$

Each term should match, which requires

$$e^{i\vec{k}_i\cdot A\vec{u}} = e^{i\left(\vec{\theta}\cdot\vec{u}\right)}, \tag{3.24}$$

and

$$\vec{k}_i \cdot A\vec{u}\vec{\theta} \cdot \vec{u} + 2\pi\,(n, m) \cdot \vec{u}. \tag{3.25}$$

This should hold for all $\vec{u}$, so

$$\vec{k}_i^T A = \vec{\theta}^T + 2\pi \left(n, m\right), \tag{3.26}$$

or equivalently

$$(\vec{k}_i \cdot \vec{a}_1, \vec{k}_i \cdot \vec{a}_2) = (\theta_1, \theta_2) + 2\pi(n, m). \tag{3.27}$$

This will be satisfied if we write $\vec{k}$ as

$$\vec{k} = n\vec{b}_1 + m\vec{b}_2 + \frac{\theta_1}{2\pi}\vec{b}_1 + \frac{\theta_2}{2\pi}\vec{b}_2, \tag{3.28}$$

with

$$\vec{a}_i \cdot \vec{b}_j = 2\pi\delta_{ij}, \tag{3.29}$$

or equivalently

$$B^T A = 2\pi I. \tag{3.30}$$

$$B^T = \begin{pmatrix} \vec{b}_1^T \\ \vec{b}_2^T \end{pmatrix} = 2\pi A^{-1} = 2\pi \begin{pmatrix} \vec{a}_1 & \vec{a}_2 \end{pmatrix}^{-1} \tag{3.31}$$

Which is also equivalent to

$$\vec{b}_1 = 2\pi \frac{Rot(\vec{a}_2)}{\vec{a}_1 \cdot Rot(\vec{a}_2)} \tag{3.32}$$

$$\vec{b}_2 = 2\pi \frac{Rot(\vec{a}_1)}{\vec{a}_2 \cdot Rot(\vec{a}_1)} \tag{3.33}$$

Where $Rot(\vec{a})$ rotates the vector by 90 degrees.

This gives us a system with a TBC wavefunction with the momentum shifted from their usual PBC positions. We could instead work with a periodic wavefunction at the price of complex hoppings by applying a gauge transform.

The TBC wavefunction obeys

$$\psi(\vec{x} + A\vec{u}) = e^{i\left(\vec{\theta}\cdot\vec{u}\right)}\psi(\vec{x}). \tag{3.34}$$

We can now perform a gauge transform.

$$\psi(\vec{x}) \to e^{i\vec{\theta}A^{-1}\vec{x}}\tilde{\psi}(\vec{x}) \tag{3.35}$$

$$e^{i\vec{\theta}A^{-1}(\vec{x}+A\vec{u})}\tilde{\psi}(\vec{x}+A\vec{u}) = e^{i\left(\vec{\theta}\cdot\vec{u}\right)}e^{i\vec{\theta}A^{-1}\vec{x}}\tilde{\psi}(\vec{x}) \tag{3.36}$$

$$e^{i\vec{\theta}A^{-1}\vec{x}}e^{i\vec{\theta}A^{-1}A\vec{u}}\tilde{\psi}(\vec{x}+A\vec{u}) = e^{i\left(\vec{\theta}\cdot\vec{u}\right)}e^{i\vec{\theta}A^{-1}\vec{x}}\tilde{\psi}(\vec{x}) \tag{3.37}$$

So for the gauge transformed wavefunction we restore periodic boundary conditions.

$$\tilde{\psi}(\vec{x}+A\vec{u}) = \tilde{\psi}(\vec{x}) \tag{3.38}$$

The transform for the creation and annihilation operators is given by considering the following.

$$\psi(\vec{x}) = \langle 0|c_{\vec{x}}|\alpha\rangle \to e^{i\vec{\theta}A^{-1}\vec{x}}\tilde{\psi}(\vec{x}) = e^{i\vec{\theta}A^{-1}\vec{x}}\,\langle 0|\tilde{c}_{\vec{x}}|\alpha\rangle \tag{3.39}$$

This implies that the operators transform as follows.

$$c_{\vec{x}} \to e^{i\vec{\theta}A^{-1}\vec{x}}\tilde{c}_{\vec{x}} \tag{3.40}$$

$$c^{\dagger}_{\vec{x}} \to e^{-i\vec{\theta}A^{-1}\vec{x}}\tilde{c}^{\dagger}_{\vec{x}} \tag{3.41}$$

This transform also preserves the commutation relations.

$$\begin{aligned}\left\{\tilde{c}^{\dagger}_{\vec{x}}, \tilde{c}_{\vec{y}}\right\} &= e^{-i\vec{\theta}A^{-1}\vec{x}}e^{i\vec{\theta}A^{-1}\vec{y}}\left\{c^{\dagger}_{\vec{x}}, c_{\vec{y}}\right\}\\ &= \delta_{\vec{x}\vec{y}}\end{aligned} \tag{3.42}$$

The hopping terms in the Hubbard model will become (now dropping twiddles)

$$c^{\dagger}_{\vec{x}+\hat{i}}c_{\vec{x}} \to e^{-i\vec{\theta}A^{-1}\left(\vec{x}+\hat{i}\right)}e^{i\vec{\theta}A^{-1}\vec{x}}c^{\dagger}_{\vec{x}+\hat{i}}c_{\vec{x}}. \tag{3.43}$$

So there is a hopping phase in the $\hat{i}$ direction as follows.

$$
\begin{aligned}
i\phi_{\hat{i}} &= -\vec{\theta} A^{-1} \hat{i} \\
&= -\frac{1}{2\pi} \vec{\theta} \begin{pmatrix} \vec{b}_1^T \\ \vec{b}_2^T \end{pmatrix} \hat{i} \\
&= -\frac{1}{2\pi} \left(\theta_1 b_{11} + \theta_2 b_{21} \right)
\end{aligned}
\tag{3.44}
$$

And similarly in the $\hat{j}$ direction.

$$
i\phi_{\hat{j}} = -\frac{1}{2\pi} \left(\theta_1 b_{12} + \theta_2 b_{22} \right) \tag{3.45}
$$

The hopping terms are thus

$$
H_0 = -t \sum_{\vec{x}} e^{i\phi_{\hat{i}}} c^{\dagger}_{\vec{x}+\hat{i}} c_{\vec{x}} + e^{-i\phi_{\hat{i}}} c^{\dagger}_{\vec{x}} c_{\vec{x}+\hat{i}} + e^{i\phi_{\hat{j}}} c^{\dagger}_{\vec{x}+\hat{j}} c_{\vec{x}} + e^{-i\phi_{\hat{j}}} c^{\dagger}_{\vec{x}} c_{\vec{x}+\hat{j}}. \tag{3.46}
$$

Fourier transforming these terms gives us

$$
H_0 = -t \sum_{\vec{k}} e^{i\phi_{\hat{i}}} e^{ik_{\hat{i}}} c^{\dagger}_{\vec{k}} c_{\vec{k}} + e^{-i\phi_{\hat{i}}} e^{-ik_{\hat{i}}} c^{\dagger}_{\vec{k}} c_{\vec{k}} + e^{i\phi_{\hat{j}}} e^{ik_{\hat{j}}} c^{\dagger}_{\vec{k}} c_{\vec{k}} + e^{-i\phi_{\hat{j}}} e^{-ik_{\hat{j}}} c^{\dagger}_{\vec{k}} c_{\vec{k}}. \tag{3.47}
$$

Using the identity $2cos(x) = e^{ix} + e^{-ix}$, we have

$$
H_0 = \sum_{\vec{k}} \epsilon(\vec{k}) c^{\dagger}_{\vec{k}} c_{\vec{k}} \tag{3.48}
$$

$$
\epsilon(\vec{k}) = -2t \sum_{\hat{x}} cos(k_{\hat{x}} + \phi_{\hat{x}}) \tag{3.49}
$$

$$
\phi_{\hat{x}} = \frac{1}{2\pi} \left(\vec{\theta}^T B^T \right)_{\hat{x}} = \frac{1}{2\pi} \left(B\theta \right)_{\hat{x}} \tag{3.50}
$$

Where $\hat{x}$ labels the dimension, $\hat{x} = 1, 2, 3$ for directions x,y,z. Figure 3.3 depicts both the cluster momenta, $\vec{k}$, for the Betts2D-10A cluster and the shifted points, $\vec{k} + \vec{\phi}$, sampled by an equi-spaced grid of 16 TBC phases.

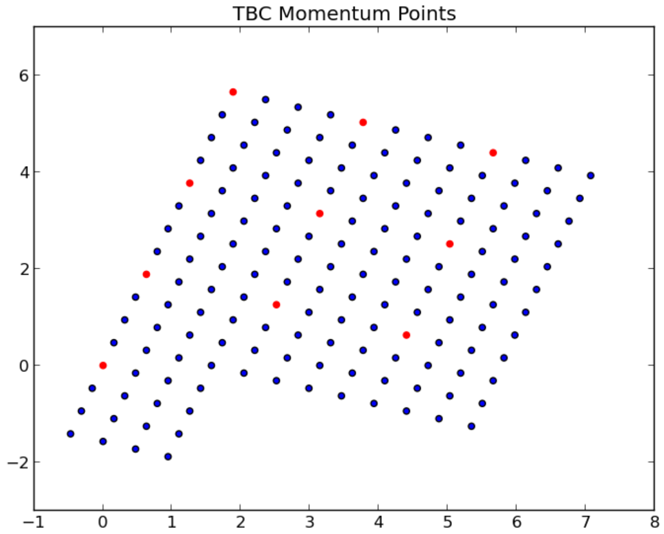

5

Figure 3.3: Illustration of the momentum points, $\vec{k}$, corresponding to the Betts-10A cluster (red) and the momentum points effectively sampled, $\vec{k}+\vec{\theta}$ by 16 twisted boundary conditions (blue).

3.5 Green's Functions

We have seen that at the level of the Hamiltonian, the net change to the Hubbard model upon applying TBC is to modify the single particle dispersion, $\epsilon(\vec{k})$.

$$\epsilon(\vec{k}) \to \epsilon_{\vec{\phi}}(k) = \epsilon(\vec{k}+\vec{\phi}) \tag{3.51}$$

We would like to know what the consequence of this change is on the Hubbard model Green's functions, since imaginary time Green's functions in real space are the primary elements used in the CT-AUX algorithm [105, 91]. In particular, the central quantity updated throughout the CT-AUX QMC algorithm is a matrix of such Green's functions, $N_\sigma(\{i, s_i, \tau_i\})$.

$$\begin{aligned} N_\sigma^{-1} &= e^{\Gamma_\sigma} - G_{0\sigma}\left(e^{\Gamma_\sigma}-1\right) \\ e^{\Gamma_\sigma} &= diag\left(e^{\gamma s_{i_1}\sigma}, e^{\gamma s_{i_2}\sigma}, \ldots, e^{\gamma s_{i_n}\sigma}\right) \\ \left(G_{0\sigma}\right)_{ab} &= g_{0 i_a i_b \sigma}(\tau_a - \tau_b) \end{aligned} \tag{3.52}$$

The N matrix is constructed and updated throughout the Markov Chain Monte

Carlo process based on the current configuration of sites, auxiliary spins, and imaginary times being sampled, $\{i, s_i, \tau_i\}$. The Green's functions included in the N matrix, $g_{0i_ai_b\sigma}(\tau_a - \tau_b)$, are the iteratively determined cluster bare Green's functions computed during the DCA self-consistency loop. That is, they are not simply non-interacting Green's functions on the cluster, but also incorporate the effects of coupling to the bath in which the cluster is embedded [14, 105].

An important detail for implementing the CT-AUX algorithm is determining whether or not these Green's function, and therefore N_σ, are real or complex valued. Let's illustrate this with the lattice non-interaction Green's function, which is easily found from the Hamiltonian in Matsubara frequencies and momentum space. We drop the vector symbols for the momentum and phase vectors.

$$G_0(k, i\omega_n) = \frac{1}{i\omega_n - \epsilon_\phi(k)} \tag{3.53}$$

We can then Fourier transform from Mastubara frequencies to imaginary time, τ.

$$G_0(k, \tau) = \frac{1}{\beta} \sum_n e^{-i\omega_n \tau} \frac{1}{i\omega_n - \epsilon_\phi(k)} \tag{3.54}$$

The sum over Matsubara frequencies can be performed via contour integration. The result for the non-interacting Green's function in imaginary time and momentum space is,

$$G_0(k, \tau) = -e^{-\epsilon_\phi(k)\tau}(1 - n_F(\epsilon_\phi(k)), \tag{3.55}$$

where $n_F(x) = (1 = e^{\beta\epsilon_\phi(k)})^{-1}$ is the Fermi function. We now transform into real space to obtain an expression for $G_0(x, \tau)$.

$$G_0(x, \tau) = -\frac{1}{N} \sum_k e^{ikx} e^{-\epsilon_\phi(k)\tau}(1 - n_F(\epsilon_\phi(k)) \tag{3.56}$$

We can now check if $G_0(x, \tau) = G_0^*(x, \tau)$, which occurs only if $G_0(x, \tau)$ is real. If we conjugate the above expression and substitute $k \to -k$, we obtain the following.

$$G_0^*(x, \tau) = -\frac{1}{N} \sum_k e^{ikx} e^{-\epsilon_\phi(-k)\tau}(1 - n_F(\epsilon_\phi(-k)) \tag{3.57}$$

Comparing these two expressions, we find that $G_0(x, \tau)$ is real if the dispersion is symmetric under the transformation $k \to -k$, $\epsilon_\phi(k) = \epsilon_\phi(-k)$. The dispersion for the 2D Hubbard model on a square lattice is,

$$\epsilon_\phi(k) = -2t\left(\cos(k_x + \phi_x) + \cos(k_y + \phi_y)\right). \tag{3.58}$$

Inspection of this dispersion reveals that the symmetry condition is only satisfied when $\phi = 0$, which corresponds to periodic boundary conditions. Thus, for arbitrary TBC phase angles we expect the non-interacting Green's function, and therefore also the N_σ matrices, to be complex.

3.6 Algorithm Modifications

The complex valued nature of $G(x,\tau)$ when using TBC has a few important numerical consequences. For example, care must be taken during the Monte Carlo updates to accumulate the average phase, rather than the average sign, and Fourier transforms cannot use shortcuts that apply when functions are known to be real.

3.6.1 Complex Phase Problem

We use Markov Chain Monte Carlo [110, 105] to sample the terms in the partition function expansion generated by the CT-AUX algorithm.

$$\begin{aligned} Z &= \sum_{k=0}^{\infty} \sum_{i_k,\ldots i_1} \sum_{s_{i_k},\ldots s_{i_1}=\pm 1} \int_0^\beta d\tau_1 \ldots \int_{\tau_{k-1}}^\beta d\tau_k \left(\frac{K}{2N\beta}\right)^k Z_k\left(\{i_j, s_{i_j}, \tau_j\}\right) \\ &= \int \rho(x) dx \end{aligned} \tag{3.59}$$

In the above $x = \{i, s_i, \tau_i\}$, and the last integral is understood to stand in for sums and interactions over all these degrees of freedom. The terms of the series are expressed in terms of the N matrices.

$$\frac{Z_k}{Z_0} = \prod_{\sigma=\uparrow,\downarrow} \det N_\sigma^{-1} \tag{3.60}$$

If we interpret the terms in the partition function as a probability distribution function, $\rho(x)$, we can efficiently sample this configuration space via a Markov Chain.

If the Markov Chain generates configurations according to $\rho(x)$, then we can compute Monte Carlo results for observables, $\mathcal{O}$, as follows.

$$\begin{aligned}\langle \mathcal{O} \rangle &= \frac{\int \mathcal{O}(x)\rho(x)dx}{\int \rho(x)dx} \\ &= \lim_{N\to\infty} \frac{1}{N}\sum_{i=1}^{N} \mathcal{O}(x_i)\end{aligned} \tag{3.61}$$

A small problem is this case is that our probability distribution is given by terms in a partition function expansion,

$$\rho(x) = \left(\frac{K}{2N\beta}\right)^k Z_k\left(\left\{i_j, s_{i_j}, \tau_j\right\}\right) d\tau_1 \dots d\tau_k/Z, \tag{3.62}$$

that are not necessarily positive and in the case of TBC are not even real valued, since $Z_k \alpha \det N^{-1}$. Thus, we need to sample according to the absolute value of these terms, $\rho(x) = \|\rho(x)\| \, e^{i \arg \rho(x)}$. This allows us to apply our Markov Chain techniques as the cost of introducing a need quantity, the average phase, that must be accounted for through out the process.

With this change, our Monte Carlo expressions for observables takes on the following form.

$$\begin{aligned}\langle \mathcal{O} \rangle &= \frac{\int \mathcal{O}(x)\, \|\rho(x)\|\, e^{i \arg \rho(x)} dx}{\int \|\rho(x)\|\, e^{i \arg \rho(x)} dx} = \frac{\int \mathcal{O}(x)\, \|\rho(x)\|\, e^{i \arg \rho(x)} dx}{\int \|\rho(x)\|\, dx} \Big/ \frac{\int \|\rho(x)\|\, e^{i \arg \rho(x)} dx}{\int \|\rho(x)\|\, dx} \\ &== \lim_{N\to\infty} \frac{1}{N}\sum_{i=1}^{N} \mathcal{O}(x_i) e^{i \arg \rho(x_i)} \Big/ \lim_{N\to\infty} \frac{1}{N}\sum_{i=1}^{N} e^{i \arg \rho(x_i)} \\ &= \left\langle \mathcal{O}(x) e^{i \arg \rho(x)} \right\rangle_{\|\rho(x)\|} \Big/ \left\langle e^{i \arg \rho(x)} \right\rangle_{\|\rho(x)\|}\end{aligned} \tag{3.63}$$

During a Monte Carlo calculation we accumulate the values of $\mathcal{O}(x)e^{i \arg \rho(x)}$ and $e^{i \arg \rho(x)}$, and then divide these quantities at the end of the computation to report a result. $\left\langle e^{i \arg \rho(x)} \right\rangle_{\|\rho(x)\|}$ is referred to as the average phase, and is simply the complex analogue of the average sign. Monte Carlo calculations run into trouble whenever the average phase (sign) is small, as this results in very large uncertainties for observables. [112]

3.7 Application of TBC to Hubbard Model

The following describes the results of three different methods that were used to explore the possible benefits of using Twisted Boundary Conditions (TBC) to study the single band, $V = 0$ Hubbard model. The first and simplest method was via exact diagonalization, both through the development of Python diagonalization program and the modification of and existing C++ program, Pomerol, [122] to accommodate the complex intersite hopping, $t_{ij} \to t_{ij} e^{i\vec{\theta}\cdot(\vec{i}-\vec{j})}$. This provides a useful testing ground for TBC, but is very limited in both the system size it can handle and by the isolated nature of the cluster, i.e., unlike DMFT, there is no coupling to a mean field bath to simulate the lattice environment of the thermodynamic system [81]. The second method used the DMFT self-consistency method to account for temporal fluctuations by using second order perturbation [91] to solve the impurity problem. While this allows us to gain the benefits of DMFT while maintaining simplicity, many strongly correlated problems, including the Hubbard model beyond small U, are beyond the regime of validity of perturbation theory. The third and last method was to modify the CT-AUX algorithm for use as the impurity solver with TBC. This last method should be the most accurate, as it provides a numerically exact solution for the impurity problem.

The next two sections will introduce the formalism behind exact diagonalization and second order perturbation theory. The modifications to the CT-AUX algorithm were applied as described earlier in this chapter.

3.7.1 Exact Diagonalization

One way to solve a quantum mechanical system defined by a Hamiltonian H is to find all of the stationary states, $|\psi_n>$, with energy eigenvalues, E_n.

$$H|\psi_n >= E_n|\psi_n >$$

Since the Hubbard model is discrete, the number of states is finite and we obtain a regular matrix eigenvalue problem. If we find the eigenenergies and eigenstates of the system, then we can construct the partition function, Z, and calculate any observable for the system exactly.

Given how quickly the number of states increases with the system size and the computational expense of the eigenvalue problem, this method of exact diagonalization will only be possible for rather small systems. In fact, the largest Hubbard systems that have been solved in this manner had around 18 sites [123]. However, the simplicity and exactness of the method still provides a useful environment for experimenting with new ideas and building intuition.

Aside from the restriction to small systems, the major technical challenges in implementing an exact diagonalization program are: 1) representing many particle states and 2) constructing the Hamiltonian matrix.

An arbitrary state in the Hubbard model can be represented by a collection of creation operators operating on the vacuum state, $|0>$, representing a system with no electrons in it. Let's define $c^\dagger_{i\sigma}$ ($c_{i\sigma}$)as the creation (annihilation) operator that creates (destroys) an electron on lattice site i with spin σ, which can be either up or down. Since these are fermion operators, they obey anti-commutation relations, [3]

$$\{c^\dagger_{i\sigma}, c_{j\sigma'}\} = \delta_{ij}\delta_{\sigma\sigma'},$$
$$\{c^\dagger_{i\sigma}, c^\dagger_{j\sigma'}\} = \{c_{i\sigma}, c_{j\sigma'}\} = 0.$$

These relationships require us to define an ordering of operators convention for states, since different sequences of the same creation operators may differ by a negative sign. Let us say that a state is defined, with a positive sign, by ordering creation operators first by spin and then by lattice site. For example, the state $|\psi>$ with an up electron on site 3 and two down electrons on sites 1 and 4 would be written as

$$c^\dagger_{3\uparrow}c^\dagger_{1\downarrow}c^\dagger_{4\downarrow}|0>$$

We can represent states for a single orbital Hubbard model with N sites on a computer with bit strings of length $2N$. [124] This is done by mapping each single particle state with one bit in the string. There are $2N$ such single particle states, since each site can have an up and a down electron. Bit $b_{i\sigma}$ is 1 if site i has an electron with spin σ, and 0 otherwise. The ordering of the bits in the string is,

$$b_{1\uparrow}b_{2\uparrow}...b_{N\uparrow}b_{1\downarrow}...b_{N\downarrow}.$$

Thus, the state $|\psi>$ above would be represented as (assuming $N = 4$),

$$|\psi>= c^\dagger_{3\uparrow}c^\dagger_{1\downarrow}c^\dagger_{4\downarrow}|0>= 00101001.$$

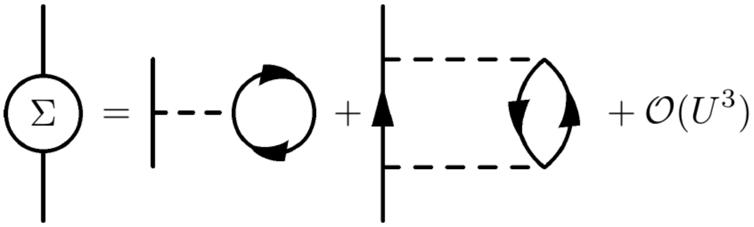

Figure 3.4: Diagrams that contribute to the second order self-energy. Figure from Ref. [17].

With this representation we can implement the effect of operators on states with bit-wise operations. (Though we also need to be careful with a possible sign change, depending on how many operators need to be commuted.) This allows us to explicitly calculate all the matrix elements of the Hamiltonian. This matrix can then be diagonalized with any numerical linear algebra library.

However, since the size of this matrix increases exponentially in the size of the system, it is a good idea to think about how the matrix might be broken up into pieces that can be diagonalized individually. The most common way to do this is to identify the symmetries of the Hamiltonian and use them to block diagonalize the matrix. In particular, the Hubbard model Hamiltonian has translation symmetry and particle number conservation, so states can be classified by momentum and particle number, in addition to energy. These states do not couple to each other, and so they can be used to block diagonalize the Hamiltonian. This decreases the cost of diagonalization and makes it easier to identify the momentum of each of the resulting eigenstates.

The method of exact diagonalization is useful because it is both exact and yields easy access to all observables, since the eigenvalues and states are determined. However, the exponential growth in the size of the state space limits this algorithm to very small systems. This means that although it may be useful for exploring new ideas, in order to investigate the physics of realistic systems we need a justifiable approximation method that cuts down computational complexity.

3.7.2 Second Order Perturbation Theory

One widely used approximation is to calculate the self-energy of an electron system with perturbation theory. The first order self-energy is known as the Hartree term, and corresponds to a simple mean field treatment of the system and contains no frequency or momentum dependence. A common treatment that starts to capture some of the dynamics of the system is second order perturbation theory [3, 91].

The diagrams contributing to the second order self-energy are shown in Figure 3.4. They can be evaluated to obtain the expression,

$$\Sigma_k(\nu) = \frac{Un}{2} - \frac{U^2}{\beta^2} \sum_{\nu' \omega k' q} G_{k'}(\nu') G_{k'+q}(\nu' + \omega) G_{k+q}(\nu + \omega).$$

Where $\beta = 1/k_B T$, T is the temperature, and k_B is Boltzmann's constant. This expression requires $\mathcal{O}(N_k^3 N_\omega^3)$ operations to compute. However, we can dramatically decrease this cost by noticing that the sum can be written as,

$$\Sigma_k(\nu) = \frac{Un}{2} - \frac{U}{\beta^2} \sum_{\omega q} P_q(\omega) G_{k+q}(\nu + \omega),$$

$$P_q(\omega) = \sum_{k'\nu'} G_{k'}(\nu') G_{k'+q}(\nu' + \omega).$$

$P_q(\omega)$ is known as the polarization bubble, and by calculating this quantity once and for all at the beginning of the calculation the cost of evaluating the self-energy decreases to $\mathcal{O}(N_k^2 N_\omega^2)$.

These formulas seem straightforward to evaluate, but the analytic properties of the Green's function require that some care is taken in calculating the sums. In particular, the Green's function in imaginary time, $G(\tau)$, is anti-periodic and has a discontinuity at $\tau = 0$. This means that something extra must be done to accurately capture the high frequency behavior of the Green's function [24].

This is relevant because the high frequency components of the Green's function are involved in the calculation of the second order self-energy in two places. One is in the calculation of the density, n, which is given by an infinite sum,

$$n = \frac{1}{\beta} \sum_{k\nu} G_k(\nu).$$

The other is in the calculation of the polarization bubble, since it also involves a sum over all frequency components of a product of Green's functions.

The first step in addressing these issues is to write down a high frequency expansion [24] for the Green's function,

$$G_k(i\omega_n) = \frac{c_1(k)}{i\omega_n} + \frac{c_2(k)}{(i\omega_n)^2} + \mathcal{O}\left(\frac{1}{(i\omega_n)^3}\right).$$

The coefficients $c_1(k)$ and $c_2(k)$ can be obtained from the following expression for the Green's function, [3]

$$G_k(i\omega_n) = \sum_{m\geq 0}(-1)^m \frac{< T_\tau\{[H, c_k]_{\{m\}}, c_k^\dagger\} >_\tau}{(i\omega_n)^k}.$$

Using this formula, we see that the high frequency coefficients (c_1, c_2) can be obtained by evaluating commutators of the Hamiltonian with the creation and annihilation operators. These calculations, while tedious, are straightforward. For the single band, on-site interacting Hubbard model one obtains,

$$c_1(k) = 1,$$

$$c_2(k) = Un_k + \epsilon(k) - \mu.$$

Now, if we define G_k^{hf} as,

$$G_k^{hf}(i\omega_n) = \frac{c_1(k)}{i\omega_n} + \frac{c_2(k)}{(i\omega_n)^2}.$$

Then we can split the full Green's function into two components

$$G_k(i\omega_n) = G_k^{hf}(i\omega_n) + \tilde{G}_k(i\omega_n)$$

We have done nothing more than rearrange terms here. However, $G_k^{hf}(i\omega)$ is a known function that can be analytically summed over all Matsubara frequencies, while $\tilde{G}_k(i\omega_n)$ contributes very little (compared to $G_k^{hf}(i\omega)$) at large frequencies.

This allows us to calculate the density much more accurately than we would with a simple truncated sum,

$$n_k = \frac{1}{\beta}\sum_{\omega_n} G_k(i\omega_n) = \frac{1}{\beta}\sum_{\omega_n}\tilde{G}_k(i\omega_n) + 0.5 - \frac{c_2(k)}{4\beta}.$$

This treatment of the Green's function also affects the calculation of the polarization bubble, which in turn influences the self-energy. This is important because a 'real' self-energy should have an imaginary part that is negative-definite, a result that follows from causality and the Kramers-Kronig relations. Whether or not this is true numerically is influenced by how the truncation of frequency sums is handled.

Second order perturbation theory allows us to tackle much larger system sizes than exact diagonalization. However, implemented as demonstrated so far, it is still limited to finite clusters that may not accurately represent thermodynamic ($N \to \infty$) physics. More importantly, it is doomed to failure once the interactions between electrons, U, become too large.

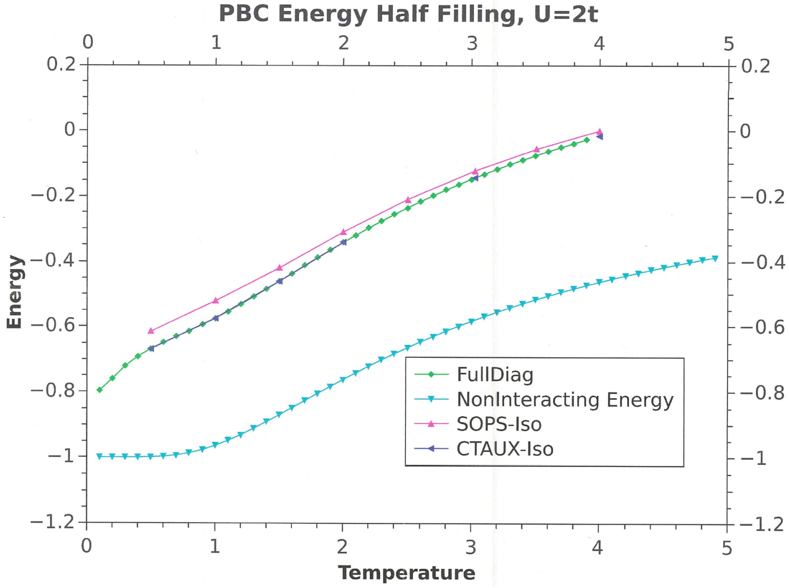

Figure 3.5: Comparison of the energy versus temperature curves for an isolated cluster at half-filling obtained via exact diagonalization (FullDiag), DMFT with a second order perturbation theory impurity solver (SOPS-Iso), and DMFT with a modified CT-AUX algorithm (CTAUX-Iso). Also shown is the analytic result for the non-interacting, $U = 0$, system. Exact diagonalization and DMFT with CTAUX agree perfectly as expected, since CTAUX solves the impurity problem exactly and in this case there is no coupling to an external bath. Second order perturbation theory do fairly well at this low interaction strength, but the approximations begins to break at lower temperatures.

3.7.3 Method Comparisons and Preliminary Results

In this section we present some of the calculations performed to check and compare the outputs from exact diagonalization (ED), DMFT + second order perturbation theory (SOPS), and DMFT + CTAUX (CTAUX). We also present some preliminary results on the convergence of system energies with cluster size and number of averaged twisted boundary conditions. Most of these calculations were performed for isolated Hubbard clusters, where there is no self-consistent coupling to a mean field bath. Although this means that the DMFT self-consistency condition is unnecessary, it simplifies our analysis by allowing us to focus on the behavior and correctness of the impurity solvers. Establishing that the TBC methodology is correct and beneficial in the isolated cluster case is necessary for proceeding to its use in the DCA self-consistency framework.

Figures 3.5, 3.6, and 3.7 show tests meant to confirm that all three methods yielded the same results for the base case, periodic boundary conditions ($\vec{\phi} = 0$). Figure 3.5 shows the energy versus temperature curves obtained for an isolated cluster at $U = 2t$. The non-interacting energy is also shown for comparison. As expected the ED and CTAUX results agree perfectly, since the isolated cluster problem is identical to the impurity problem, which is numerically solved exactly by the CTAUX Monte Carlo scheme. SOPS also performs fairly well since this is a weak interaction strength at which perturbation theory is applicable, although the perturbation error begins to appear as the temperature is lowered.

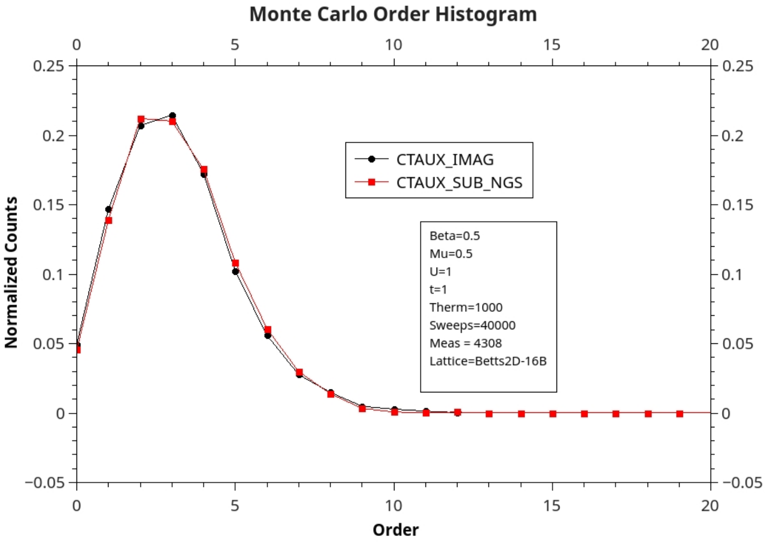

Figure 3.6: Check of the modified CT-AUX algorithm by comparing the order histogram generated by the original code, "CTAUX_SUB_NGS", and the code modified to work with twisted boundary conditions, "CTAUX_IMAG".

Figures 3.6 and 3.7 compare the results of a simulation at $\beta = 0.5$, $\mu = 0.5$, $U = 1t$, on a 16 site Betts cluster with PBC between the modified and original CTAUX algorithms. This check is meant to ensure that no errors have been introduced into the CTAUX program that would cause the normal (PBC) results to disagree. The histogram, Fig. 3.6, shows that both methods sample diagrams during the Monte Carlo simulation with the same distribution of orders, k. Fig. 3.7 confirms that both methods produce the same single particle Green's functions. Shown is the imaginary part of $G(i\omega_n, k = (0, 0)$.

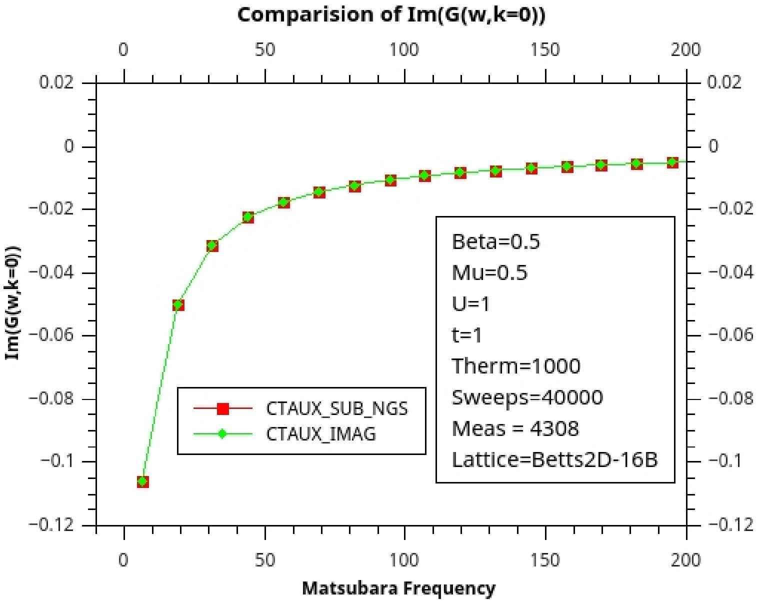

Figure 3.7: Check of the modified CT-AUX algorithm by comparing the imaginary part of the $k = (0, 0)$ Matsubara Green's function generated by the original code, "CTAUX_SUB_NGS", and the code modified to work with twisted boundary conditions, "CTAUX_IMAG".

We now move on to exploring how TBC affects the convergence of the system energy. The simplest test is to compare how the energy of the non-interacting Hubbard model behaves as a function of cluster size and number of twisted boundary conditions since the analytic result is known. In the thermodynamic limit, the energy of the non-interacting system, E, can be expressed in terms of the momentum space resolved electron density, $n_\sigma(k)$, and the single particle dispersion, $\epsilon(k)$.

$$E = \sum_\sigma \int dk \epsilon(k) n_\sigma(k) \tag{3.64}$$

For the 2D single band non-interacting Hubbard model, the dispersion and density are given as follow.

$$\epsilon(k) = -2t \sum_{i=1}^{2} \cos(k_i) - \mu \tag{3.65}$$

$$n_\sigma(k) = \frac{1}{1 + e^{\beta\epsilon(k)}} \tag{3.66}$$

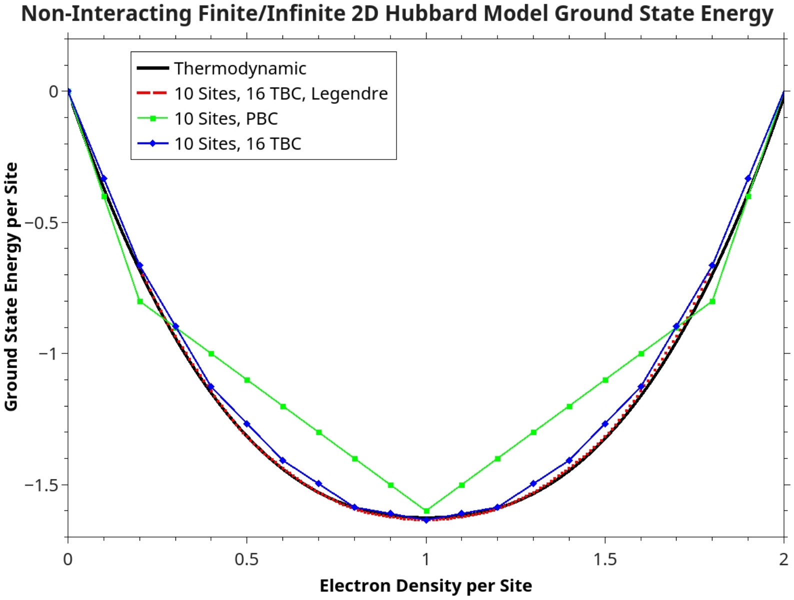

Figure 3.8: Comparison of how the ground state energy of the noninteracting Hubbard model compares between an thermodynamic (infinite) system and a 10 site cluster. Averaging over twisted boundary conditions on the finite system yields a much better approximation of the infinite system, and the Legendre method of producing an energy from the TBC data does even better.

These equations and Figures 3.8 and 3.9 can give us an intuitive understanding of why averaging over boundary conditions can yield a energy that betters approximates that of the infinite system. Consider that while Eq. 3.64 expresses the energy of the thermodynamic system as a integral over the Brillouin Zone (BZ), the momentum space for a finite cluster consists of a set of discrete momentum vectors, k_c. Thus, the finite cluster energy, E^c is given by a sum rather than an integral.

$$E^c = \sum_\sigma \sum_c \epsilon(k_c) n_\sigma(k_c) \tag{3.67}$$

Comparing Eqs. 3.64 and 3.67, we see that the cluster energy will be equivalent to a finite element approximation to the integral defining the infinite lattice energy.

Thus, if we want the cluster energy to better approximate the thermodynamic energy, we can simply increase the size of the cluster, which in turn increases the number of cluster momenta, k_c, and yields a better finite element approximation.

However, many computational techniques, such as ED and DCA, have a computational expense that scales very poorly with cluster size and can therefore make this approach intractable. [14] An alternative and potentially much cheaper strategy is to average over TBC for a single cluster rather than increasing its size. Earlier in this chapter we saw that TBC modifies the single particle dispersion by sending $\epsilon(k) \rightarrow \epsilon(k+\phi)$. If we define the cluster energy with TBC phase ϕ as E^c_ϕ, then we can try looking at the TBC averaged (TBCA) energy, E^c_{TBCA}.

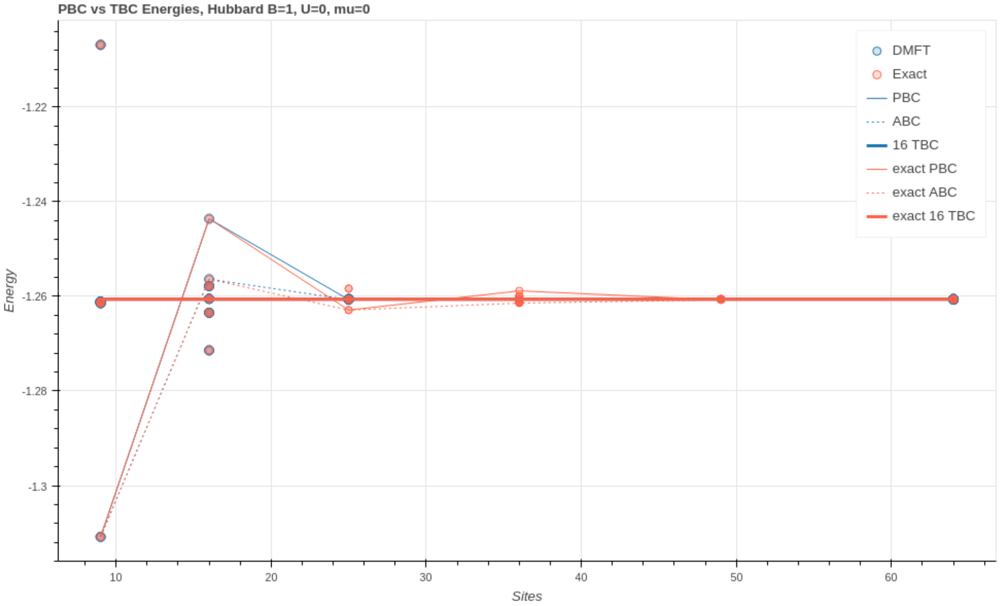

Figure 3.9: Example of how the energy converges as a function of cluster size for the non-interacting, $U = 0$, Hubbard model. PBC stands for periodic boundary conditions, ABC for anti-periodic, and TBC for an average over the energy obtained from a grid of 16 twisted boundary conditions. In this very simple case, we see that TBC immediately yields the thermodynamic energy, whereas PBC or ABC require cluster with around 40 sites in order to eliminate finite size errors.

$$\begin{aligned} E^c_{TBCA} &= \frac{1}{m}\sum_{i=0}^{m} E^c_{\phi_i} \\ &= \sum_\sigma \sum_c \frac{1}{m}\sum_{i=0}^{m} \epsilon(k_c+\phi_i) n_\sigma(k_c+\phi_i) \end{aligned} \tag{3.68}$$

Where m is the number of TBC phases used to compute the average. If we imagine that the sampled TBC phases are arranged on a uniform grid, then we see that the TBCA approach effectively increases the number of momentum points used to calculate the energy, i.e. it improves the finite element approximation to the integral for the thermodynamic energy, Eq. 3.64.

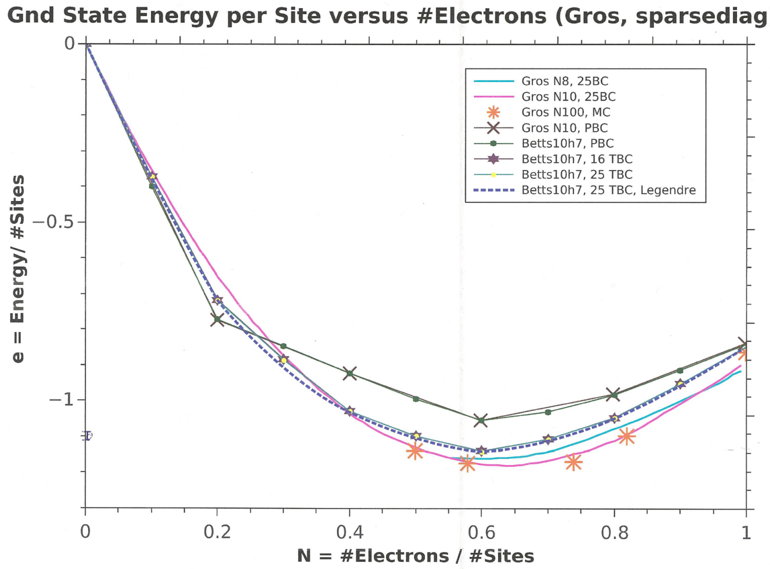

Figure 3.10: Comparison of the energy versus doping, n, for the $U = 4t$ 2D Hubbard model. This test compares results from a modified exact diagonalization program (Betts10h7) with those obtained in Ref. [18] (Gros). The finite clusters with periodic boundary conditions (PBC) yield energies far away from the thermodynamic result, but averaging over even a small number of twister boundary conditions greatly reduces the finite size effects.

Is is thus clear that we should expect the finite cluster approximation of the energy for the non-interacting Hubbard model to converge to the infinite system result as we increase the size of the cluster or as we increase the number of TBC phases. In Fig. 3.8, we see that while a 10 site cluster with PBC does a poor job of matching the energy vs density curve of the infinite system, averaging over a 4 by 4 grid of TBC produces a much better approximation.

A similar result is shown in Fig. 3.9, which shows how the various cluster and TBC phase energies behave. This figure also checks the DMFT implementation of TBC, since the non-interacting result can be easily calculated. We see that for small clusters the spread in TBC energies, E^c_ϕ, is quite wide, but that they converge very quickly as the cluster size increases. More remarkably, the TBC averaged energy agrees with the large cluster limit even for a small 9 site cluster. This is in stark contrast to the PBC energy, which fluctuates and only only starts to converge to the large cluster energy for clusters with around 25 sites. Although the non-interacting system is trivial, this already starts to show some of the potential of TBC in improving estimates of large system size energies without the steep computational cost of simulating larger clusters.

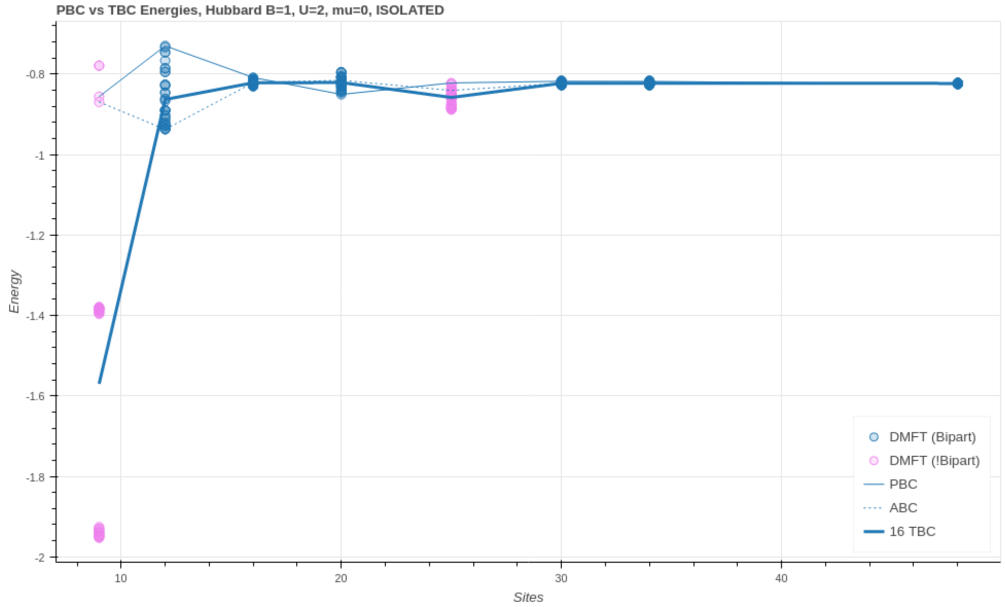

Figure 3.11: Example of how the energy converges as a function of cluster size for the an isolated $U = 2$ Hubbard cluster at $\beta = 1$. One key observation from this graph is that non-bipartite clusters (pink) yield large finite size effects, and so extrapolations should be limited to bipartite clusters (blue).

We now turn to the use of TBC in studying interacting systems. In Fig. 3.10, we compare the energy vs density curves for a $U = 4t$ Hubbard model obtained via ED to published results by Gros [18]. We again see that even outside the non-interacting limit, TBC can be used to significantly reduce finite size effects. In this case we see that a 10 site cluster can be used to obtain close to thermodynamic results, in this case by averaging over just 16 or 25 TBC phases. Since the state space of the Hubbard model scales as 4^{N_c}, where N_c is the number of cluster sites, exact diagonalization is too expensive to perform on Hubbard clusters much larger than 10 sites. In comparison, TBC simply requires running the same calculation with different TBC phases, and so the added computational expense is just linear in the number of phases.

Fig. 3.10 also demonstrates two different ways of computing observables with TBC. In addition to the above described TBCA, which consists of simply averaging over the results from simulations with different TBC phases, one can also use a technique known as Integration Over Boundary Conditions (IBC, referred to as Legendre in the figures). As described in Ref [18] the IBC method provides a means of computing the ground state energy in the grand canonical ensemble, which alleviates the challenge that arises in ED studies of working with a constant, integer electron number. We do not pursue this method further, however, because this is only a significant advantage for ED studies and we found the differences between TBCA and IBC to be slight.

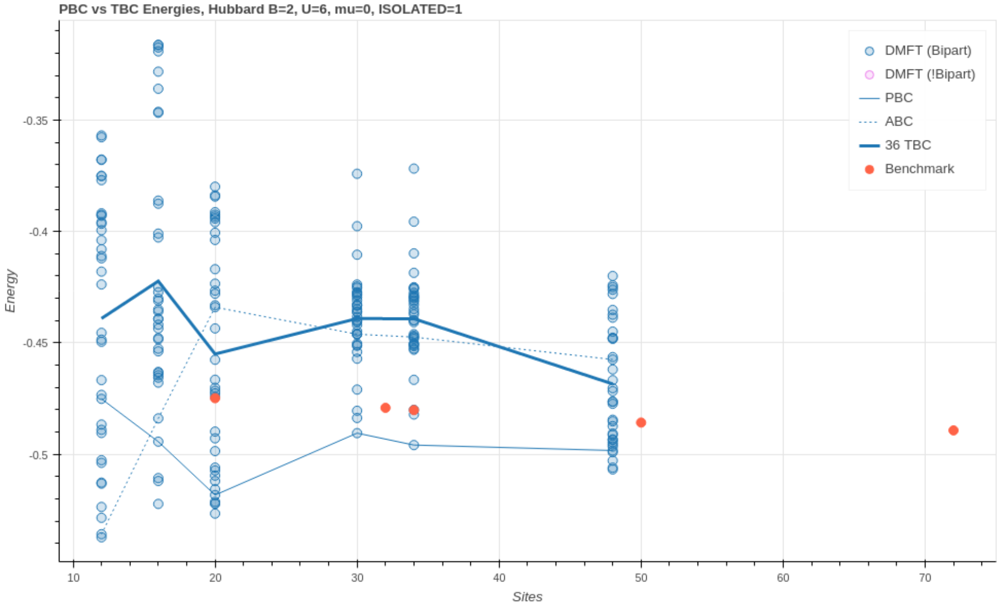

Figure 3.12: Example of how the energy converges as a function of cluster size for the an isolated $U = 6$ Hubbard cluster at $\beta = 2$. Periodic, anti-periodic, and TBC energies are compared to benchmark energies computed in Ref. [19].

Figures 3.11 and 3.12 present results obtained for isolated, interacting Hubbard clusters with a modified version of the CT-AUX algorithm. Since these clusters are not coupled to a self-consistently determined bath, they rely only on the numerically exact impurity solver, rather than the DMFT self-consistency cycle.

Figure 3.11 shows the energies obtained from CT-AUX for a wide range of cluster sizes from 16 TBC phases. We see that this high temperature and low interaction strength ($U = 2t$, $\beta = 1$) the TBCA result for the energy seems to converge slightly faster than the PBC result, as a function of cluster size. Although this improvement is only significant for small clusters, one important finding from these results is the importance of cluster geometry. We find that non-bipartite clusters results in a much larger spread of TBC energies, possibly due to the strong anti-ferromagnetic fluctuations that exist in the Hubbard model at weak interaction strengths. [14] Bipartite clusters are those whose sites can be classified as two types, A or B, and in which A sites only border B sites and vice-versa. It is well known that strong discrepancies can occur in simulations when the cluster geometry is incommensurate with the physical fluctuations of the model.

Figure 3.12 presents similar results for a much stronger interaction strength, $U = 6$. Unfortunately these results are much more nebulous, as it is not clear that the TBCA method provides any significant improvement in scaling over PBC. Although the previous tests indicate that the modifications to the CT-AUX algorithm are correct, it is possible that the lackluster performance of TBCA is due to some error that only manifests at large interaction strengths. It will be a matter for future study to determine if this is the case, or if the TBCA framework is simply inapplicable far away from the non-interacting limit.

Chapter 4

Charge Order

This chapter describes work related to studying charge order as it occurs in the 2D extended Hubbard model. It contains results on the behavior of the charge order transition away from half-filling, as well as a detailed study of the competition between charge order and antiferromagnetism. In addition, a detailed derivation of a numerical technique, known as submatrix updates, implemented for the modified CT-AUX algorithm used to study charge order is presented.

4.1 Introduction

Much of the initial work on strongly correlated systems, especially that done in with the DMFT framework, have focused on local interactions and correlations. For example, the most commonly studied version of the Hubbard model only includes the interaction between different spin electrons occupying the same lattice site [125, 16]. This focus on local correlations both makes the problem easier and is often justifiable, as there are many instances in which local interactions drive the physics of strongly correlated system. Indeed, one the motivators behind single site DMFT was the observation that in the limit of infinite dimensions (or infinite coordination number for a lattice model), the self-energy becomes purely local quantity [102, 126, 127, 81]. Furthermore, the simplest Hubbard model exhibits the Mott insulator transition, superconductivity, antiferromagnetism, and pseudogap behavior, all with only local interactions accounted for [81, 128, 14, 129].

However, the Coulomb interaction is naturally a long range interaction, and it is unsurprising that it can give rise to phenomena not captured by local approximations. One such phenomena is charge order, a ubiquitous symmetry broken phase exhibited by many strongly correlated systems that arises from non-local interactions. This phase is characterized by an inhomogenous and periodic distribution of electric charge throughout the system, often in the form of striped or checkerboard patterns [130]. Compounds that exhibit charge order (CO) often also exhibit antiferromagnetic (AFM) phases [47, 131, 11]. Examples include the *d*-electron material $La_{1-x}Sr_xFeO_3$,[132] the doped nickelate $La_{2-x}Sr_xNiO_4$,[76] the layered manganite $La_{0.5}Sr_{1.5}MnO_4$,[133] the cobalt oxides[134], the doped iridate [135], the layered ruthenate [136] and the layered cuprates $La_{2-x}Sr_xCuO_4$ and $La_{2-x}Ba_xCuO_4$ at 1/8 doping [137]. Organic salts, including the one-dimensional $(TMTTF)_2SbF_6$ [138, 139, 140, 141] and two-dimensional quarter filled compounds [142, 143, 144] similarly show coexisting AFM and CO. Several of these materials are also superconducting. Understanding the phase diagram in these materials requires a detailed analysis of the competition between these two types of ordering [145, 80].

4.2 Application to the 2D Extended Hubbard Model

One of the simplest systems to display strong magnetic correlations is the Hubbard model, which has become the archetype of strongly correlated electron systems [146]. The model approximates the band structure by a single band with nearest-neighbor hopping parameter t, and the Coulomb effects by a local interaction U. The two-dimensional version of the model, while exhibiting strong antiferromagnetic fluctuations over much of the phase diagram (see *e.g.* Refs. [147, 148] for recent work) is known to have a charge ordered ground state in parts of the phase diagram [149].

The extended Hubbard model promotes charge order by explicit addition of a repulsive nearest-neighbor interaction term V. In the half-filled model, this will make it energetically favorable to break translational symmetry and generate a state with two electrons on one site, none on its neighbors, and a repeating (π, π) charge ordered pattern. In contrast, a large on-site interaction U will enhance antiferromagnetic (π, π) correlations. The interplay of V, U, temperature, doping, and bandstructure effects thereby generates the rich phase diagram of the model.

In the following sections, we explore the two-dimensional half-filled extended Hubbard model at non-zero temperature in the DCA approximation. This approximation allows both for long ranged charge and spin ordered states, and treats them on an equal footing. We use the model and approximation as a proxy to study the interplay between these phases, and to analyze how the extent of the phases changes as a function of U, temperature, and V.

4.3 Model and Methods

This work applies the methods developed in Ref. [23] to study to behavior of charge order away from half filling and the formation and competition between AFM and CO phases in the half filled 2D extended Hubbard model. The following provides an overview of the formalism, and the interested reader is referred to [23] for further details.

The Hamiltonian for the extended Hubbard model on a two-dimensional square lattice is given by

$$\begin{aligned} H = -t \sum_{\langle ij \rangle, \sigma} \left(c^{\dagger}_{i\sigma} c_{j\sigma} + c^{\dagger}_{j\sigma} c_{i\sigma} \right) + U \sum_{i} n_{i\uparrow} n_{i\downarrow} \\ + \frac{V}{2} \sum_{\langle ij \rangle, \sigma\sigma'} n_{i\sigma} n_{j\sigma'} - \tilde{\mu} \sum_{i\sigma} n_{i\sigma}, \end{aligned} \tag{4.1}$$

where t is the nearest-neighbor hopping amplitude, U and V represent the on-site and nearest neighbor Coulomb interactions, and $\tilde{\mu}$ denotes the chemical potential. $c^{\dagger}_{i\sigma}(c_{i\sigma})$ is the creation (annihilation) operator for a particle with spin σ on lattice site i, and the particle number operator for site i is $n_{i\sigma} = c^{\dagger}_{i\sigma} c_{i\sigma}$. Half filled occurs at $\tilde{\mu} = \mu_{\mathrm{HF}} = \frac{U}{2} + 4V$ for the 2D square lattice. We use dimensionless units U/t, V/t, βt, and μ/t, and set $t = 1$.

We use the Dynamical Cluster Approximation (DCA) [150, 14] to find approximate solutions for the lattice model. The DCA is a cluster extension of Dynamical Mean Field Theory (DMFT) that maps the lattice problem onto a finite sized cluster (i.e. impurity) that is coupled to a non-interacting bath. The coupling to the bath is found via an iterative scheme that attempts to fulfill a self-consistently condition. In the case of DCA, this condition is formulated by course graining the Brillouin zone into N_c momentum space patches, and demanding that impurity quantities (such as the self energy) match the corresponding patch averaged quantities from the lattice model. In this paper we study systems with $N_c = 8$.

The DCA scheme becomes exact in the limit where $N_c \to \infty$, and the DMFT is recovered when $N_c = 1$. The method is able to describe short-ranged spatial correlations non-perturbatively (i.e. correlations on length scales smaller than N_c), but correlations outside the cluster are neglected. The method is also capable of simulating ordered phases directly, as long as the symmetry breaking is commensurate with the impurity cluster [14, 151]. An important detail is that for the extended Hubbard model the DCA coarse-graining procedure renormalizes the nearest neighbor interaction V as $\bar{V} = \sin(\pi/N_c)/(\pi/N_c)V$, as described by Ref. [107] and Ref. [108].

We can study ordered phases by adding a symmetry breaking term to the Hamiltonian. [14] These terms involve extending Eq. (4.1) via staggered chemical potential $\mu_i = \mu_{0\sigma} e^{iQr_i}$:

$$H_{\mu_0} = H + \sum_{i\sigma} \mu_{i\sigma} n_{i\sigma} \tag{4.2}$$

where Q describes the symmetry of the ordered phase and $Q = (\pi, \pi)$ for both antiferromagnetism and checkerboard charge order. This staggered chemical potential divides the original bipartite lattice into two sub-lattices A and B with $\mu_{i\sigma} = \pm\mu_{0\sigma}$ for sub-lattice $A(B)$ respectively, thereby doubling the unit cell. Antiferromagnetism is described by $\mu_{0\uparrow} = -\mu_{0\downarrow}$, while charge order is described by $\mu_{0\uparrow} = \mu_{0\downarrow}$. In this paper, we begin simulations with a small $\mu_{0\sigma}/t \approx 0.05$ on the first iteration and then set $\mu_{0\sigma}/t = 0$ on subsequent iterations. After this the system is allowed to evolve freely, and will either converge to a paramagnetic state (electrons uniformly distributed by lattice site and spin) or tip into one of the ordered states.

In this work we solve the cluster impurity problem in the DCA self-consistency cycle with the continuous time auxiliary field quantum Monte Carlo algorithm (CTAUX) [152], modified to accommodate non-local density-density interactions. The CTAUX algorithm is described in Ref. [25, 24] and the details on the modifications can be found in Ref. [23].

4.4 Application to the 2D Extended Hubbard Model Away From Half Filling

The following section closely follows Terletska, Chen, Paki, and Gull, "Charge ordering and nonlocal correlations in the doped extended Hubbard model" [94].

4.4.1 Phase diagrams

We first briefly discuss the results obtained at half filling ($\mu = 0$) and presented in Ref. [23]. The phase diagram in the space of on-site interaction U and nearest neighbor interaction V shows metallic behavior for small U and small V, Mott insulating behavior for large U and small V, and charge order for large V. This basic shape of the phase diagram is consistent within a large range of methods, and in particular with recent results using extended dynamical mean field theory, [153] the GW approximation in combination with dynamical mean field theory, [21, 154] and the so-called dual boson perturbation theory [20], as shown in Fig. 4.1. In contrast to the predictions from early analytic theories, [22, 155, 156] a non-zero strength of V is required to drive the system to the ordered phase at $U = 0$. Upon increasing the interaction strength, the charge order line stays above the mean field prediction of $U = 4V$ but, at least for U/t up to 1, closely approaches it.

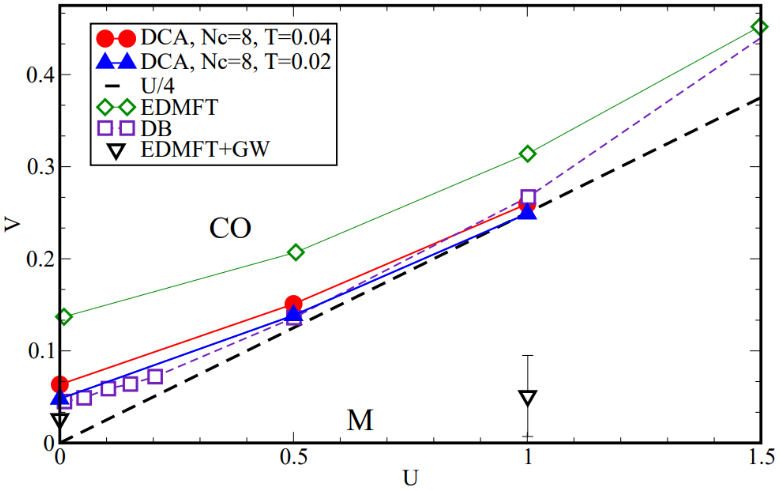

Figure 4.1: VU phase diagram of the 2D extended Hubbard model at half-filling. $N_C = 8$ DCA data obtained from the dependence of the charge order parameter versus V are shown for $T/4t = 0.04$ and $T/4t = 0.02$. Comparable results from dual bosons [20], EDMFT, and EDMFT+GW [21] are also shown. The dashed line corresponds to the U/4 phase boundary of early analytic theories [22]. Energies are shown in units of t with $4t = 1$. Figure adapted from Ref. [23].

We now turn to the doping evolution of the phase diagram. Fig. 4.2 shows the evolution of this charge order phase boundary upon varying the chemical potential μ, where $\mu = 0$ denotes the half-filled state. While the model is particle-hole symmetric around $\mu = 0$, we focus in this paper on hole doping and denote $x = 1 - n$ as doping,

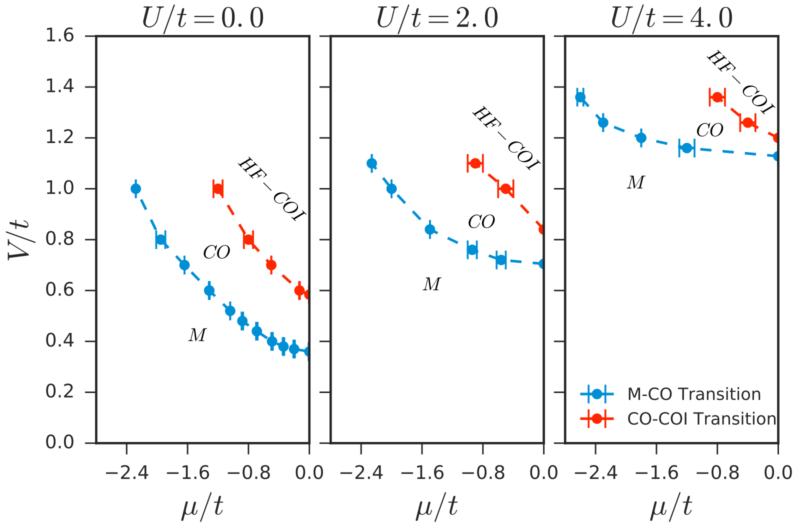

Figure 4.2: Phase diagram showing half-filled charge ordered insulator (HF-COI), charge-ordered metal (CO), and isotropic metal (M), in the space of nearest neighbor interaction V and chemical potential μ. Left panel: on-site interaction $U/t = 0$. Middle panel: $U/t = 2.0$. Right panel: $U/t = 4$. All data are obtained for cluster size $Nc = 8$ and temperature T.

where n denotes the density. Results for the system without on-site interaction ($U = 0$) are shown in the left panel. Weak ($U/t = 2$) and intermediate ($U/t = 4$) interaction strength results are shown in the middle and right panel. All results are obtained at a temperature of $T/t = 0.32$.

Consistent with Ref. [23] and earlier results, [20, 157, 21] a non-zero interaction strength of $V/t \sim 0.4$ is needed to establish charge order. As temperatures are higher than in Ref. [23], the minimal interaction strength for the onset of charge-order is larger. As the chemical potential is increased, the charge-order phase boundary shifts to larger V (blue line). Raising the on-site interaction to weak ($U/t = 2$) and moderate ($U/t = 4$) strength shifts the onset of charge order gradually to higher V.

At high interaction strength V, the charge-ordered state is an incompressible (see Fig. 4.9), half-filled band-like insulator with a large gap in the density of state. Fig. 4.2 denotes this regime as HF-COI (Half Filled Charge Ordered Insulator). This regime is separated from the uniform (isotropic) metallic phase by a compressible 'metallic' charge ordered state, which we denote as CO (red line).

At the temperatures studied, the transition from non-half-filled to half-filled state and the transition from charge-ordered to isotropic state are all continuous, i.e. second order. No jump in order parameter or hysteresis could be identified. The model

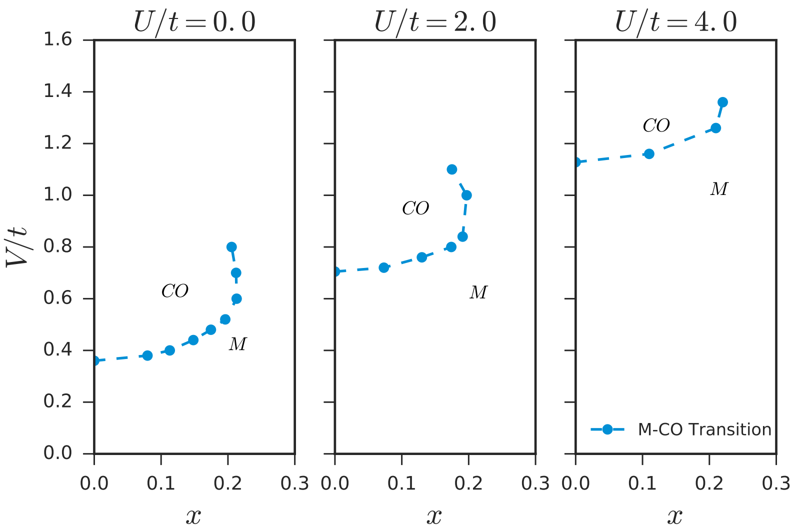

Figure 4.3: Phase diagram in the space of nearest neighbor interaction V and doping $x = 1 - n$ showing charge-ordered metal (CO), and isotropic metal (M) phases. Left panel: on-site interaction $U/t = 0$. Middle panel: $U/t = 2.0$. Right panel: $U/t = 4$. All data are obtained for cluster size $N_c = 8$ and temperature $T/t = 0.32$.

is known to exhibit first order transitions between the metallic state and the isotropic Mott insulator, both in single-site approximations to the extended Hubbard model [158] and in cluster approximations to the Hubbard model without non-local interactions [152, 129]. However, these phase transitions take place at local interaction strengths that are larger than the ones studied here.

Fig. 4.3 shows the data of Fig. 4.2 replotted against doping $x = 1 - n$ rather than chemical potential. The left panel shows $U/t = 0$, the middle panel $U/t = 2$, and the right panel $U/t = 4$. In this representation, the half-filled charge order insulating regime is compressed to the $x = 0$ line. It is evident that once the critical V for charge order is reached, a charge ordered phase is established almost independently of doping, as long as $x < 20\%$. Further increase of doping eventually leads to the destruction of the charge ordered phase, and the system becomes a uniform metal. Upon increasing the local interaction strength U, the critical value of nearest neighbor interaction V increases due to the competition between local and non-local interactions, but the phase boundary remains near $x \sim 20\%$ and a slight backbending is visible for larger U, indicating that the regime of doping shrinks as V is further increased. Numerical difficulties with the impurity solver currently make regimes of larger non-local interaction strength inaccessible.

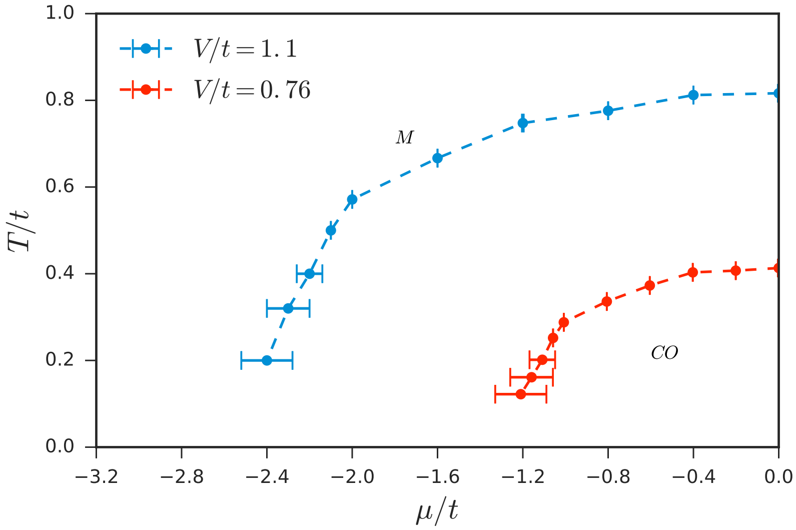

Figure 4.4: Phase boundaries for $V/t = 1.1$ (blue line) and $V/t = 0.76$ (red line) in the space of temperature T and chemical potential μ showing charge-ordered (CO) and isotropic metal (M) phases. All data are obtained for cluster size $N_c = 8$ and local interaction strength $U/t = 2.0$.

In order to establish the temperature and doping parameter space for the charge order phase, which corresponds to the phase diagram typically measured in experiments, [159] we now explore the temperature dependence of the charge order regime shown in Figs. 4.4 and 4.5, as a function of chemical potential μ and doping x. The data are obtained for two representative nearest-neighbor interaction strengths $V/t = 0.76$ and $V/t = 1.1$, which correspond to CO metal and HF-COI, respectively. At high temperature, the system is in a metallic state (M), at low temperature in a charge ordered state (CO). For doping up to 10%, the charge order onset temperature is almost independent of doping. As doping is gradually increased beyond 15%, the onset temperature is rapidly suppressed and, within the parameter range we could reliably study, no charge order is found beyond around 20% doping.

In analogy to the data shown in Figs. 4.2 and 4.3, the data in Fig. 4.6 shows the phase boundary between charge order and metallic states as a function of non-local interaction V and chemical potential μ. To highlight the temperature dependence, we also show data at a temperature that is twice as large. As in Fig. 4.4, the regime supporting charge order shrinks substantially as temperature is raised and thermal fluctuations suppress charge order. In addition, the 'reentrant' backbending behavior as a function of V is only visible at low temperature.

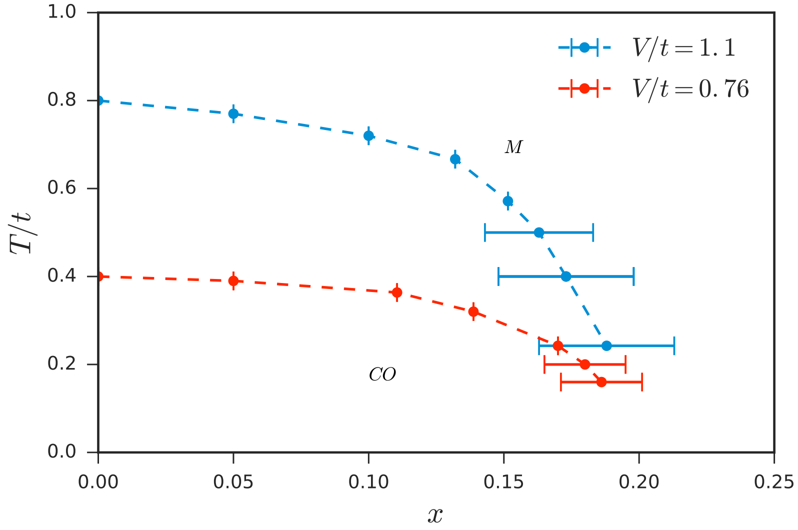

Figure 4.5: Phase boundaries for $V/t = 1.1$ (blue line) and $V/t = 0.76$ (red line) in the space of temperature T and doping x showing charge-ordered (CO) and isotropic metal (M) phases, for $U/t = 2.0$. All data are obtained for cluster size $N_c = 8$.

4.4.2 Order Parameter

The phase boundaries of Figs. 4.2 through 4.6 were obtained by analyzing the site-dependent density as a function of external parameters such as μ or V. In particular, the difference in densities between the two sublattices, $|n_a - n_B|$, is a natural order parameter for the charge ordered phase. A typical example is given in Fig. 4.7, where the densities in sublattice A and B, n_A and n_B, are plotted as a function of chemical potential, for on-site interaction strength $U/t = 2$ and four different non-local interaction strengths. As the chemical potential is raised towards half filling, a spontaneous symmetry breaking of the sublattice densities is visible, indicating the establishment of charge order. As mentioned previously, no first-order hysteresis could be found in our simulations, indicating that all transitions are continuous. Larger nearest-neighbor interactions lead to an earlier onset of the charge order and correspondingly a larger polarization of the density.

The order parameter for charge order, $\delta n = n_A - n_B$, is shown in the left panel of Fig. 4.8, and the total density $n_{\text{ave}} = \frac{1}{2}(n_A + n_B)$ in the right panel of Fig. 4.8. In the uniform phase, $\delta n = 0$, whereas $\delta n \neq 0$ in the charge order phase. The data are shown as a function of chemical potential μ and for a range of non-local interactions V, at constant on-site interaction $U/t = 2$ and temperature $T/t = 0.32$. These data are obtained directly from the sublattice densities shown in Fig. 4.7.

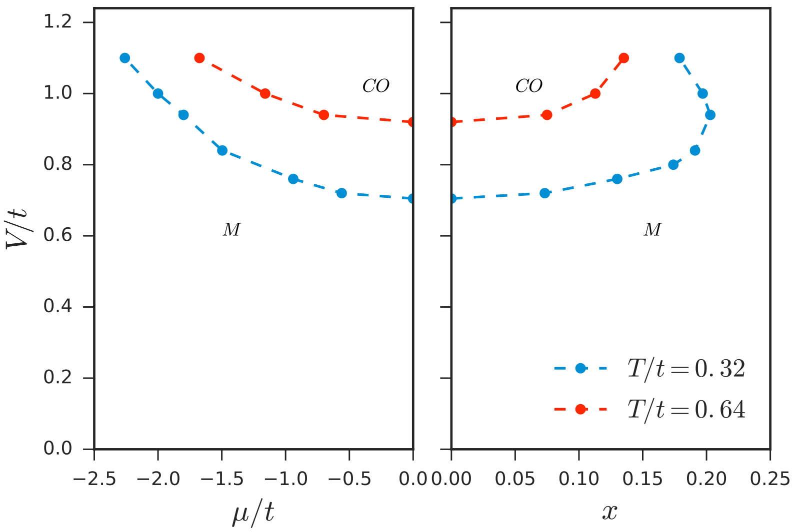

Figure 4.6: Phase boundaries for $T/t = 0.64$ (blue line) and $T/t = 0.32$ (red line) in the space of nearest-neighbor interaction V and chemical potential μ (left panel) / doping x (right panel) showing charge-ordered (CO) and isotropic metal (M) phases. All data are obtained for clusters of size $N_c = 8$ and local interaction strength $U/t = 2$.

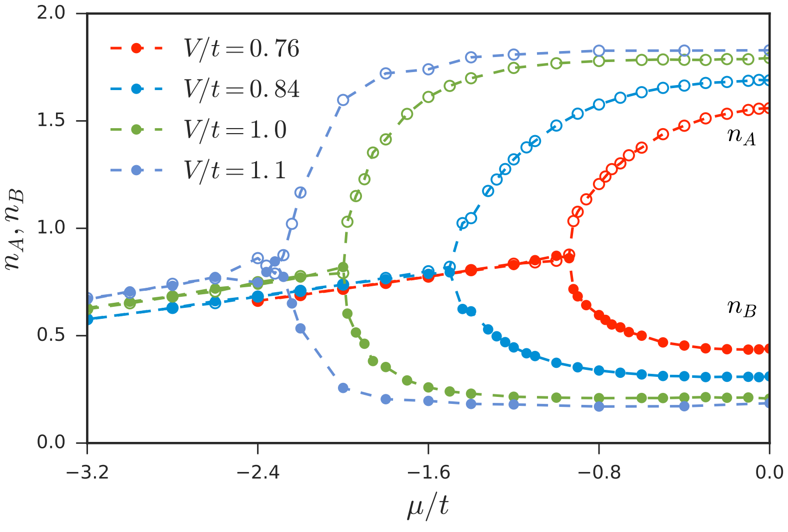

Figure 4.7: Sublattice densities n_A and n_B as a function of chemical potential μ, showing spontaneous establishment of charge-order symmetry breaking, for $U/t = 2.0$, $Nc = 8$, temperature $T/t = 0.32$, and nearest-neighbor interaction strengths V indicated.

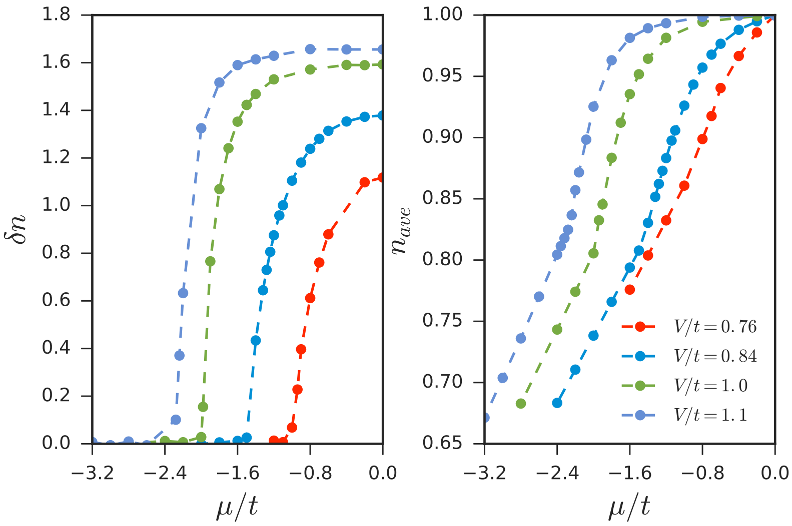

Figure 4.8: (Left) Order parameter $\delta n = n_A - n_B$ and (Right) the average total density $n_{ave} = \frac{n_A + n_B}{2}$ as function of chemical potential μ for $V/t = 0.76, 0.84, 1,$ and 1.1, at temperature $T/t = 0.32$, $U/t = 2$, and on clusters of size $N_c = 8$.

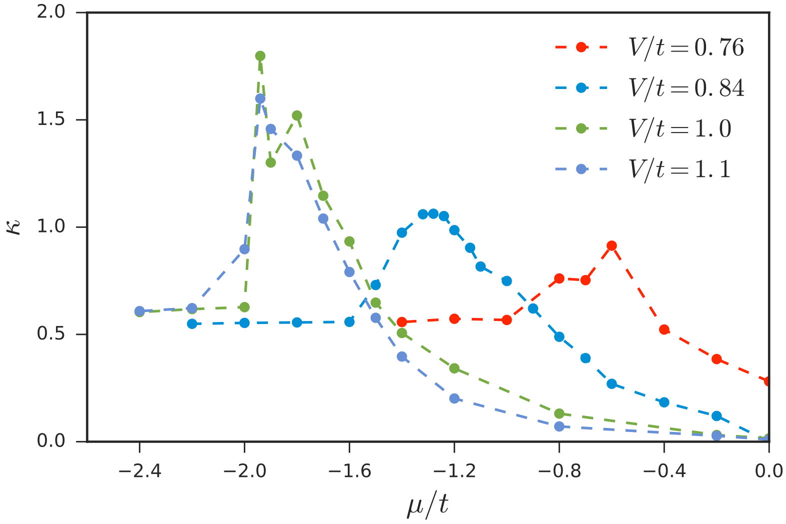

Figure 4.9: Compressibility $\kappa = \frac{\partial n_{ave}}{\partial \mu}$ as a function of chemical potential μ for nearest neighbor strengths indicated. Data obtained for $U/t = 2.0$ on a cluster with $N_c = 8$ and at temperature $T/t = 0.32$.

The total density n_{ave}, shown in the right panel of Fig. 4.8, shows a clear deviation from the linear slope at the position where charge order is established ($\delta n \neq 0$). In addition, for larger inter-site interaction strength, $V/t = 1.0$ and $V/t = 1.1$, a pinning of the n_{ave} vs μ curve to half filling with $n_{ave} = 1$ is visible, indicating an incompressible band insulator-like state (with a robust gap in the density of states) near half filling. As the non-local interaction strength V is increased, the slope of the $n_{ave}(\mu)$ curve rapidly increases on the the ordered side in the vicinity of the phase transition, indicating that first-order coexistence between CO and uniform metallic state may be possible at even larger V.

The HF-COI phase boundary of Fig. 4.2 (red line) was determined by setting a cutoff value of $n \geq 0.995$. As we will show in Sec. 4.4.3, this criterion based on the density also coincides with the region in which the system has a large insulating gap.

The increase of the slope of the $n_{ave}(\mu)$ curve in Fig. 4.8 and, consequently, the narrowing of the region between the charge ordered insulator ($n_{ave} = 1$) and isotropic metal ($\delta n = 0$) is directly responsible for the reentrant behavior observed in Figs. 4.3 and 4.5.

The compressibility $\kappa = \frac{\partial n_{ave}}{\partial \mu}$, Fig. 4.9, here obtained via numerical derivative of the $n_{ave}(\mu)$ curve, shows that the compressibility exhibits a clear maximum at the charge order onset. This maximum becomes more pronounced as V is increased. The value of κ quickly approaches a roughly constant large-μ value on the uniform side of the transition. Consistent with expectation, the half-filled charge ordered insulating state shows a strongly suppressed compressibility.

4.4.3 Spectral functions

Analytically continued local spectral functions, Fig. 4.11, give further insight into the evolution of the charge order transition as a function of doping. For clarity, we limit ourselves to a single scan in doping, using fixed values of $U/t = 2.0$, $V/t = 1.1$, and $T/t = 0.32$. This is the data corresponding to Fig.4.7.

At large doping (not shown), the system is an isotropic Fermi liquid with a small self-energy near zero, so that no suppression of the density of states near zero is visible. As x is lowered from the uniform side towards the onset of charge order (purple panel, $x = 0.196$), the density of states develops a clear suppression near zero indicative of strong charge order fluctuations. However, a symmetry breaking is not yet visible. Reduction of x to 0.143 (light blue panel) and 0.075 (orange panel)

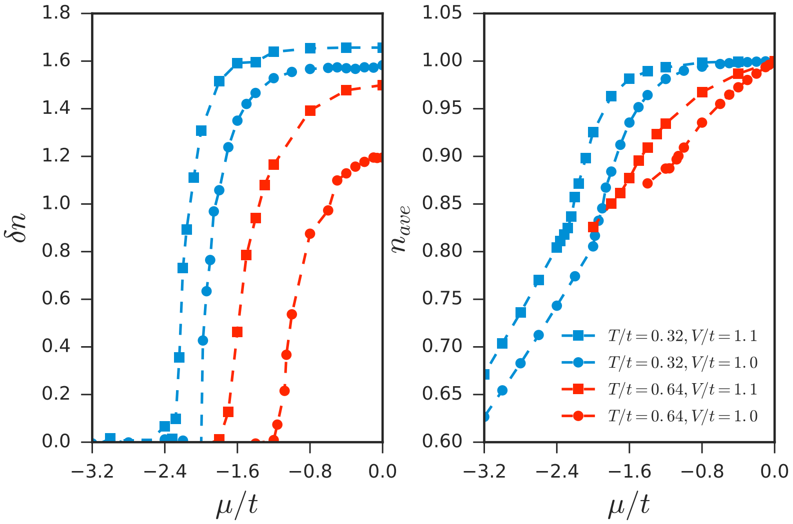

Figure 4.10: Order parameter δn (left panel) and total average density n_{av} (right panel) at temperature $T/t = 0.32$ (blue curves) and $T/t = 0.64$ (red curves) for $U/t = 2$, $N_c = 8$, and for interactions $V/t = 1.1$ (squares) and $V/t = 1.0$ (circles) respectively.

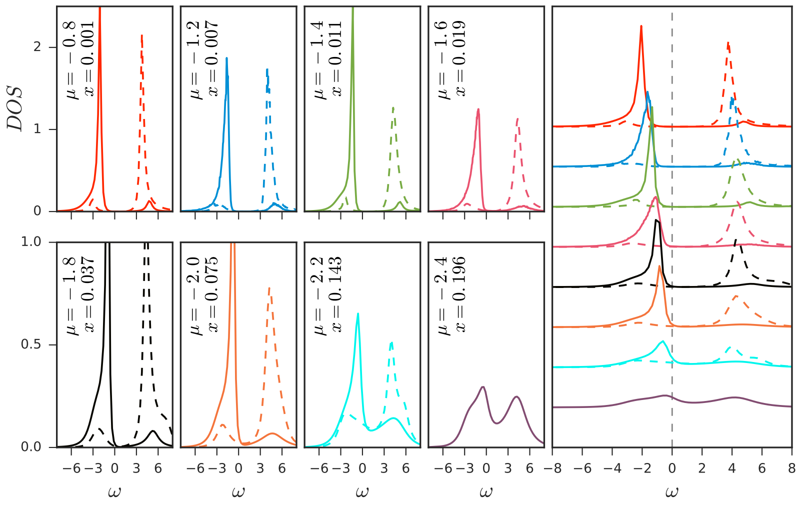

Figure 4.11: Density of states (DOS) for a set of chemical potentials from $\mu/t = -0.8$ to $\mu/t = -2.4$, as a function of frequency. Full lines: sublattice A. Dashed lines: sublattice B. Values are obtained for $T/t = 0.32$, $V/t = 1.1$, and $U/t = 2.0$. For corresponding densities see Fig. 4.8, for compressibilities see Fig. 4.9.

shows the establishment of symmetry breaking but a finite density of states remains at the Fermi energy, indicating a charge order metal. This region coincides with the region of large compressibility visible in Fig. 4.9. As doping is further reduced, the peak-to-peak distance of the minority and majority occupancy spectral functions (full and dashed line) gradually widens and a full gap is established by $x = 0.037$. At this point, further doping transfers spectral weight from below the gap to above the gap, while the lower gap edge stays pinned to the Fermi energy and a large density of states is present just below of the Fermi energy. Finally, as x reaches values near zero, the Fermi energy detaches from the gap edge and moves towards the middle of the gap (at $x = 0$, not shown), while the minority and majority bands become fully particle-hole symmetric.

The results in Fig. 4.11 are obtained via analytic continuation from noisy quantum Monte Carlo results. In this instance, we used a Padé continuation method, which we crosschecked against an implementation of the stochastic analytic continuation method. [160] While analytic continuation does not capture subtle features of the spectral functions, it is generally reliable for the global features (existence of a gap or of the first major peak, weight integrated over a large area, etc) interpreted in the paragraph above.

4.4.4 Energetics

Fig. 4.12 presents an analysis of the energetics of the charge order transition as a function of chemical potential. The top left panel shows the total energy E_{tot} for the four non-local interaction strengths V indicated and for $U/t = 2.0$, $T/t = 0.32$. Also shown, as dashed line, is the isotropic (NC) state where charge order has been artificially suppressed. The phase transition is visible in the top left panel as a slight change of slope and as a deviation between the symmetry broken and the isotropic state.

The total energy consists of two parts, a single-particle 'kinetic' part $\frac{1}{N_c}\sum_K(\epsilon_K - \mu)n_K$ (note that different practitioners use different definitions of the 'kinetic' energy) and an interacting part consisting of the contributions from local and non-local interaction terms. The top right panel shows the doping evolution of the kinetic part. The phase transition is clearly visible in the data, indicating that the large kinetic energy term at low doping is rapidly reduced upon entering the ordered phase. This indicates the reduction of the mobility of electrons once the charge order is established. Nevertheless, the contribution of this term to the total energy is small in comparison to the interaction contribution.

The bottom two panels disentangle the interaction contributions to the total energy. The bottom left panel shows contributions from the local interaction U, while the bottom right panel shows contributions from the non-local interaction V. Note the overall magnitude of the change in comparison to the kinetic part. We first focus on the local interaction energy contribution H_U. The charge order insulator has a high double occupancy at half filling, and therefore a large contribution of the local interaction energy. As the charge order is melted by doping, the double occupancy is rapidly reduced and therefore the local interaction energy contribution is reduced. This behavior of the energetics is opposite from what would be expected in a Mott insulator, where the double occupancy is generally rapidly suppressed upon entering the insulating state, but qualitatively similar to what is expected at an antiferromagnetic transition.

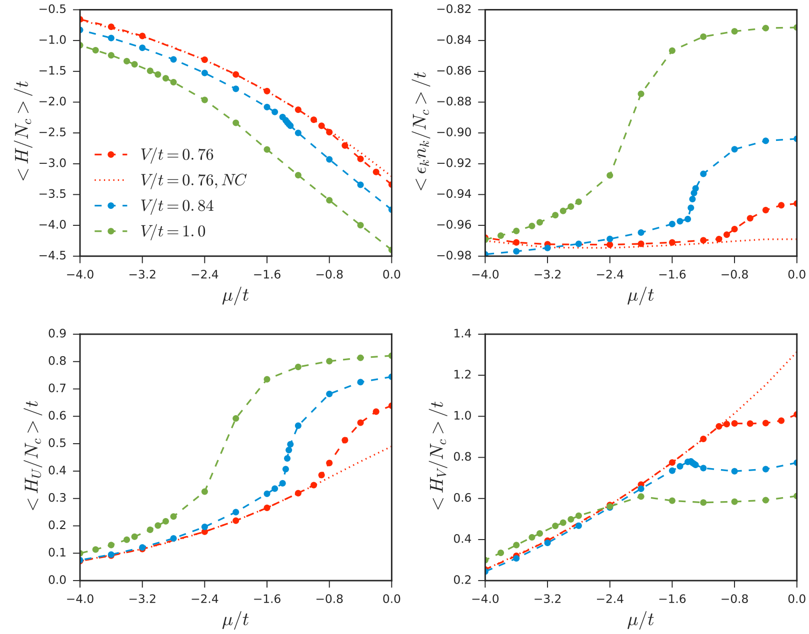

Figure 4.12: Energetics. Top left panel: total energy per particle. Top right panel: kinetic/single particle energy. Bottom left panel: on-site contribution to the potential energy. Bottom right panel: Non-local contribution to the potential energy. Dotted red lines for $V/t = 0.76$ denote the metastable (NC) solution where charge order is suppressed. Error bars, where indicated, denote errors larger than the symbol size.

In contrast, when compared to the uniform phase, the non-local interaction energy H_V in the charge ordered phase is strongly suppressed in the ordered phase by the cost of increase of local interaction H_U due to the increased double occupancy at a given site. Therefore, the charge-order transition mainly reduces the non-local interaction energy at the cost of increasing the local interaction energy, while the

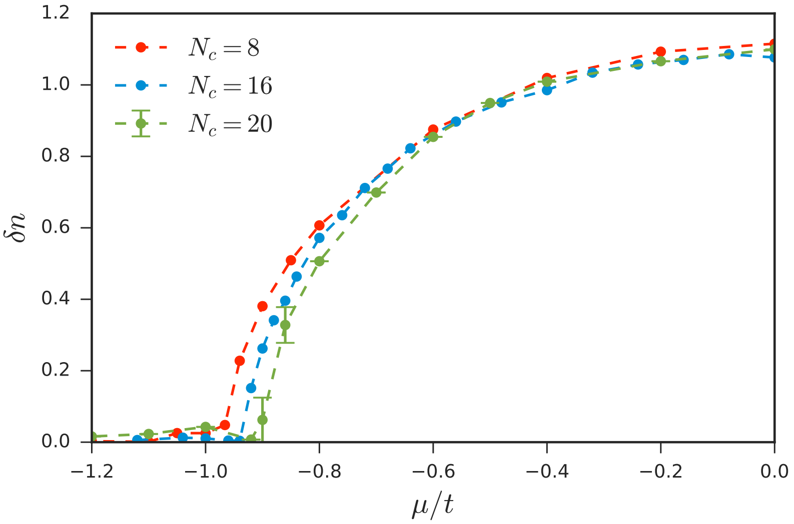

Figure 4.13: Size of the order parameter as a function of doping as cluster size is varied from $N_c = 8$ to $N_c = 16$ and $N_c = 20$, with $V/t = 0.76$, $U/t = 2$, $T/t = 0.32$. For these parameters, a variation in the critical doping of around 5% is visible. Away from the critical point, the order parameter quickly converges with system size.

total change to the kinetic energy is much smaller. [23]

4.4.5 Estimation of finite size effects

The dynamical cluster approximation is controlled, in the sense that $1/N_c$ is a small parameter. Away from criticality, local observables such as the order parameter or the total energy per particle are expected to converge $\sim 1/N_c$. At criticality, where the correlation length is expected to be much larger than the system size, convergence is expected to be slow. Within our approximation, we cannot perform a rigorous finite size scaling at the critical temperature. However, from a limited range of relatively small cluster sizes we can estimate the variation of the critical region with cluster size and illustrate the variance of quantities such as the energy or the order parameter. Fig. 4.13 shows such a study for the order parameter and the critical temperature on clusters of size 8, 16, and 20. Visible are deviations on the order of 5% in the location of the critical doping. The size of the order parameter obtained on the larger clusters quickly converges to the value obtained for $N_c = 8$. A rigorous finite size extrapolation, as it is done in the context of high-temperature cold atom calculations, is not possible for these parameters with current techniques.

4.5 Competition between AFM and CO

The following section closely follows Paki, Terletska, Iskakov, and Gull, "Charge Order and Antiferromagnetic Competition in the 2D Extended Hubbard Model" [95]. Here we consider the competition between charge order and antiferromagnetism by allowing symmetry breaking for both charge and spin.

4.5.1 Green's Functions

The ordered phases investigated here reduce the translation symmetry of the lattice.[14] This doubles the size of the unit cell in real space while halving the size of the Brillouin zone, such that in the ordered phase the momentum space points k and $k+q$ become degenerate, where for AFM and CO $q = (\pi, \pi)$. In order to study ordered and non-ordered phases with the same method, a double cell formalism is used in which momentum space Green's functions on a block diagonal structure. Each bock takes on the following form.

$$G_\sigma(\mathbf{k}) = \begin{pmatrix} G_\sigma(k,k) & G_\sigma(k,k+q) \\ G_\sigma(k+q,k) & G_\sigma(k+q,k+q) \end{pmatrix} \tag{4.3}$$

In the non-ordered phase $G_\sigma(k,k+q) = G_\sigma(k+q,k) = 0$, so that the Green's functions become diagonal in momentum space. In the ordered phases these off diagonal components become finite and obey certain symmetry relations. For AFM, $G_\sigma(k,k+q) = G_\sigma(k+q,k) = -G^*_{-\sigma}(k,k+q) = -G^*_{-\sigma}(k+q,k)$, while for CO we have $G_\sigma(k,k+q) = G_\sigma(k+q,k) = G_{-\sigma}(k,k+q) = G_{-\sigma}(k+q,k)$.

We can define both the momentum dependent and local sublattice and spin resolved Green's functions as follows [23].

$$G_{A/B,\sigma}(k) = \frac{G_\sigma(k,k) + G_\sigma(k+q,k+q)}{2} \pm G_\sigma(k,k+q) \tag{4.4}$$

$$G^{loc}_{A/B,\sigma} = \frac{1}{N_C}\sum_k G_{A/B,\sigma}(k) \tag{4.5}$$

Similar equations describe the sublattice resolved self-energies. These quantities allow us to study how the density of states (from analytic continuation of $G^{loc}_{A/B,\sigma}$) and self-energies behave on each sublattice.

4.5.2 Order Parameter

The order parameters for charge order, Δ_{CO}, and anti-ferromagnetism, Δ_{AFM}, can be computed from the spin resolved cluster site densities, $n_{i\sigma}$.

$$\Delta_{CO} = \frac{2}{N_c} \left| \sum_{i \in A,\sigma} n_{i\sigma} - \sum_{i \in B,\sigma} n_{i\sigma} \right| \tag{4.6}$$

$$\Delta_{AFM} = \frac{1}{N_c} \left| \sum_{i} e^{iQr_i} (n_{i\uparrow} - n_{i\downarrow}) \right| \tag{4.7}$$

For completeness, we note that these expression can also be written in terms of the off diagonal components of the momentum space Green's function in imaginary time, $G_{k,k+q,\sigma}(\tau)$.

$$\Delta_{CO} = \frac{2}{N_c} \left| \sum_{k\sigma} G_\sigma(k, k+Q; \tau = 0^-) \right| \tag{4.8}$$

$$\Delta_{AFM} = \frac{1}{N_c} \left| \sum_{k} \big(G_\uparrow(k, k+Q; \tau = 0^-) - G_\downarrow(k, k+Q; \tau = 0^-) \big) \right| \tag{4.9}$$

4.5.3 AFM vs CO Results

We begin the discussion of our results with the dependence of phase boundaries, order parameters, and energetics on U, V, and β for the half-filled extended Hubbard model. We focus on three phase boundaries exhibited by the model in our approximation: those between the normal and antiferromagnetic phases (Normal-AFM), normal and charge ordered phases (Normal-CO), and antiferromagnetic and charge ordered phases (AFM-CO). In section 4.5.4, we present the TV phase diagram (at $U = 4t$) for the model and examine how order parameters and energtics behave along cuts through the different phase boundaries. We also demonstrate hysteresis across the AFM-CO phase boundary, indicating a first order transition. In section 4.5.5, we present the temperature dependence of the VU phase diagram, comparing $T/t = 1/6$ and $T/t = 1/10$.

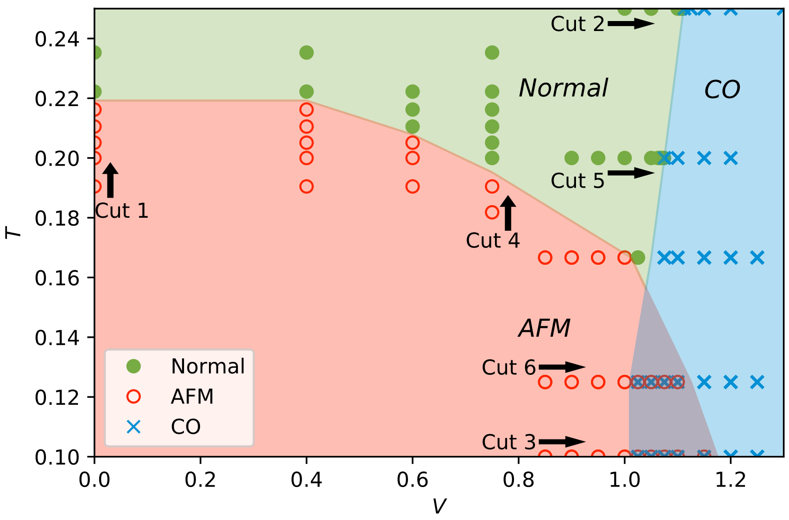

Figure 4.14: TV DCA Phase diagram for the half-filled extended Hubbard model at $U = 4$. Green shading and filled circles: Normal (disordered) state. Red area and open circles: AFM ordering. Blue area and crosses: CO state. Region with both crosses and circles: first order CO/AFM coexistence. Symbols denote simulation points. Transition lines are obtained from the midpoint between simulation points. Also indicated are six phase transition cuts referred to in the text.

4.5.4 T-V phase diagram

The phase diagram as a function of nearest neighbor interaction V and temperature T at fixed $U/t = 4$ is shown in Fig. 4.14. The model exhibits a paramagnetic metallic phase (from now on referred to as the normal state) at high temperature and weak V (green shading in Fig. 4.14), an anti-ferromagnetic state (AFM) at low temperature and low V, and a charge ordered state at large V (blue shading). Symbols indicate simulation points; the phase transition boundaries are obtained from the midpoint between simulation results in different phases.

As is expected from Hubbard model simulations in the absence of V, strong antiferromagnetic correlations exist at half filling. In cluster DMFT simulations, these cause the system to polarize and fall into a long-range antiferromagnetically ordered phase [161, 162] below a transition temperature of $T \sim 2.22$. This 'phase' is an artifact of the approximation and should be understood as an area where long-ranged antiferromagnetic fluctuations are strong.

Larger DCA clusters will eventually lead to a suppression of AFM order in 2d and simply exhibit strong AFM fluctuations [162]. The AFM correlation length is large compared to accessible cluster sizes (and rapidly growing as temperature is

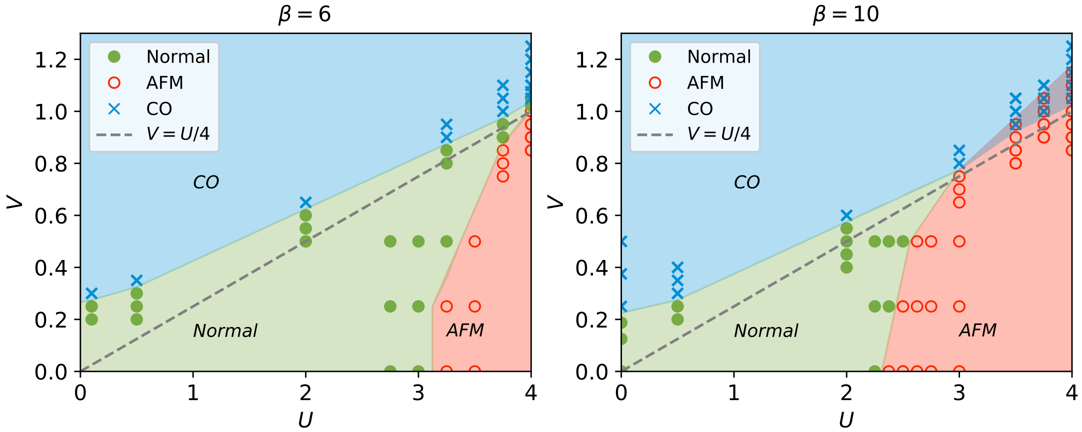

Figure 4.15: Comparison of the UV phase diagram of the extended Hubbard model at $\beta = 6$ and $\beta = 10$, both at $\mu = 0$. At low temperature for this range of U, the AFM and CO phases are entirely separated by the normal state region. Upon lowering the temperature, a hysteresis region emerges at larger U in which both the CO and AFM solutions are stable. Points with both a blue cross and a red, open circle indicates points at which a simulation converges to either a CO or AFM solution, depending on whether a CO or AFM starting solution is used. The mean field result for the phase boundary between the normal and CO state, $V = U/4$, is also shown for comparison.

decreased), making observing a true paramagnetic state difficult within this approximation [162]. However, one may expect that effects present in real systems but excluded from the Hubbard model, such as inter-layer couplings, may stabilize these fluctuations and lead to an actual phase transition with similar overall behavior.

Nonlocal interactions suppress these fluctuations. In this simulation, as V is increased above $\sim 0.6t$, the critical temperature of the artificial antiferromagnetic phase is rapidly reduced. Within DCA, further increase of V will entirely suppress the antiferromagnetic state, so that beyond a value of $\sim 1.2t$ no AFM ordering is observed in our calculations.

Repulsive non-local interactions on a bipartite lattice eventually lead to a charge ordered state [23]. For our parameters, at $U/t = 4$, this charge ordering sets in at $V/t \sim 1.1$ for the highest T shown. Lowering the temperature shifts that phase boundary towards lower values of U, such that at $T/t = 0.1$ the phase boundary is observed near $V/t = 1.0$.

For the parameter values chosen, there is an area where both charge ordered and antiferromagnetic states can occur. In this area, the nearest neighbor interaction is large enough that charge order is favorable, but the temperature is low enough that

AFM fluctuations are strong. In our simulation, we find a first-order coexistence regime where the system is either in a charge ordered state (where magnetic order is absent) or in an AFM state (where charge order is absent).

4.5.5 U-V phase diagram

To illustrate the evolution of the phase diagram as a function of nearest and next-nearest interactions, we present a cut in the V-U plane at constant T in Fig. 4.15. The left panel shows the extent of the three phases at the higher temperature, $T/t = 1/6$. At large V, the system is charge ordered at half filling (blue area). At small V but large U, the system undergoes an antiferromagnetic transition in this approximation (red area). And at small U and V, the model is in an isotropic 'normal' state (green). The right panel repeats this presentation for the lower temperature $T/t = 1/10$.

As explored in previous work [23, 94] (see also results from other methods [163, 155, 164, 20]), the CO transition sits above the mean field line [22], has a non-zero intersect at $U = 0$, and is only weakly temperature dependent. In contrast, the AFM phase in this approximation is very strongly temperature dependent for these parameters, hinting at a rapid evolution of the spin susceptibility in this model, and moves to substantially lower U and larger V as the temperature is lowered.

At the lower temperature, the coexistence between the two phases occurs at large V and large U, where the non-local interaction is strong enough to favor charge order but the local U also permits longer range antiferromagnetism.

The phase diagram as a function of nearest neighbor interaction V and on-site interaction U at half-filling for $T = 1/6$ and $T = 1/10$ is shown in Fig. 4.15. The symbols and shading carry the same relation to the Normal, AFM, and CO states as in Fig. 4.14.

At both temperatures shown in Fig. 4.15, charge order is favored at large V and antiferromagnetism is favored at large U. When the temperature is decreased from $T = 1/6$ to $T = 1/10$, the charge order region expands slightly (i.e. the transition occurs at a slightly lower V for a given U), whereas the AFM region expands significantly (i.e. the transition occurs for a much smaller U for a given V).

4.5.6 Order parameter and phase boundaries

Charge order is characterized by a difference between the occupancies on different sublattices, as described by the order parameter in Eq. 4.6. Antiferromagnetism, as

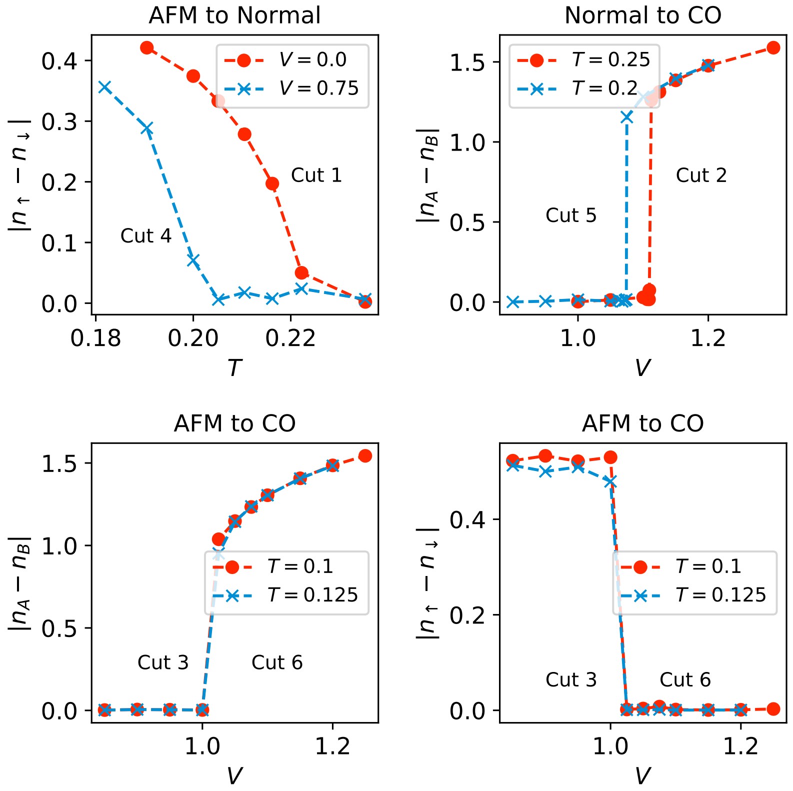

Figure 4.16: AFM and CO order parameters across phase transition. $U/t = 4$, $\mu = 0$. AFM-Normal at constant V (top left panel), CO-Normal at constant T (top right panel), and AFM-CO (bottom panels). AFM-CO cuts are obtained with a CO starting solution; see Fig. 4.18 for hysteresis.

defined by the order parameter of Eq. 4.7, is identified by different occupancies of the two spin species. In order to distinguish between ordered and isotropic points in the presence of Monte Carlo noise, we define simulation points with order parameters larger than 0.1 as ordered in Figs. 4.14 and 4.15.

Raw data for the order parameters along the cuts indicated in Fig. 4.14 are shown in Fig. 4.16. The top left panel shows the order parameters across the antiferromagnetic phase boundary. Shown are two cuts at constant V but for varying temperature. The continuous increase in the order parameter indicates a second order phase transition. Larger non-local interaction moves the onset of the phase transition to lower temperatures, suppressing both the onset and the strength of the antiferromagnetic order parameter.

The top right panel shows the transition from the normal state to charge order, at constant temperature, as a function of V. In the absence of long-ranged antifer-

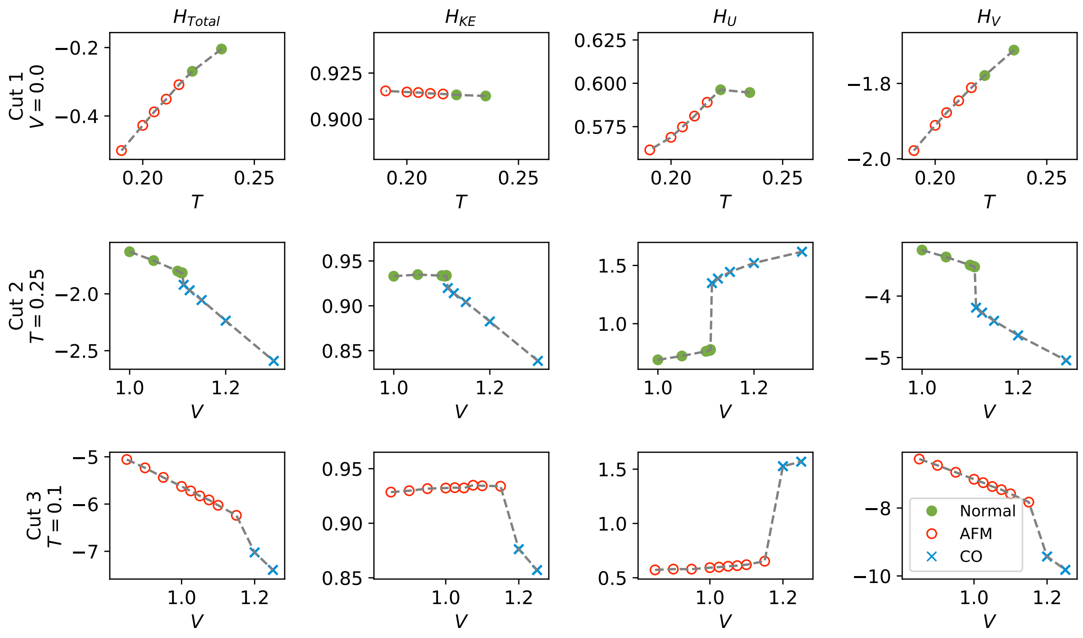

Figure 4.17: Contribution to the energetics across three phase transitions for the extended Hubbard model at $U = 4$, $\mu = 0$. Top Row: AFM-Normal transition along Cut 1 from Fig. 4.14. As AFM order emerges, the on site interaction energy, H_U is suppressed by the reduction in double occupancy. Middle Row: Normal-CO transition along Cut 2 from Fig. 4.14. The localization of electrons on the one sublattice leads to a decrease in the kinetic energy, H_{KE}, an increase in the on-site interaction energy, H_U, in exchange for a decrease in the nearest neighbor interaction energy, H_V. Bottom Row: AFM-CO transition along cut 3 from Fig. 4.14, showing only the results obtained from the AFM starting solution. An increase in the on-site interaction energy, H_U is exchanged for a decrease in the nearest neighbor interaction energy, H_V. The symbols for each data point, indicating the stable phase, follow from Fig. 4.14.

romagnetic order, this transition has been analyzed in detail in previous work [23]. As discussed later on in (Sec. 4.5.8), this transition is also first order at these interactions strengths and temperatures. Lower temperatures lead to an earlier onset of the charge ordered state at lower V [23, 20].

The bottom two panels show the order parameter across the transition from the antiferromagnetic (low V) to the charge ordered (large V) states, at constant T as a function of V. Shown are both the magnetic (left) and charge ordered (right) order parameters. This transition is first order (see Sec. 4.5.8 for hysteresis); shown here are data obtained by starting from a charge ordered solution.

4.5.7 Energetics

Fig. 4.17 shows the contributions to the energetics as the system crosses the phase boundaries. Shown are the total energy H_{Total}, the kinetic energy H_{KE}, the contribution of the local energy to the interaction energy H_U, and the contribution of the non-local term to the interaction energy H_V. These energies are computed as

$$H_{KE} = \frac{1}{N_C} \sum_{k\sigma} (\epsilon_k - \mu) \langle n_{k\sigma} \rangle \tag{4.10}$$

$$H_V = \frac{K - \langle k \rangle}{\beta N_C} - H_U \tag{4.11}$$

$$H_U = \frac{U}{N_C} \sum_i \langle n_{i\uparrow} n_{i\downarrow} \rangle, \tag{4.12}$$

and $H_{Total} = H_{KE} + H_U + H_V$. $\langle k \rangle$ denotes the average order sampled during the Monte Carlo simulation [165] and K is a constant introduced in the CT-AUX algorithm by a Hubbard-Stratonovich transformation [152].

The first row of Fig. 4.17 shows how the different energy components change as the temperature is increased and the system moves from an AFM ordered phase to the normal state. The dominant change upon entering the AFM phase is a reduction of the on-site interaction, H_U, due to the suppression of the double occupancy. Kinetic energies and potential energies show little change. This is consistent with the antiferromagnetic transition in single site DMFT and four-site cluster DMFT below the Mott transition, where the opening of the antiferromagnetic gap lowers the energy by suppressing the double occupancy [166].

The second row shows the energetics as V is increased and the system enters the charge ordered state from the normal state at high temperature. Here, the major change in the energetics is the non-local interaction energy term H_V, which can be dramatically lowered by entering a charge ordered phase. The kinetic energy decreases slightly as electrons become constrained to one sublattice, and the transition is accompanied by an increase in the on-site interaction energy, H_U, caused by the increase of the double occupancy in the charge ordered state. We note that although the change in energy looks sharp at this resolution, we found no evidence of coexistence across this transition.

Finally, the third row displays the evolution of the system as it jumps between the AFM and CO phases at low temperature. This transition is first order. The data shown is from the branch of the hysteresis that starts in the AFM phase. It is evident that the transition requires a substantial rearrangement of the energetics, with major changes in all energy terms.

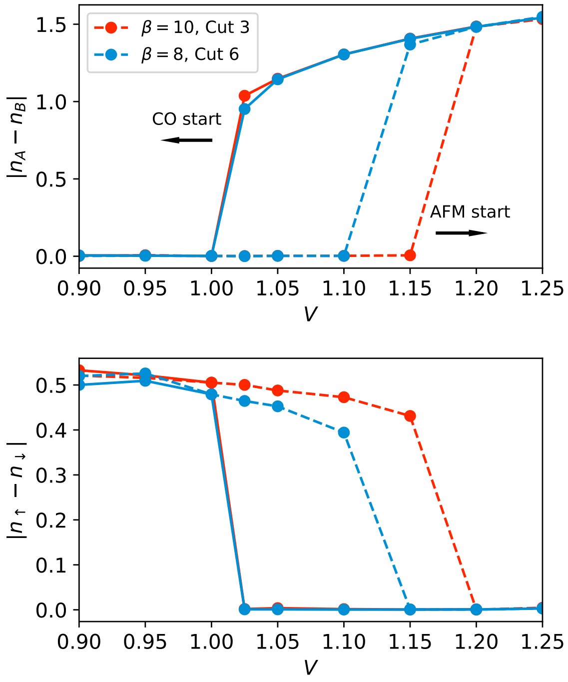

Figure 4.18: Hysteresis between AFM and CO. $U = 4t$, half filling, $\beta t = 10$ (red) and $\beta t = 8$ (blue). Top panel: CO order parameter, Δ_{CO}. Bottom panel: AFM order parameter, Δ_{AFM}. Dashed (solid) lines indicate convergence from a charge ordered (an antiferromagnetic) initial guess.

4.5.8 Hysteresis

We present evidence of hysteresis in the AFM/CO transition at low temperatures in Fig. 4.18. This data is obtained by running each simulation point twice - once with an initial configuration corresponding to an AFM ordered state, and once with one describing a charge ordered state. Outside the coexistence region both of these simulations converge to the same solution. In contrast, in a coexistence region both states will be stable and the two simulations will converge to different solutions.

The top panel of Fig. 4.18 shows the CO order parameter, while the bottom panel shows the AFM order parameter. Shown is a trace along Cut3 ($T/t = 1/10$) and Cut6 ($T/t = 1/8$) at constant temperature as a function of V. A coexistence regime

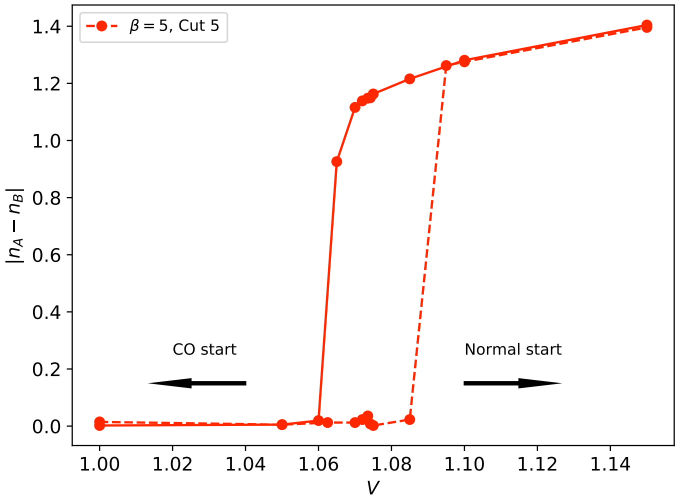

Figure 4.19: Hysteresis between Normal and CO states. $U = 4t$, half filling, $\beta t = 5$. Shown is the converged CO order parameter, Δ_{CO}, arising from simulations started with Normal solution with a small CO offset (dotted) and a CO solution (solid).

starts at $V/t \sim 1$ and extends to $V/t \sim 1.2$ at the lower temperature, and shrinks as temperature increases (demonstrated by the $T/t = 1/8$ data) and eventually vanishes, see Fig. 4.14. The data indicates that the stable states are always only AFM or CO, and that no solutions have both finite AFM and finite CO ordering.

We also show evidence for a small hysteresis region in the Normal/CO transition in Fig. 4.19. The figure shows the converged CO order parameter resulting from two sets of simulations, at $\beta = 5$ and $U = 4$. In the first set, each simulation is started with a Normal state solution with a small CO offset. In the second set, each simulation is started with a CO state solution. For a narrow range of V, from about $V \approx 1.065$ to $V \approx 1.9$, these simulations reveal that both Normal and CO states are stable. This indicates that at this temperature and interaction strength, the Normal to Charge Order phase transition is first order.

This finding is consistent with the sharp transition in energy displayed in Fig. 4.17, as well as previous work [23] that indicated that the Normal to CO transition is continuous at small U but sharpens as U is increased. Since the hysteresis region is so narrow, we do not attempt to draw it on our phase diagrams. All other plots in this paper dealing with the Normal to CO transition display data obtained from simulations that start with a Normal state solution.

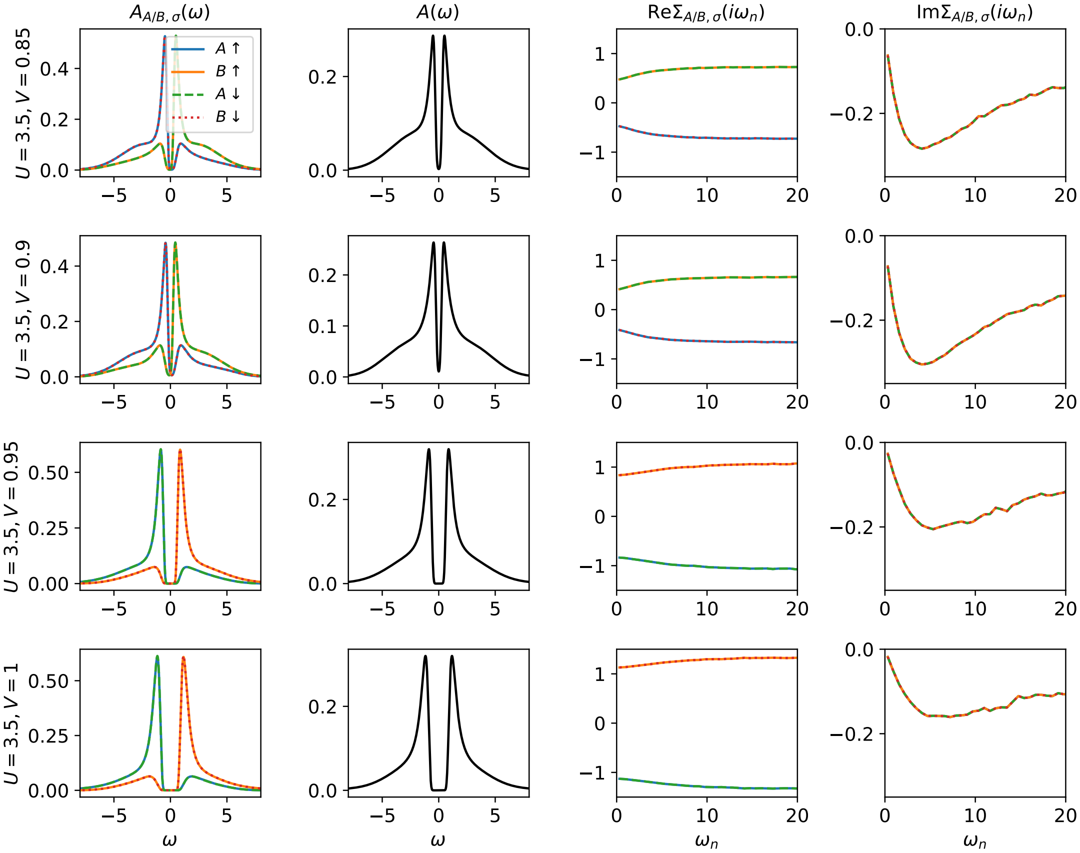

Figure 4.20: Evolution of spectral functions across AFM-CO phase boundary at $U = 3.5t$. First column: spin and sublattice resolved spectral function. Second column: local spectral function depicting the qualitative difference between the small AFM and large CO gap. Third and fourth columns: real and imaginary part of the Matsubara frequency self-energy.

4.5.9 Spectral Functions

Fig. 4.20 shows the evolution of the spectral function and self energy across the AFM/CO phase boundary at $U = 3.5$ and $\beta = 10$. The first column depicts the different sublattice and spin contributions to the total spectral function, which is shown in the second column. The symmetry of the sublattice and spin components change as one would expect in moving from the AFM to CO state. At lower V the occupied states (i.e. states with energy below $\omega = 0$) are predominantly those with spin up on the A sublattice and spin down on the B sublattice. These components are equal to each other and related to the other components (spin down on sublattice A and spin up on sublattice B) by particle-hole symmetry (i.e. $\omega \to -\omega$), as expected for an antiferromagnetic state. Upon increasing V and transitioning into the charge ordered state, the symmetry of the spectral function components change so electrons occupy the A sublattice and vacate the B sublattice, with symmetry between the up and down spin components.

We can use the total spectral function results to compare the energy gaps at $\omega = 0$ on either side of the AFM/CO transition. At lower V, the system is not fully gapped and is in a metallic state with AFM order. In contrast, the charge ordered state displays a gap immediately after the transition.

The last two columns of Fig. 4.20 show how the real and imaginary parts of the sublattice and spin resolved Matsubara self-energies behave through the AFM/CO transition. The real parts switch symmetry and increase in magnitude upon entering the charge ordered state, in agreement with the formation of a robust electronic gap. In contrast, the imaginary part of the self-energy seems to be smaller in the charge order state than the antiferromagnetic state, indicating smaller correlation effects. This behavior makes physical sense because the antiferromagnetic state is dependent upon spin correlations between electrons in the two sublattices (i.e. virtual exchange hopping), whereas the charge ordered state can be viewed as a result of classical energetics that favor a reduction in the double occupancy.

4.6 Submatrix Updates

This section describes some of the technical details of the numerical algorithm used to produce the results for the extended Hubbard model presented earlier in this chapter.

One way to improve the efficiency and stability of the Monte Carlo updates performed during the CT-AUX algorithm is with submatrix updates [25, 98]. Rather than performing each auxiliary spin update individually, with the submatrix scheme we collect k accepted updates and apply their collective effects all at once, as shown in Fig. 4.21. In this section we describe new work to apply to apply the submatrix updates method to the double cell formalism used for studying charge order in the extended Hubbard model. The CT-AUX method used to study charge order was reviewed in Chapter 2.

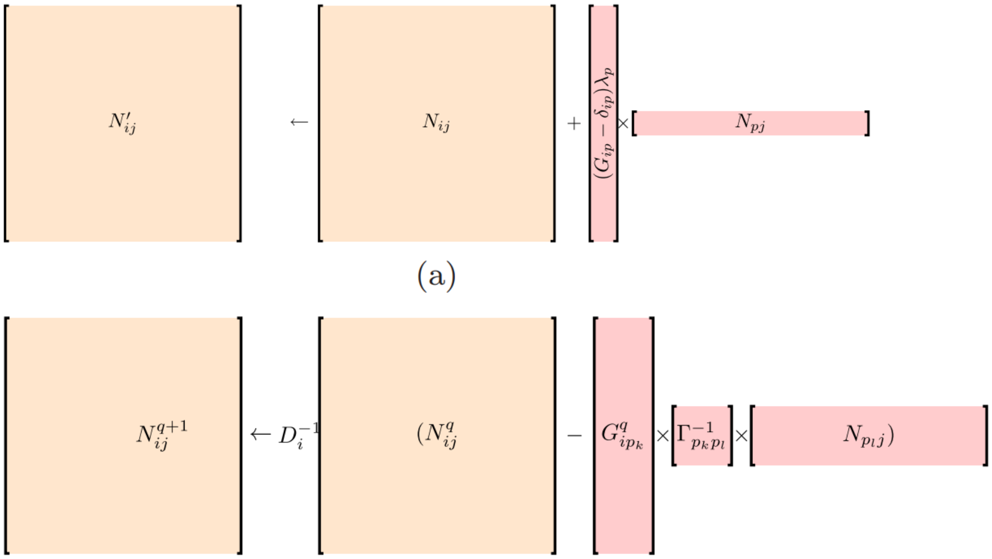

(a)

(b)

Figure 4.21: Illustration of update formulas. 1(a): rank-one updates of Ref.[24], accessing $O(m^2)$ data points for $O(m^2)$ operations and performing one update. 1(b):submatrix updates, accessing $O(m^2)$ values but performing $O(m^2k)$ operations, for k updates. Figure and caption from Ref. [25].

4.6.1 Spinflip Determinant Ratios for Charge Order

The CT-AUX algorithm, when modified for the double cell formalism needed for simulating antiferromagnetic and charge ordered states, [14, 23] yields the following expansion for the partition function.

$$Z = \sum_{k=0}^{\infty} \sum_{s_i=\pm 1} \int_0^{\beta} d\tau_1 ... \int_{\tau_{k-1}}^{\beta} \tau_k \left(\frac{K}{8\beta N_C^2}\right)^k \sum_{i_n j_n \sigma_n \sigma'_n} \det\left[e^{\Gamma^{\sigma\sigma'}_{ij}} - G^{ij}_{0\sigma\sigma'}\left(e^{\Gamma^{\sigma\sigma'}_{ij}} - I\right)\right] \tag{4.13}$$

If we define a new matrix, N, as

$$N^{-1} = \left[e^{\Gamma^{\sigma\sigma'}_{ij}} - G^{ij}_{0\sigma\sigma'}\left(e^{\Gamma^{\sigma\sigma'}_{ij}} - I\right)\right] \tag{4.14}$$

The reason for defining the inverse of N will become clear later. With this definition, our Monte Carlo process will simply sample different values of $\det N^{-1}$, based on the configurations of auxiliary spins assigned to each site, s_i, the imaginary time positions of the auxiliary spins, τ_i, and the lattice and (real) spins of each vertex, $i_n, j_n, \sigma_n, \sigma'_n$. Note that each vertex in our auxiliary spin expansion is related to two sites and two spins because of the non-local term, V, in the extended Hubbard model.

The various terms in the definition of N^{-1} are constructed from the configurations as follows.

$$e^{\Gamma_{ij}^{\sigma\sigma'}} = \begin{pmatrix} \begin{pmatrix} e^{\gamma_{i_1 j_1}^{\sigma_1\sigma'_1} s_1} & 0 \\ 0 & e^{-\gamma_{i_1 j_1}^{\sigma_1\sigma'_1} s_1} \end{pmatrix} & & 0 \\ & \ddots & \\ 0 & & \begin{pmatrix} e^{\gamma_{i_k j_k}^{\sigma_k\sigma'_k} s_k} & 0 \\ 0 & e^{-\gamma_{i_k j_k}^{\sigma_k\sigma'_k} s_k} \end{pmatrix} \end{pmatrix} \tag{4.15}$$

$$G_{0\sigma\sigma'}^{ij} = \begin{pmatrix} \begin{pmatrix} g_{i_1 i_1}^{\sigma_1\sigma_1}(\tau_1-\tau_1) & g_{i_1 j_1}^{\sigma_1\sigma'_1}(\tau_1-\tau_1) \\ g_{j_1 i_1}^{\sigma'_1\sigma_1}(\tau_1-\tau_1) & g_{j_1 j_1}^{\sigma'_1\sigma'_1}(\tau_1-\tau_1) \end{pmatrix} & & \begin{pmatrix} g_{i_1 i_n}^{\sigma_1\sigma_n}(\tau_1-\tau_n) & g_{i_1 j_n}^{\sigma_1\sigma'_n}(\tau_1-\tau_n) \\ g_{j_1 i_n}^{\sigma'_1\sigma_n}(\tau_1-\tau_n) & g_{j_1 j_n}^{\sigma'_1\sigma'_n}(\tau_1-\tau_n) \end{pmatrix} \\ \vdots & \ddots & \vdots \\ \begin{pmatrix} g_{i_n i_1}^{\sigma_n\sigma_1}(\tau_n-\tau_1) & g_{i_n j_1}^{\sigma_n\sigma'_1}(\tau_n-\tau_1) \\ g_{j_n i_1}^{\sigma'_n\sigma_1}(\tau_n-\tau_1) & g_{j_n j_1}^{\sigma'_n\sigma'_1}(\tau_n-\tau_1) \end{pmatrix} & & \begin{pmatrix} g_{i_n i_n}^{\sigma_n\sigma_n}(\tau_n-\tau_n) & g_{i_n j_n}^{\sigma_n\sigma'_n}(\tau_n-\tau_n) \\ g_{j_n i_n}^{\sigma'_n\sigma_n}(\tau_n-\tau_n) & g_{j_n j_n}^{\sigma'_n\sigma'_n}(\tau_n-\tau_n) \end{pmatrix} \end{pmatrix} \tag{4.16}$$

The $\gamma_{ij}^{\sigma\sigma'}$ terms arises from the decoupling transformation, and takes on different values depending on the vertex configuration.

$$\cosh\gamma_{ij}^{\sigma\sigma'} = 1 + \frac{\beta N_C^2}{K} U_{ij}^{\sigma\sigma'} = \begin{cases} 1 + \frac{\beta N_C^2 U}{K}, \ i = j, \sigma = -\sigma' \\ 1 + \frac{\beta N_C^2 V}{K}, \ i \neq j, \sigma = -\sigma' \\ 1 + \frac{\beta N_C^2 V}{K}, \ i \neq j, \sigma = \sigma' \\ 1, \ i = j, \sigma = \sigma' \end{cases} \tag{4.17}$$

The elements of $G_{0\sigma\sigma'}^{ij}$ are Green's functions between the different vertices.

$$g_{i_l j_m}^{\sigma_l \sigma'_m}(\tau_l - \tau_m) = \langle T_\tau c_{i_l\sigma_l}(\tau_l) c_{j_m\sigma'_m}^\dagger(\tau_m)\rangle \delta_{\sigma_l\sigma'_m} \tag{4.18}$$

The delta function here arises because there are no spin flipping terms in our Hamiltonian. This means that any Green's functions involving unequal spins will be zero, and thus that every term appearing in N^{-1} will involve either $\uparrow\uparrow$ or $\downarrow\downarrow$ spin configurations. It can therefore be written as a block diagonal matrix in the spins, which allows us to split up the determinant appearing in the partition function expansion.

$$N^{-1} = \begin{pmatrix} N_{\uparrow}^{-1} & 0 \\ 0 & N_{\downarrow}^{-1} \end{pmatrix} \rightarrow \det N^{-1} = \det N_{\uparrow}^{-1} \det N_{\downarrow}^{-1} \tag{4.19}$$

This is similar to the normal CT-AUX algorithm, but here an important consideration is that the sizes of the matrices $\det N_{\uparrow}^{-1}$ and $\det N_{\downarrow}^{-1}$ can be different.

For example, if the current configuration, v, involves two vertices,

$$v = \{(\sigma_1, \sigma_1', i_1, j_1, s_1, \tau_1), (\sigma_2, \sigma_2', i_2, j_2, s_2, \tau_2)\} \tag{4.20}$$

and we know that $\sigma_1 = \sigma_2 = \sigma_2' \neq \sigma_1'$, and that $\sigma_1' =\uparrow$, then the N matrices are given by the following.

$$N_{\uparrow}^{-1} = \left(e^{-\gamma_1 s_1} - g_{j_1 j_1}^{\sigma_1' \sigma_1'}(e^{-\gamma_1 s_1} - 1)\right) \tag{4.21}$$

$$N_{\downarrow}^{-1} = \begin{pmatrix} e^{\gamma_1 s_1} - g_{i_1 i_1}^{\sigma_1 \sigma_1}(e^{\gamma_1 s_1} - 1) & g_{i_1 i_2}^{\sigma_1 \sigma_2}(e^{\gamma_2 s_2} - 1) & g_{i_1 j_2}^{\sigma_1 \sigma_2'}(e^{-\gamma_2 s_2} - 1) \\ g_{i_2 i_1}^{\sigma_2 \sigma_1}(e^{\gamma_1 s_1} - 1) & e^{\gamma_2 s_2} - g_{i_2 i_2}^{\sigma_2 \sigma_2}(e^{\gamma_2 s_2} - 1) & g_{i_2 j_2}^{\sigma_2 \sigma_2'}(e^{-\gamma_2 s_2} - 1) \\ g_{j_2 i_1}^{\sigma_2' \sigma_1}(e^{\gamma_1 s_1} - 1) & g_{j_2 i_2}^{\sigma_2 \sigma_2'}(e^{\gamma_2 s_2} - 1) & e^{-\gamma_2 s_2} - g_{j_2 j_2}^{\sigma_2' \sigma_2'}(e^{-\gamma_2 s_2} - 1) \end{pmatrix} \tag{4.22}$$

Every time we add/remove/flip a vertex during our simulation, we need to add/remove/flip one column and row to each of $N_{\uparrow}^{-1}$ and $N_{\downarrow}^{-1}$ if $\sigma \neq \sigma'$, or add/remove/flip two columns and rows to N_{σ}^{-1} if $\sigma = \sigma'$.

The fundamental idea behind submatrix updates is to delay updating the N matrices during the Monte Carlo simulation, until some number of accepted updates have been collected and then applying their net affect to N all at once. This scheme allows us to replace vector-matrix multiplications with matrix-matrix multiplications, increasing the computational efficiency and potentially numerical stability. Here we will focus on applying submatrix idea to the spin flip updates.

The first step is to establish how flipping a single auxiliary spin, s_n, changes the N matrices. Let's focus on how this update changes N_{σ}^{-1}. If there are currently k vertices in the configuration,

$$v = \{(\sigma_1, \sigma_1', i_1, j_1, s_1, \tau_1), ..., (\sigma_k, \sigma_k', i_k, j_k, s_k, \tau_k)\}, \tag{4.23}$$

then there is one column and row in $N^{-1}\sigma$ for every σ_n and σ_n' that is equal to σ. Furthermore, if $\sigma_n = \sigma$, then i_n appears in N_σ^{-1}, and if $\sigma_n' = \sigma$, then j_n appears.

Let us define parameters that allow us to map between the indices of N_σ^{-1} and the variables of each vertex. If we define Δ_l to be the number of the vertex corresponding to the row/column l of N_σ^{-1}, S_l to be the $i_{\Delta l}$ or j_{Δ_l} in row/column l, and

$$d_l = \begin{cases} 1, \ S_l \text{ an i site} \\ -1, \ S_l \text{ a j site} \end{cases} \tag{4.24}$$

Then we can define N_σ^{-1} as

$$N_\sigma^{-1} = e^{\Gamma_\sigma} - G_{0\sigma}(e^{\Gamma_\sigma} - I) \tag{4.25}$$

where

$$(G_{0\sigma})_{lk} = g^\sigma_{S_l S_k} \tag{4.26}$$

$$\left(e^{\Gamma_\sigma}\right)_{lk} = \delta_{lk} e^{V(l)} \tag{4.27}$$

$$V(l) = d_l \gamma_{i_{\Delta_l} j_{\Delta_l}}^{\sigma_{\Delta_l} \sigma'_{\Delta_l}} s_{\Delta_l} \tag{4.28}$$

During a spin flip update of auxiliary spin s_n, we need to change all columns l of N_σ^{-1} such that $\Delta_l = n$. This means we will potentially be changing one or two columns, depending on if $\sigma_n = \sigma_n'$. Let's suppose that $\sigma = \sigma_n = \sigma_n'$, in which case we need to update to adjacent columns of N_σ^{-1} as follows.

$$\begin{aligned} (N_\sigma^{-1})'_{ij} &= {N_\sigma^{-1}}_{ij} \\ &- {N_\sigma^{-1}}_{ij} \delta_{lj} - {N_\sigma^{-1}}_{ij} \delta_{l+1,j} \\ &+ \left(e^{\Gamma'_\sigma} - G_{0\sigma}(e^{\Gamma'_\sigma} - I)\right)_{ij} \delta_{lj} + \left(e^{\Gamma'_\sigma} - G_{0\sigma}(e^{\Gamma'_\sigma} - I\right)_{ij} \delta_{l+1,j} \\ &= {N_\sigma^{-1}}_{ij} + \left[(1 - G_{0\sigma}) \left(e^{\Gamma'_\sigma} - e^{\Gamma_\sigma}\right)\right] (\delta_{lj} + \delta_{l+1,j}) \end{aligned} \tag{4.29}$$

Since Γ_σ is a diagonal matrix, we have that

$$\left(e^{\Gamma'_\sigma} - e^{\Gamma_\sigma}\right)_{ij} = \delta_{il}\delta_{jl} \left(e^{V'(l)} - e^{V(l)}\right) + \delta_{i,l+1}\delta_{j,l+1} \left(e^{V'(l+1)} - e^{V(l+1)}\right). \tag{4.30}$$

This allows us to write the updated N_σ^{-1} as

$$\begin{aligned}(N_\sigma^{-1})'_{ij} = (N_\sigma^{-1})_{ij} + (1 - G_{0\sigma})_{il}\left(e^{V'(l)} - e^{V(l)}\right)\delta_{j,l} \\ + (1 - G_{0\sigma})_{i,l+1}\left(e^{V'(l+1)} - e^{V(l+1)}\right)\delta_{j,l+1}\end{aligned} \tag{4.31}$$

In matrix notation, this is equivalent to the following.

$$(N_\sigma^{-1})' = N_\sigma^{-1} + u_1 v_1^T + u_2 v_2^T = N_\sigma^{-1} + u \cdot v \tag{4.32}$$

$$u = \left(\begin{array}{c|c} u_1 & u_2 \end{array} \right) \tag{4.33}$$

$$v = \left(\begin{array}{c} v_1^T \\ \hline v_2^T \end{array} \right) \tag{4.34}$$

Where u_1, u_2, v_1, and v_2 are column vectors defined as,

$$(u_1)_i = (\delta_{il} - G_{0\sigma il})\left(e^{V'(l)} - e^{V(l)}\right) \tag{4.35}$$

$$(u_2)_i = (\delta_{i,l+1} - G_{0\sigma i,l+1})\left(e^{V'(l+1)} - e^{V(l+1)}\right) \tag{4.36}$$

and $(v_1^T)_i = \delta_{il}$, $(v_j^T)_i = \delta_{i,l+1}$.

We will now make use of the Woodberry matrix identity, which states that

$$(A + UCV)^{-1} = A^{-1} - A^{-1}U\left(C^{-1} + VA^{-1}U\right)^{-1}VA^{-1}. \tag{4.37}$$

Applying the Woodberry identity to our equations for how N_σ^{-1} changes under a spin update gives us an expression for how N_σ changes.

$$N'_\sigma = N_\sigma - N_\sigma u\left(I + vN_\sigma u\right)^{-1} vN_\sigma \tag{4.38}$$

Using the Hirsch-Fye Dyson equation,

$$(G - N)e^V = N(G_0 - 1)e^V = G - 1, \tag{4.39}$$

and remembering that $G = NG_0$ allows us to write

$$N'_\sigma = N_\sigma + UB^{-1}V^T \tag{4.40}$$

where

$$U = \left[\begin{array}{c|c} \left(e^{V'(l)-V(l)} - 1\right)(G_{\sigma il} - \delta_{il}) & \left(e^{V'(l+1)-V(l+1)} - 1\right)(G_{\sigma i,l+1} - \delta_{i,l+1}) \end{array} \right] \tag{4.41}$$

$$V = \left[\begin{array}{c} N_{\sigma,l,j} \\ \hline N_{\sigma,l+1,j} \end{array} \right] \tag{4.42}$$

$$B = I + \left[\begin{array}{cc} (1 - G_{ll})\lambda_l & -G_{l,l+1}\lambda_{l+1} \\ -G_{l+1,l}\lambda_l & (1 - G_{l+1,l+1})\lambda_{l+1} \end{array} \right] \tag{4.43}$$

$$\lambda_l = e^{V'(l)-V(l)} - 1 \tag{4.44}$$

Note in the above that we are now expressing things in terms of the interacting Green's function, $G = NG_0$, rather than the bare Green's functions, G_0. We have also dropped the spin index, σ, for convenience.

The critical quantity to access during the Monte Carlo procedure is the ratios of determinants of the N matrices, $\frac{\det N'}{\det N}$, since they are used in calculating acceptance probabilities.

$$\det N' = \det\left(N + UB^{-1}V\right) = \det(N)\det(B + V^T N^{-1}U)\det(B^{-1}) \tag{4.45}$$

In the above expression we have used the matrix determinant lemma, which states that

$$\det(A + UWV^T) = \det(A)\det(W^{-1} + V^T A^{-1}U)\det(W). \tag{4.46}$$

Thus, in order to compute $\frac{\det N'}{\det N}$, we need

$$\det(B^{-1}) = \frac{1}{\det B} = \frac{1}{1 + (1 - G_{l+1,l+1}\lambda_{l+1} + (1 - G_{ll})\lambda_l + (1 - G_{ll} - G_{l+1,l+1})\lambda_l\lambda_{l+1}} \tag{4.47}$$

and

$$\begin{aligned}\det(B+V^TN^{-1}U) &= \left[\begin{array}{cc} 1+(1-G_{ll})\lambda_l & -G_{l,l+1}\lambda_{l+1} \\ -G_{l+1,l}\lambda_l & 1+(1-G_{l+1,l+1})\lambda_{l+1} \end{array}\right] \\ &+ \left[\begin{array}{cc} (G_{ll}-1)\lambda_l & G_{l,l+1}\lambda_{l+1} \\ G_{l+1,l}\lambda_l & (G_{l+1,l+1}-1)\lambda_{l+1} \end{array}\right] \\ &= 1\end{aligned} \tag{4.48}$$

Therefore the determinant ratio needed when a auxiliary spin, s_i, is flipped that belongs to a vertex with $\sigma_i = \sigma_i'$ is

$$\frac{N'}{N} = \frac{1}{1+(1-G_{l+1,l+1}\lambda_{l+1}+(1-G_{ll})\lambda_l+(1-G_{ll}-G_{l+1,l+1})\lambda_l\lambda_{l+1}}. \tag{4.49}$$

When $\sigma_i \neq \sigma_i'$, we would just have to change one column of each N_σ^{-1} matrix. The resulting determinant ratio in this case is

$$\frac{N'}{N} = \frac{1}{1+(1-G_{ll})\lambda_l+(1-G_{ll})}. \tag{4.50}$$

4.6.2 Submatrix Updates for Charge Order

The next step in implementing submatrix updates is to construct a new matrix, A_σ, and see how it changes under spin flip updates. This matrix is defined to be the inverse of the Green's function matrix, G_σ.

$$\begin{aligned}A_\sigma' &= G_\sigma^{-1\prime} \\ &= (N_\sigma^{-1\prime}G_{0\sigma})^{-1} \\ &= \Big(G_\sigma + \left[\begin{array}{c|c} \lambda_l(G_\sigma(:,l)-e_l) & \lambda_{l+1}(G_\sigma(:,l+1)-e_{l+1}) \end{array}\right] \\ &\times B_l^{-1}\left[\begin{array}{c} G_\sigma(l,:) \\ \hline G_\sigma(l+1,:) \end{array}\right]\Big)^{-1} \\ &= A_\sigma - \left[\begin{array}{c|c} \lambda_l(e_l-A_\sigma(:,l)) & \lambda_{l+1}(e_{l+1}-A_\sigma(:,l+1)) \end{array}\right]\left[\begin{array}{c} e_l \\ \hline e_{l+1} \end{array}\right] \\ &= A_\sigma - \lambda_l(e_l-A_\sigma(:,l))\otimes e_l - \lambda_{l+1}(e_{l+1}-A_\sigma(:,l+1))\otimes e_{l+1}\end{aligned} \tag{4.51}$$

In the above we have again used the Woodberry formula and that $A_\sigma = G_\sigma^{-1}$. This formula tells us that the effect of a spin flip updates on the A_σ matrix is to multiply the columns l and $l+1$ by $(1+\lambda_l)$ and $(1+\lambda_{l+1})$, respectively, and then to subtract λ_l and λ_{l+1} from the matrix elements $A_{l,l}$ and $A_{l+1,l+1}$.

Let's define $\tilde{A}_\sigma$ and $\tilde{G}_\sigma$ as follows.

$$A'_\sigma = \tilde{A}_\sigma - \lambda_l e_l \otimes e_l - \lambda_{l+1} e_{l+1} \otimes e_{l+1} \tag{4.52}$$

$$\tilde{A}_\sigma = A_\sigma + \lambda_l A_\sigma(:,l) \otimes e_l + \lambda_{l+1} A_\sigma(:,l+1) \otimes e_{l+1} \tag{4.53}$$

$$\tilde{G}_\sigma = (\tilde{A}_\sigma)^{-1} \tag{4.54}$$

The determinants of these matrices are easy to calculate since $\tilde{A}_\sigma$ is obtained from multiplying columns of A_σ.

$$\det \tilde{A}_\sigma = (1+\lambda_l)(1+\lambda_{l+1}) \det A_\sigma \tag{4.55}$$

$$\det \tilde{G}_\sigma = (1+\lambda_l)^{-1}(1+\lambda_{l+1})^{-1} \det G_\sigma \tag{4.56}$$

The ratio of determinants with A_σ is given by

$$\frac{\det A'_\sigma}{\det A_\sigma} = \lambda_l \left(\frac{1+\lambda_l}{\lambda_l} - G_{ll} \right) \lambda_{l+1} \left(\frac{1+\lambda_{l+1}}{\lambda_{l+1}} - G_{l+1,l+1} \right) - \lambda_l \lambda_{l+1} G_{l+1,l} G_{l,l+1} \tag{4.57}$$

Let's now imagine that we perform a series of spin flip updates, where no auxiliary spin is flipped more than once. Depending on the vertex, $v = \{i_n, j_n, \sigma_n, \sigma'_n, s_n, \tau_n\}$, flipping the auxiliary spin s_n may require changing one or two columns, i.e. a rank one or rank two update. If m of the updates are rank two and k are rank one, and we define functions that map the i^{th} rank one or rank two update to the relevant columns in A_σ, $p(i) \rightarrow l$ and $q(i) \rightarrow l$ respectively, then we can write the total change in A_σ after these updates as follows.

Update	0	1		2		. . .	k+m
Vertex	v(0)	v(1)		v(2)			v(k+m)
Aux. Spin	$s_{v(0)}$	$s_{v(1)}$		$s_{v(2)}$			$s_{v(k+m)}$
Rank	1	2		2			1
Columns	p(0)	q(0)	q(0)+1	q(1)	q(1)+1		p(k)
Rank 1 Index	0	1	2	3	4		g=k+2m
Rank 1 Column	$\phi(0)$	$\phi(1)$	$\phi(2)$	$\phi(3)$	$\phi(4)$		$\phi(k+2m)$

Table 4.1: Example of the relationship between the spin flip indices used in the submatrix algorithm derivation, in a case where two rank two updates follow a rank one update. The new index ϕ treats all the spin flips as though they are rank 1 updates.

$$\begin{aligned} A_\sigma^{k+m} = A_\sigma^0 &+ \sum_{i=0}^{k} \lambda_{p(i)} \left(A_\sigma^0(:, p(i)) - e_{p(i)} \right) \otimes e_{p(i)} \\ &+ \sum_{i=0}^{m} \lambda_{q(i)} \left(A_\sigma^0(:, q(i)) - e_{q(i)} \right) \otimes e_{q(i)} \\ &+ \sum_{i=0}^{m} \lambda_{q(i)+1} \left(A_\sigma^0(:, q(i)+1) - e_{q(i)+1} \right) \otimes e_{q(i)+1} \end{aligned} \tag{4.58}$$

However, this has the same form as a series of $k+2m$ rank one updates. We now define an index, $\phi(i)$, that maps the $i = 0, 1, \ldots g = k+2m$ rank one updates to the correct column indices. The relationship between these indices is shown in Table 4.1.

The rule to update A_σ after many spin flips is a bit simpler with this new index.

$$A_\sigma^g = A_\sigma^0 + \sum_{i=0}^{g} \lambda_{\phi(i)} \left(A_0(:, \phi(i)) - e_{\phi(i)} \right) \otimes e_{\phi(i)} \tag{4.59}$$

At this point we can now follow the original submatrix formalism developed for rank 1 updates [25, 98]. We can rewrite the above expression as follows.

$$A_\sigma^g = \tilde{A}_\sigma^g - X_g Y_g^T \tag{4.60}$$

$$\tilde{A}_\sigma^g = A_\sigma^0 + \sum_{i=0}^{g} \lambda_{\phi(i)} A_\sigma^0(:, \phi(i)) \otimes e_{\phi(i)} \tag{4.61}$$

$$X_g = \left[\begin{array}{c|c|c|c} \gamma_{\phi(0)} e_{\phi(0)} & \gamma_{\phi(1)} e_{\phi(1)} & \ldots & \gamma_{\phi(g)} e_{\phi(g)} \end{array} \right] \tag{4.62}$$

$$Y_g = \left[\begin{array}{c|c|c|c} e_{\phi(0)} & e_{\phi(1)} & \dots & e_{\phi(g)} \end{array}\right] \tag{4.63}$$

If we once again define $\tilde{G}^g_\sigma = (\tilde{A}^g_\sigma)^{-1}$, then $\tilde{G}^g_\sigma(\phi(k), :) = G(\phi(k), :)/(1 + \gamma_\phi(k))$. This allows us to compute

$$\det(\tilde{A}^g_\sigma) = \prod_{i=0}^{g}(1 + \gamma_{\phi(i)}) \det(A^0), \tag{4.64}$$

$$\det(\tilde{G}^g_\sigma) = \prod_{i=0}^{g}(\frac{1}{1 + \gamma_{\phi(i)}}) \det(G^0). \tag{4.65}$$

Now the effect of many spin flips on the determinant of A^g_σ can be computed.

$$\begin{aligned}
\det(A^g_\sigma) &= \det(\tilde{A}^g_\sigma - X_g Y_g^T) \\
&= \det(\tilde{A}^g_\sigma) \det(I - Y_g^T \tilde{G}^g_\sigma X_g) \\
&= \left(\prod_{i=0}^{g}(1 + \lambda_{\phi(i)}) \det(A^0)\right) (-1)^{g+1} \left(\prod_{i=0}^{g} \frac{\lambda_{\phi(i)}}{1 + \lambda_{\phi(i)}}\right) \det(\Gamma_g) \\
&= (-1)^{g+1} \left(\prod_{i=0}^{g} \lambda_{\phi(i)}\right) \det(\Gamma_g) \det(A^0_\sigma)
\end{aligned} \tag{4.66}$$

The matrix Γ_g is a matrix of rank gxg defined as follows.

$$\Gamma_g = \begin{bmatrix}
G^0_\sigma(\phi(0), \phi(0)) - \frac{1+\lambda_{\phi(0)}}{\lambda_{\phi(0)}} & \dots & G^0_\sigma(\phi(0), \phi(g-1)) & G^0_\sigma(\phi(0), \phi(g)) \\
\vdots & & & \vdots \\
G^0_\sigma(\phi(g-1), \phi(0)) & \dots & G^0_\sigma(\phi(g-1), \phi(g-1)) & G^0_\sigma(\phi(g-1), \phi(g)) \\
G^0_\sigma(\phi(g), \phi(0)) & \dots & G^0_\sigma(\phi(g), \phi(g-1)) & G^0_\sigma(\phi(g), \phi(g)) - \frac{1+\lambda_{\phi(g)}}{\lambda_{\phi(g)}}
\end{bmatrix} \tag{4.67}$$

As we choose and accept these g spin flip updates, we can efficiently compute the determinant of Γ_g by storing the matrix as an LU decomposition. For example, when performing a single spin flip we can express Γ_m in terms of Γ_{m-1} as follows.

$$\Gamma_m = \begin{bmatrix} \Gamma_{m-1} & s \\ w^\dagger & d \end{bmatrix} = L_m U_m = \begin{bmatrix} L_{m-1} & 0 \\ x^\dagger & 1 \end{bmatrix} \begin{bmatrix} U_{m-1} & y \\ 0 & \beta \end{bmatrix} \tag{4.68}$$

Thus, in order to update the matrix $\Gamma_{m-1} \rightarrow \Gamma_m$, we just need to compute the following quantities.

$$\begin{aligned} s &= G^0_\sigma(\phi(0) : \phi(m-1), \phi(m)) \\ d &= G^0_\sigma(\phi(m), \phi(m)) - \frac{1+\lambda_{\phi(m)}}{\lambda_{\phi(m)}} \\ w^\dagger &= G^0_\sigma(\phi(m), \phi(0) : \phi(m-1)) \end{aligned} \tag{4.69}$$

This allows us to write $\det(\Gamma_m) = \beta \det(\Gamma_{m-1})$. Applying this result to Eq. 4.66 allows us to obtain a result for the ratio of determinants between A^m_σ and A^{m-1}_σ.

$$\det(A^m_\sigma) = -\lambda_{\phi(m)} \beta \det(A^{m-1}_\sigma) \tag{4.70}$$

The quantity we actually need during the CT-AUX algorithm is the ratio between N_σ matrices. Since $A^m_\sigma = (G^m_\sigma)^{-1} = G^{-1}_{0\sigma}(N^m_\sigma)^{-1}$, the result we need in order to accept or reject spin flip updates is,

$$\frac{\det(N^m_\sigma)}{\det(N^{m-1}_\sigma)} = \frac{-1}{\lambda_{\phi(m)}\beta} \tag{4.71}$$

Note that is the spin flip involves a vertex with $\sigma = \sigma'$, we are really performing a rank two update, so we need to apply the rank one result twice in order to get the appropriate ratio.

$$\frac{\det(N^m_\sigma)}{\det(N^{m-2}_\sigma)} = \frac{1}{\lambda_{\phi(m)}\beta_m \lambda_{\phi(m-1)}\beta_{m-1}} \tag{4.72}$$

After performing a set of spin flip updates, we need to recompute the N_σ and G_σ matrices. The formulas for performing these updates are as follows. [98]

$$\begin{aligned} G^g_\sigma &= D^{-1}(G^0_\sigma - G^0_\sigma(:, \phi(:))(\Gamma^g)^{-1} G^0_\sigma(\phi(:), :) \\ N^g_\sigma &= D^{-1}(N^0_\sigma - G^0_\sigma(:, \phi(:))(\Gamma^g)^{-1} N^0_\sigma(\phi(:), :) \\ D^{-1}(\phi(i), \phi(i)) &= \frac{1}{1+\lambda_{\phi(i)}} \end{aligned} \tag{4.73}$$

Where D^{-1} is the $g \times g$ identity matrix aside from the indicated elements. The rank k of the G_σ and N_σ matrices is not changed by spin flips. Γ^g is a rank $g < k$ matrix. The notation $G^0_\sigma(:, \phi(:))$ means the $k \times g$ matrix formed out of the g rows of G^0_σ indicated by the g different values of ϕ.

It is important to note that in these equations, G^0_σ indicates the matrix of interacting Green's functions as it stands before the g updates, given in terms of the bare Green's function matrix, $G_{0\sigma}$ by $G_\sigma^0 = N_\sigma^0 G_{0\sigma}$. Computing the full interacting Green's function matrix is an $\mathcal{O}(k^3)$ operation, but the above formulas tell us that we only need certain elements of this matrix. In practice we only compute the elements we actually need via the $\mathcal{O}(k)$ operations $(G_\sigma^0)_{ij} = \sum_l (N_\sigma)_{il}(G_{0\sigma})_{lj}$.

4.6.3 Submatrix Update Procedure

To recap, these results are pieced together into the following submatrix update procedure.

1. Starting off with the matrices N_σ^0 and $G_{0\sigma}$, as well as the current set of k vertices $v_n = \{i_n, j_n, \sigma_n, \sigma_n', s_n, \tau_n\}$, pick some number, $m < k$, of unique auxiliary spins to try to flip.

2. For each proposed spin flip, determine whether or not to accept the move based on the Metropolis algorithm acceptance probability, W_{acc}.

   $$W_{acc} = \min\left(1, \frac{\det(N_\uparrow(s'))\det(N_\downarrow(s'))}{\det(N_\uparrow(s))\det(N_\downarrow(s))}\right) \tag{4.74}$$

   The ratios appearing in this probability can be computed from the Γ_σ matrices via Eq. 4.71 or Eq. 4.72, depending on which type of vertex the auxiliary spin belongs to. Note that this requires computing elements of the interacting Green's function matrix, $G_\sigma^0 = N_\sigma^0 G_{0\sigma}$.

3. If the flip is rejected, then we simply go on to the next spin flip candidate. If the flip is accepted, we need to update the LU decomposition of the Γ_σ matrices via Eq. 4.68. We also make sure to record which vertices have been flipped.

4. After attempting to flip m vertices, number g will have been accepted. Before continuing on to another series of spin flip updates or possibly insertion/removal updates, we need to update the N_σ matrices via Eq. 4.73.

Chapter 5

Dual Fermions

This chapter describes a project to study the behavior of the 2D Hubbard model with the dual fermions method. We present results that demonstrate the high momentum resolution that is achievable with this technique, including the detailed evolution of quantities such as spectral functions and mass renormalizations along the Fermi surface.

5.1 Introduction

A challenge for cluster methods like DCA is the limited access to momentum space. Rather than computing quantities like Green's functions and densities throughout the Brillouin zone, the DCA self-consistency condition only produces results for a limited number of cluster momenta, $\vec{K}$ [103, 14]. More momentum points can be obtained by increasing the size of the impurity cluster, but in many cases the increase in computational cost makes this path impractical [16]. Additionally, the shape of the finite clusters used can significantly affect simulation results [167, 168, 169]. This situation can make it difficult to study systems that exhibit strongly momentum dependent behavior, and also to compare computational results to experiments that obtain momentum space information, such as ARPES [131]. Although some attempts have been made to interpolate the DCA data, doing so is non-trivial and can result in non-causality [103, 169].

A relatively new method for obtaining more fine-grained momentum space information from a DMFT calculation is Dual Fermions [170, 171, 89]. This chapter describes the Dual Fermions method and discusses some results from application to the 2D Hubbard model. The Dual Fermions expansion is derived and its conceptual foundation is described. The Dual Fermions Ladder Approximation (DFLA), [172, 173, 174] which approximates the resulting diagrammatic series as a sum over an infinite series of ladder diagrams, is derived. Then some examples of using the Dual Fermions technique to obtain high momentum space resolution Green's function, self-energies, bandstructures, and mass renormalizations for the 2D Hubbard model are presented.

5.2 Dual Fermions Formalism

The Dual Fermions technique is a recently developed method for calculating the path integrals that arise when studying quantum many body systems, such as the 2D Hubbard model [171]. The technique has attracted attention because of its ability to provide access to fine grained momentum dependent quantities at relatively low computational cost [175, 176, 172, 177, 178]. In comparison, obtaining such high resolution momentum space information with cluster theories, such as DCA, requires simulations for large clusters whose computational cost often scales exponentially with the number of cluster sites, N_C [169, 14].

The ability to compute quantities throughout momentum space is attractive for several reasons. One reason is that although interpolation schemes exist for cluster theories, the resulting data is subject to the details of the fitting procedure rather than dictated by the underlying physics of the model [169]. Furthermore, such interpolation schemes can run into causality issues, leading to nonphysical results [150]. Secondly, various interesting phenomena in strongly correlated systems seem to exhibit strong momentum dependence, and the course grid of momentum points simulated by cluster theories can be insufficient for carefully studying effects like momentum dependent metal / insulators transitions [177].

However, the greatest motivation for high momentum space resolution techniques comes from the need to compare computational results with experiments. Some of the most important experimental techniques used in strongly correlated physics, such as ARPES and quantum oscillations, [131] yield fine grained momentum space data on material bandstructures and Fermi surface structures. Such results can be hard to compare with cluster theories, since methods like DCA only provide results at certain points in momentum space dictated by the cluster geometry. While more momentum points can be in theory simulated by increasing the size of the simulation cluster, this quickly becomes computational intractable in regions of parameter space with a fermion sign problem.

5.2.1 Dual Fermions Expansion Derivation

Here we will demonstrate how to use the Dual Fermions method with the 2D single-band Hubbard model. We will follow Refs [179, 180, 89]. The Hamiltonian for the Hubbard model is

$$H = \sum_{k\sigma} \left(\epsilon(k) - \mu\right) c^{\dagger}_{k\sigma} c_{k\sigma} + U \sum_{i} n_{i\uparrow} n_{i\downarrow} \tag{5.1}$$

where $c/c^{\dagger}$ are particle creation and annihilation operators and $\epsilon(k) = -2t(\cos(k_x) + \cos(k_y))$ is the single particle dispersion on a square lattice. The Dual Fermions expansion is derived within the action formalism, and the Hubbard Hamiltonian corresponds to the following action, S.

$$S[c, c^*] = \sum_{\omega k\sigma} \left(\epsilon(k) - \mu - i\omega\right) c^*_{\omega k\sigma} c_{\omega k\sigma} + U \sum_{i} \int_0^{\beta} n_{i\uparrow} n_{i\downarrow} d\tau \tag{5.2}$$

Note that in the action the formalism, the creation and annihilation operators of the Hamiltonian have been replaced with the grassmann numbers c/c^*, β is the inverse temperature, and $\omega = (2n+1)\pi/\beta$ are fermionic Matsubara frequencies [3, 91].

The above action describes an infinite lattice system, involving sums over all the available single particle momenta, k. In order to make further progress, we define a single-site impurity system that is coupled to a bath via a frequency dependent hybridization, Δ_{ω}. The action for this impurity, S_{imp}, is given by

$$S_{imp}[c, c^*] = \sum_{\omega\sigma} \left(\Delta_{\omega} - \mu - i\omega\right) c^*_{\omega\sigma} c_{\omega\sigma} + U \int_0^{\beta} n_{i\uparrow} n_{i\downarrow} d\tau. \tag{5.3}$$

Since the hybridization is independent of k, we can write write the lattice action in terms of the impurity action.

$$S[c, c^*] = \sum_{i} S_{imp}[c_i, c^*_i] - \sum_{\omega k\sigma} \left(\Delta_{\omega} - \epsilon(k)\right) c^*_{\omega k\sigma} c_{\omega k\sigma} \tag{5.4}$$

All we have done at this point is add zero to the original action, in the form of adding and subtracting the new hybridization function, Δ_{ω}. Our next step is to introduce new dual variables, f/f^*, via the identity

$$e^{A^2 c^*_{\omega k\sigma} c_{\omega k\sigma}} = \left(\frac{A}{\alpha}\right)^2 \int e^{-\alpha\left(c^*_{\omega k\sigma} f_{\omega k\sigma} + f^*_{\omega k\sigma} c_{\omega k\sigma}\right) - \alpha^2 A^2 f^*_{\omega k\sigma} f_{\omega k\sigma}} df^*_{\omega k\sigma} df_{\omega k\sigma}. \tag{5.5}$$

This identity is simply a Gaussian integral over grassmann numbers, and is referred to as a dual transformation [91]. If we choose $A^2 = (\Delta_\omega - \epsilon(k))$ and assume that $\alpha = \alpha_{\omega\sigma}$ is independent of momentum, then we can express the partition function in terms of a transformed action that depends on both c/c^* and f/f^*.

$$Z = \int e^{-S[c,c^*]} Dc^* Dc = \int\int e^{-S[c,c^*,f,f^*]} Df^* Df Dc^* Dc \tag{5.6}$$

Where new action takes the following form.

$$\begin{aligned} S[c,c^*,f,f^*] = &-\sum_{\omega k} \ln\left(\alpha_{\omega\sigma}^{-2}(\Delta_\omega - \epsilon(k)\right) + \sum_i S_{imp}[c_i, c_i^*] \\ &+ \sum_{\omega k\sigma}\left(\alpha_{\omega\sigma}(c^*_{\omega k\sigma} f_{\omega k\sigma} + f^*_{\omega k\sigma} c_{\omega k\sigma}) + \alpha^2_{\omega\sigma}(\Delta_\omega - \epsilon(k))^{-1} f^*_{\omega k\sigma} f_{\omega k\sigma}\right) \end{aligned} \tag{5.7}$$

We now have two forms of the action,and thus two forms on the partition function, that should describe the same physics. For convenience, let's give these partition functions unique names.

$$Z' = \int e^{-S[c,c^*]} Dc^* Dc \tag{5.8}$$

$$Z'' = \int\int e^{-S[c,c^*,f,f^*]} Df^* Df Dc^* Dc \tag{5.9}$$

Both of these partition functions should give the same results for the single particle Green's function, $G_{\omega k\sigma} = \langle c^*_{\omega k\sigma} c_{\omega k\sigma}\rangle$. For the partition function Z', this Green's function could be obtained by varying the single particle dispersion, $\epsilon(k) \rightarrow \delta\epsilon_{\omega k}$.

$$G_{\omega k\sigma} = \langle c^*_{\omega k\sigma} c_{\omega k\sigma}\rangle = \frac{\delta Z'}{\delta\epsilon_{\omega k}}|_{\delta\epsilon_{\omega k}=0} \tag{5.10}$$

If we perform the same calculation with Z'', we should obtain the same physical result.

$$\frac{\delta Z''}{\delta \epsilon_{\omega k}}|_{\delta\epsilon_{\omega k}=0} = (\Delta_\omega - \epsilon(k))^{-1} + (\Delta_\omega - \epsilon(k))^{-1}\alpha_{\omega\sigma}\langle f^*_{\omega k\sigma} f_{\omega k\sigma}\rangle \alpha_{\omega\sigma}(\Delta_\omega - \epsilon(k))^{-1} \tag{5.11}$$

Comparisons of these two expressions leads to the following relationship for the single particle Green's function.

$$G_{\omega k\sigma} = (\Delta_\omega - \epsilon(k))^{-1} + (\Delta_\omega - \epsilon(k))^{-1}\alpha_{\omega\sigma} G^{dual}_{\omega k\sigma} \alpha_{\omega\sigma}(\Delta_\omega - \epsilon(k))^{-1} \tag{5.12}$$

Where we have defined the dual Green's function, $G^{dual}_{\omega k\sigma} = \langle f^*_{\omega k\sigma} f_{\omega k\sigma}\rangle$. This expression allows us to express the full lattice Green's function in terms of the solution to the dual problem.

At this point we can now attempt to integrate out the original lattice degrees of freedom, c/c^*, and obtain an effective action involving only the dual fermions, f/f^*. We can rewrite the dual fermion action as,

$$\begin{aligned} S[c, c^*, f, f^*] = &-\sum_{\omega k} \ln\left(\alpha^{-2}_{\omega\sigma}(\Delta_\omega - \epsilon(k)\right) + \sum_i S_{imp}[c_i, c^*_i] \\ &+ \sum_{\omega i\sigma} \left(\alpha_{\omega\sigma}(c^*_{\omega i\sigma} f_{\omega i\sigma} + f^*_{\omega i\sigma} c_{\omega i\sigma})\right) + \sum_{\omega k\sigma} \left(\alpha^2_{\omega\sigma}(\Delta_\omega - \epsilon(k))^{-1} f^*_{\omega k\sigma} f_{\omega k\sigma}\right), \end{aligned} \tag{5.13}$$

since we have assumed that $\alpha_{\omega\sigma}$ is independent of momentum and $\sum_k f^*_k c_k + c^*_k f_k = \sum_i f^*_i c_i + c^*_i f_i$. The terms in the action involving the original lattice degree of freedom are now purely local, allowing us to write the action as a sum of independent lattice site actions.

$$\begin{aligned} S[c, c^*, f, f^*] = &-\sum_{\omega k} \ln\left(\alpha^{-2}_{\omega\sigma}(\Delta_\omega - \epsilon(k)\right) + \sum_i S_{site}[c_i, c^*_i, f_i, f^*_i] \\ &+ \sum_{\omega k\sigma} \left(\alpha^2_{\omega\sigma}(\Delta_\omega - \epsilon(k))^{-1} f^*_{\omega k\sigma} f_{\omega k\sigma}\right) \end{aligned} \tag{5.14}$$

$$S_{site}[c_i, c^*_i, f_i, f^*_i] = S_{imp}[c_i, c^*_i] + \sum_\omega \alpha_{\omega\sigma}\left(f^*_{i\omega} c_{i\omega} + c^*_{i\omega} f_{i\omega}\right) \tag{5.15}$$

We can integrate over the c_i/c^*_i for each site independently. This allows us to define a dual potential, $V_i[f_i^*, f_i]$, as follows.

$$\int e^{-S_{site}[c_i,c_i^*,f_i,f_i^*]} Dc_i^* Dc_i = Z_i^{imp} e^{\sum_{\omega\sigma} \alpha^2_{\omega\sigma} g_\omega f^*_{\omega i\sigma} f_{\omega i\omega} - V[f_i,f_i^*]} \tag{5.16}$$

$$Z_i^{imp} = \int e^{-S_{imp}[c_i^*,c_i]} Dc_i^* DC_i \tag{5.17}$$

$$g_\omega = \langle c_\omega c_\omega^* \rangle_{S_{imp}} \tag{5.18}$$

Here we have defined the impurity Green's function, g_ω, and have assumed that it is translationally invariant. Expanding both sides of Eq. 5.16 order by order allows us to find explicit expressions for the dual potential. Here we will perform the expansion to show how the first order expression for $V_i[c_i, c_i^*]$ arises, which is the most common the approximation used in the dual fermions literature.

Since the impurity action, S_{imp}, is quadratic in c/c^*, we can expand the left side of Eq. 5.16 as follows.

$$\begin{aligned}
\int e^{-S_{site}[c_i,c_i^*,f_i,f_i^*]} Dc_i^* Dc_i &= \int e^{-S_{imp}[c_i,c_i^*]} \sum_k \frac{(-1)^k}{k!} \left(\sum_\omega \alpha_{\omega\sigma} [f^*_{i\omega} c_{i\omega} + c^*_{i\omega} f_{i\omega}] \right)^k Dc_i^* Dc_i \\
&= \int e^{-S_{imp}[c_i,c_i^*]} \left[1 + \frac{1}{2} \left(\sum_\omega \alpha_{\omega\sigma} [f^*_{i\omega} c_{i\omega} + c^*_{i\omega} f_{i\omega}] \right)^2 \right. \\
&\quad \left. + \frac{1}{4!} \left(\sum_\omega \alpha_{\omega\sigma} [f^*_{i\omega} c_{i\omega} + c^*_{i\omega} f_{i\omega}] \right)^4 + \dots \right] Dc_i^* Dc_i \\
&\approx Z_i^{imp} \left(1 + \sum_\omega \alpha^2_\omega g_\omega f^*_{i\omega} f_{i\omega} \right) \\
&\quad + \int e^{-S_{imp}[c_i,c_i^*]} \frac{1}{4!} \left(\sum_\omega \alpha_{\omega\sigma} [f^*_{i\omega} c_{i\omega} + c^*_{i\omega} f_{i\omega}] \right)^4 Dc_i^* Dc_i
\end{aligned} \tag{5.19}$$

In the above we have truncated the expansion at fourth order, made use of the impurity Green's function definition $g_\omega = \int e^{iS_{imp}[c_i,c_i^*]} c_{i\omega} c^*_{i\omega} Dc_i^* Dc_i / Z_i^{imp}$, and noted that correlation functions with an odd number of grassmann variables are zero, i.e. $\langle c_{i\omega} \rangle = 0$. On the other hand, expanding the right side of Eq. 5.16 yields the following.

$$
\begin{aligned}
Z_i^{imp} e^{\sum_{\omega\sigma} \alpha_{\omega\sigma}^2 g_\omega f_{\omega i\sigma}^* f_{\omega i\omega} - V[f_i, f_i^*]} = Z_i^{imp} \Bigg[& 1 + \sum_{\omega\sigma} \alpha_{\omega\sigma}^2 g_\omega f_{\omega i\sigma}^* f_{\omega i\sigma} - V_i[f_i, f_i^*] \\
& + \left(\sum_{\omega\sigma} \alpha_{\omega\sigma}^2 g_\omega f_{\omega i\sigma}^* f_{\omega i\sigma} - V_i[f_i, f_i^*] \right)^2 + \ldots \Bigg]
\end{aligned} \tag{5.20}
$$

If we keep only terms that are quartic in the dual fields, f/f^*, then comparing these two expansions tells us that the dual potential is given to first order by,

$$
\begin{aligned}
V_i[f_i, f_i^*] = \frac{1}{Z_i^{imp}} \int e^{-S_{imp}[c_i, c_i^*]} \frac{1}{4!} \left(\sum_{\omega\sigma} \alpha_{\omega\sigma} [f_{i\omega\sigma}^* c_{i\omega\sigma} + c_{i\omega\sigma}^* f_{i\omega\sigma}] \right)^4 Dc_i^* Dc_i \\
- \left(\sum_{\omega} \alpha_{\omega\sigma}^2 g_\omega f_{\omega i\sigma}^* f_{\omega i\sigma} \right)^2
\end{aligned} \tag{5.21}
$$

The parameter $\alpha_{\omega\sigma}$ is as yet arbitrary. If we set $\alpha_{\omega\sigma} = g_\omega^{-1}$ and carry out the integration over c/c^*, we obtain an approximation for the dual potential in terms of the two particle impurity vertex, γ_{1234}, where we now use a collective index $1 = \{\omega_1, \sigma_1\}$.

$$
V_i[f_i, f_i^*] = \frac{1}{4} \sum_{1234} \gamma_{1234} f_{i1}^* f_{i2}^* f_{i3} f_{i4} \tag{5.22}
$$

The vertex comes from the solution of the impurity problem, which can be obtained from a DMFT calculation.

$$
\gamma_{1234} = g_1^{-1} g_2^{-1} \left[\chi_{1234} - \chi_{1234}^0 \right] g_3^{-1} g_4^{-1} \tag{5.23}
$$

Where χ is just the impurity two particle Green's function, and χ^0 is the Hartree-Fock (non-interacting) contribution.

$$
\chi_{1234} = \langle c_1 c_2 c_3^* c_4^* \rangle_{imp} \tag{5.24}
$$

$$
\chi_{1234}^0 = g_1 g_2 (\delta_{14}\delta_{23} - \delta_{13}\delta_{24}) \tag{5.25}
$$

This allows us to fully replace the c/c^* degrees of freedom. Dropping the inconsequential constant term, the total action is now given by the following.

$$\begin{aligned} S &= -\sum_i S_{site} - \sum_{\omega k\sigma} \left(\alpha^2_{\omega\sigma}(\Delta_\omega - \epsilon(k))\right)^{-1} f^*_{\omega k\sigma} f_{\omega k\sigma} \\ &= -\sum_{k\omega\sigma} f^*_{\omega k\sigma}[\tilde{G}^0_\omega(k)]^{-1} f^*_{\omega k\sigma} + \sum_i V_i[f^*_i, f_i] \end{aligned} \tag{5.26}$$

Where we have now defined the bare Green's function for the dual fermions, f/f^*.

$$\begin{aligned} \tilde{G}^0_\omega(k) &= -g_\omega \left[(\Delta_\omega - \epsilon(k))^{-1} + g_\omega\right]^{-1} g_\omega \\ &= (g^{-1}_\omega + \Delta_\omega - \epsilon(k))^{-1} - g_\omega \end{aligned} \tag{5.27}$$

The variables f/f^* have now taken on a life of their own. While they were originally introduced as a purely mathematical artifact by the dual transformation, we now see that the Green's functions for the electrons (our 'original' fermions) can be expressed in terms of the Green's function of these new 'dual fermions'.

5.3 Dual Fermion Ladder Approximation

The Dual Fermions calculations presented in this thesis are performed within the Dual Fermion Ladder Approximation (DFLA) [171, 177] using the OpenDF software package [173]. While the dual fermions expansion given by Eq. 5.26 is in theory exact, in practice a number of approximations are required in order to obtain a computationally useful algorithm.

The two approximations used in the DFLA are to keep only the lowest order contribution to the dual interaction, $V[f^*, f]$, and to compute only a single infinite series of diagrams in the expansion of the dual fermions action and calculation of the dual self-energy, $\tilde{\Sigma}_{\omega k}$. The approximation for the dual interaction was computed in Eq. 5.22, and is given in terms of the impurity vertex function, γ, related to the two particle Green's function. Under this approximation $V[f^*, f]$ is a simple, local four leg vertex, although the full vertex would include six, eight, etc. leg contributions.

Given the four leg dual fermion interaction vertex, γ, and the dual Green's function, $\tilde{G}_\omega(k)$, one can construct diagrammatic expansions of the dual fermions action, Eq. 5.26 Although sampling the entire series is possible via diagrammatic Monte Carlo [181], in practice a much simpler ladder approximation can still yield significant corrections to the DMFT result. This ladder is constructed from the bare vertex, γ, and the bubble diagram, $\tilde{\chi}_{\Omega\omega}(q)$, to define a dressed vertex, $\Gamma_{\Omega\omega\omega'}(q)$, that can be used to compute the dual self-energy, $\tilde{\Sigma}_\omega(k)$.

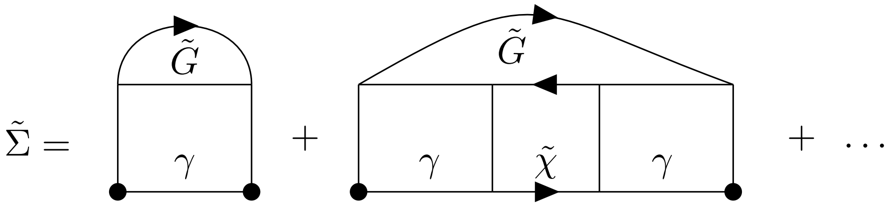

Figure 5.1: The first and second order diagrams that contribute to the dual self-energy, $\tilde{\Sigma}$, within the Dual Fermions Ladder Approximation (DFLA).

The first few diagrams that contribute to the dual self-energy are shown in Fig. 5.1. The bare vertex γ is defined as in Eq. 5.23, while the bubble, χ, and full vertex, Γ, are defined as follows [34].

$$\Gamma_{\Omega\omega\omega'}(q) = \gamma_{\Omega\omega\omega'} + \sum_{\omega''} \gamma_{\Omega\omega\omega'}\tilde{\chi}_{\Omega\omega''}(q)\Gamma_{\Omega\omega''\omega'}(q) \tag{5.28}$$

$$\tilde{\chi}_{\Omega\omega}(q) = -\frac{T}{N_k^D}\sum_k \tilde{G}_{\omega k}\tilde{G}_{\omega+\Omega,k+q} \tag{5.29}$$

Where N_k is the number of momentum points used to approximate the integral over the Brillouin zone. Based on Fig. 5.1, the dual self-energy can then be expressed as follows.

$$\tilde{\Sigma}_\omega(k) = \frac{T}{2N_k^D}\sum_{\Omega q}\Gamma_{\Omega\omega\omega}(q)\tilde{G}_\omega(k+q) \tag{5.30}$$

Note that if we hold the bosonic frequency, Ω, and the momentum, q, constant, then the base vertex can be expressed as a matrix equation in the Matsubara frequencies, ω and ω'.

$$\begin{aligned}\hat{\Gamma} &= \gamma + \gamma\chi\hat{\Gamma}\\ &= (1-\gamma\chi)^{-1}\hat{\Gamma}\end{aligned} \tag{5.31}$$

This matrix form is both easier to analyze and indicates the radius of convergence of the ladder series, Eq. 5.29. As long as the largest eigenvalue of $1-\gamma\chi$ is smaller than one, the ladder series can be summed and Eq. 5.31 holds. However, once this eigenvalue approaches and crosses one, the ladder series diverges and this version of the dual fermions method fails. For example, this divergence is known to occur when approaching the AFM transition in the Hubbard model, providing a lower bound on the range of applicable temperatures.

The dual Green's function can then be computed from the self-energy via the Dysons equation.

$$\tilde{G}_\omega(k) = \left[\tilde{G}^0_\omega(k) - \tilde{\Sigma}_\omega(k)\right]^{-1} \tag{5.32}$$

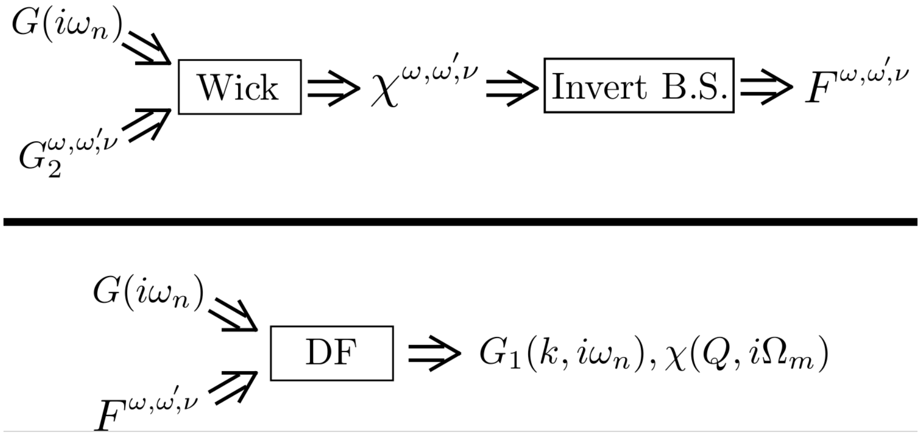

Figure 5.2: Schematic of the process used to perform a dual fermions simulation. We begin with a DMFT calculation that provides the two particle vertex and converged impurity Green's function. These are then used as inputs for a dual fermions calculation.

This closes an iterative process for computing the dual Green's function. Starting with the bare Green's function, $\tilde{G}^0_\omega(k)$, defined from the DMFT results by Eq. 5.27, we can set $\tilde{G}_\omega(k) = \tilde{G}^0_\omega(k)$, compute the above dual fermion vertex function, compute a new result for $\tilde{G}_\omega(k)$ via Eq. 5.32, and repeat until the dual Green's function converges. Once the dual fermions computation is finished, we can use the results to obtain corrections to the lattice Green's function, $G_\omega(k)$, via Eq. 5.12. A schematic of the dual fermions calculation with DMFT is shown in Fig. 5.2.

5.4 Dual Fermions for the 2D Hubbard Model

In this section we will present dual fermions calculations performed on the 2D Hubbard model. We will discuss some results on densities, Green's functions, and fully resolved momentum space band structures and Fermi surfaces, as well as some measurements of the renormalized mass along the Fermi surface.

The dual fermions results presented here use the outputs of single site DMFT simulations performed with a CT-AUX impurity solver [81, 25]. It is thus worthwhile to investigate how the dual fermions calculation modifies the DMFT results. In particular, it is known that the 2D Hubbard model displays the Mott-Insulator transition, a correlation effect in which electrons become localized due to an increase in the interaction strength, U [81]. This transition is one of the most popular strongly correlated phenomena to discuss, because it is simple to understand intuitively, plays an important role in certain real materials, and can not be understood within an independent particle picture.

Figs. 5.3 and 5.4 present a study of the insulating transition and compare the predictions of single site DMFT and the dual fermions method. Fig. 5.3 depicts the density versus chemical potential, μ, curves found by both methods, for a series of interaction strengths, U, and next-nearest neighbor hopping, t'.

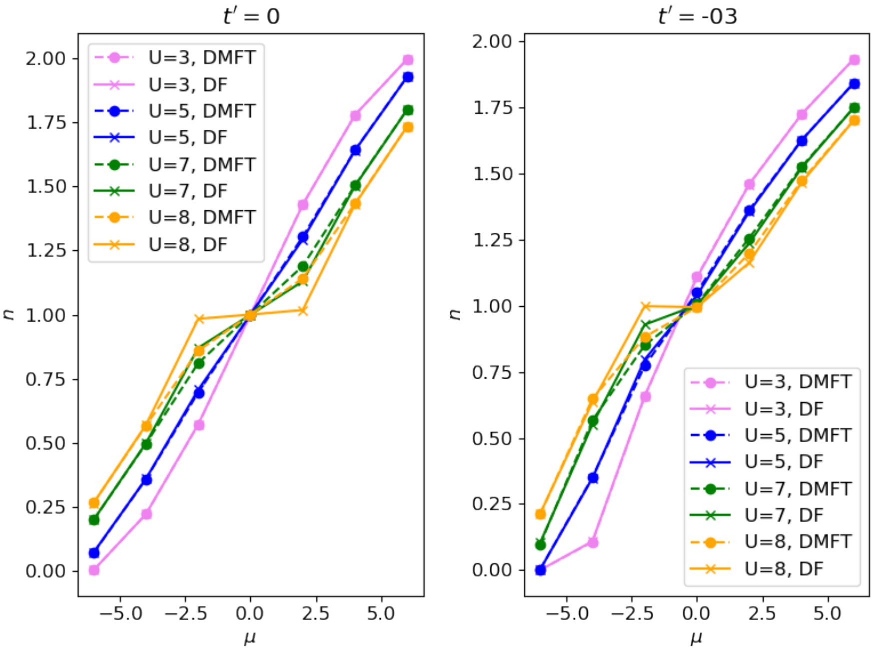

Figure 5.3: Comparison of the density vs μ curves between single site DMFT and dual fermions. As the interaction U is increased, the dual fermions corrections to the average density become significant close to half-filling, $\mu = 0$.

From this we see that the corrections from dual fermions become significant at

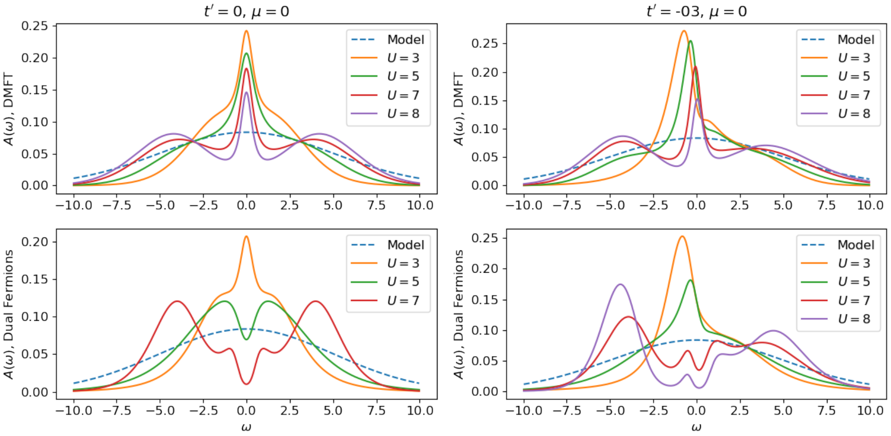

Figure 5.4: Evolution of the total spectral function as a function of interaction strength and nearest neighbor hopping, t', comparing single site DMFT to Dual Fermions. The Dual Fermions method opens an electronic gap at a much lower energy than DMFT. The finite t' breaks the particle-hole symmetry of the system, as reflected in the lack of symmetry in the spectral function across $\omega = 0$.

larger interaction strengths around half-filling, and generally has the effect of flattening out the n vs μ curve. This flattening out reflects a decrease in the compressibility of the system, which is commonly associated with the formation of an electronic gap, i.e. a transition from metallic to insulating states. The hopping t' has the predicted effects of breaking particle-hole symmetry, so that the curve is not symmetric about half-filling, $\mu = 0$.

The general trend that dual fermions reduces the interaction strength at which the system becomes insulating is supported by the spectral function data shown in Fig. 5.4. This data is obtained by analytically continuing the Green's functions found by DMFT and dual fermions, via the Maximum Entropy method [99] discussed in Chapter 2. The spectral function is related to the real frequency Green's function by $A(\omega) = -\frac{1}{\pi} ImG(\omega)$. In the case of DMFT we obtain only the local Green's function, which can be analytically continued as is. Dual fermions instead results in a momentum dependent Green's function, $G(i\omega_n, k)$, and so it must be integrated over k to obtain the local dual fermions Green's function.

$$
\begin{aligned}
A^{DMFT}(\omega) &= -\frac{1}{\pi} Im \left(MEM \left[G^{DMFT}(i\omega_n) \right] \right) \\
A^{DF}(\omega) &= -\frac{1}{\pi} Im \left(MEM \left[\frac{1}{N_k} \sum_k G^{DF}(i\omega_n, k) \right] \right)
\end{aligned}
\tag{5.33}
$$

Where MEM stands for the Maximum Entropy Method analytic continuation procedure. Fig. 5.4 shows that while a gap begins to open in both the DMFT and DF cases, it forms at much lower U in the DF case. Note also that as spectral weight is removed from $\omega = 0$, it shifts to two "Hubbard bands" above and below the Fermi surface [36]. The 'model' curve in this plot indicates the default model used during the MEM method.

One of the exciting features of dual fermions is its ability to provide data with arbitrary momentum space resolution. In contrast to cluster DMFT methods, such as DCA, that only produce Green's functions at a small set of cluster momenta, K, dual fermions enables one to study the behavior of Green's functions and spectral functions throughout the Brillouin zone. This can be advantageous for studying systems in which the physics is heavily momentum dependent, such as those with k dependent electronic gaps, and for comparing simulations directly to the experimental data produced by techniques, such as ARPES, that directly probe the energy and momentum dependent distribution of electronic states [131].

An example of what can be done with this ability is shown in Figures 5.5 and 5.6, in which two views of the evolution of the bandstructure versus temperature for the $U = 3t$ Hubbard model. By increasing the number of momentum space points, N_k, we can obtain the momentum resolved Green's function, $G(i\omega_n, k)$, and therefore the momentum resolved spectral function, $A(\omega, k)$, with arbitrary resolution. In this case we use $N_k = 32 \times 32$, and by plotting slices of the spectral function along a high symmetry cut through the Brillouin zone we can obtain a smooth bandstructure that allows us to see the formation of momentum dependent structure as we lower the temperature.

From the spectral function plots the most interesting feature is the band-splitting that occurs around $k = (0, 0)$ and $k = (\pi, \pi)$, which are far away from the Fermi surface, $\omega = 0$. In addition, Fig. 5.6 reveals the formation of an entirely new, but very weak, band that mirrors the original one. Hints of the formation of these structures can be seen by observing the behavior of the real frequency self-energy, $\Sigma(\omega, k)$. In

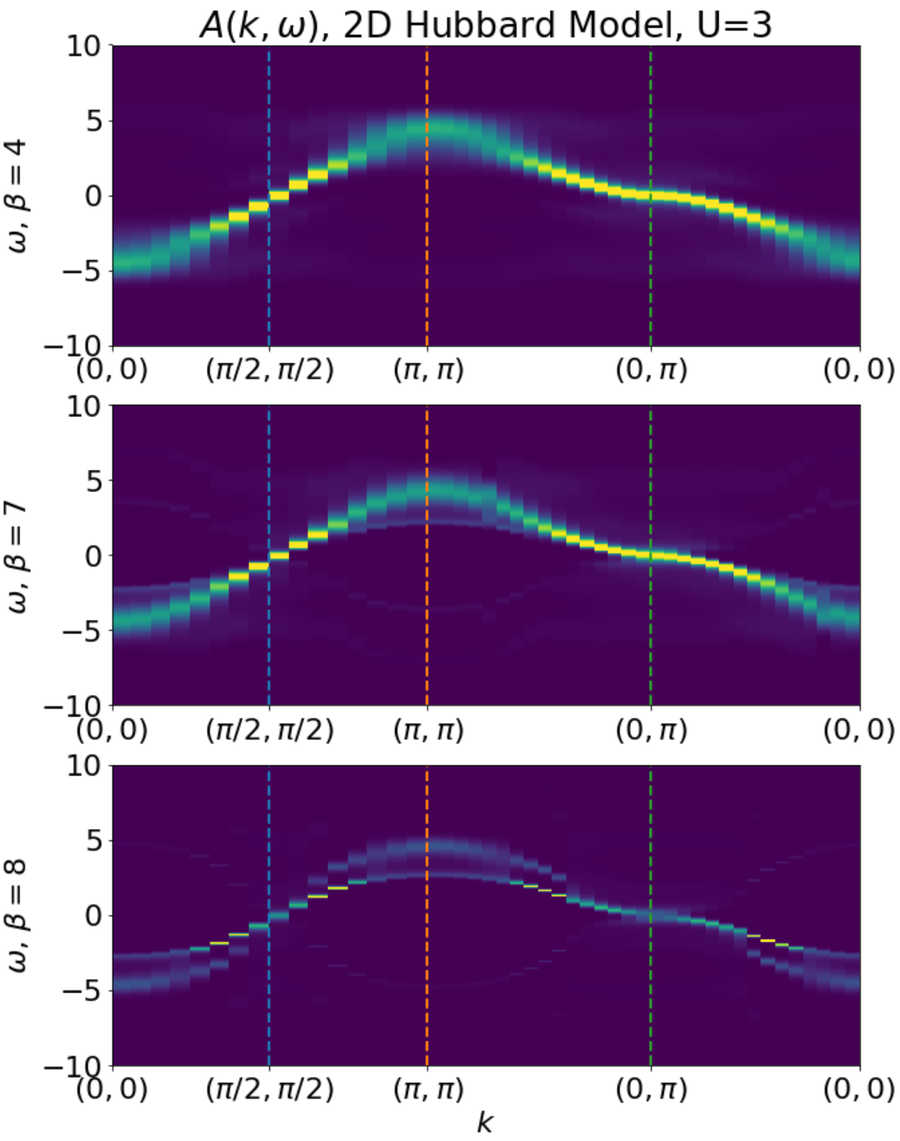

Figure 5.5: Band structure of the $U = 3t$ 2D Hubbard model versus temperature, $\beta = 1/T$, along a high symmetry cut through the Brillouin zone. Obtained from analytic continuation of the dual fermions Green's function to obtain the spectral function, $A(k,\omega)$. Lowering the temperature results in band splitting away from the Fermi surface, $\omega = 0$.

both the real and imaginary parts of the self-energy, we can see the formation of an X-like structure centered on the $\Sigma = (\pi/2, \pi/2)$ and $X = (0, \pi)$ that roughly follows the shape of both the band splitting and the weak new band.

We can also track how the number of states at the Fermi surface, $\omega = 0$, changes by plotting cuts of the spectral function. Fig. 5.8 depicts the such a cut from the

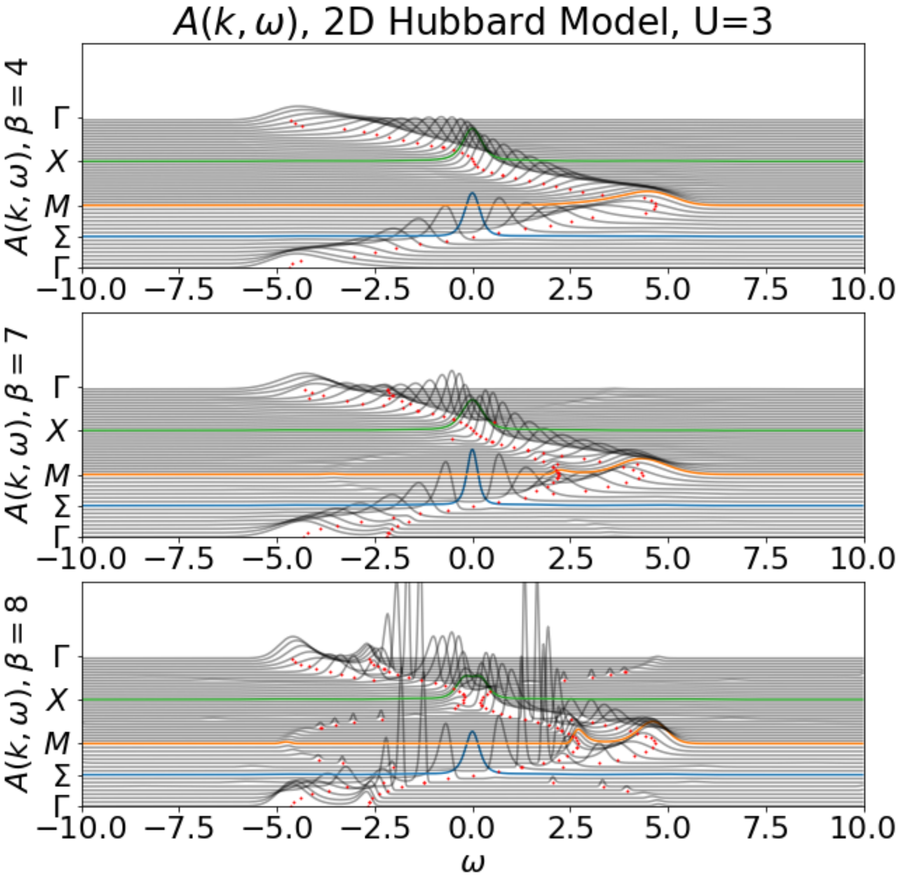

Figure 5.6: Spectral function of the $U = 3t$ Hubbard model at half-filling as a function of temperature. The bandstructure can be mapped by tracing the peaks in the spectral function. From this data we can see that as the temperature is lowered, the main band is split at the Γ and M points, and a much weaker band appears the mirrors the original band.

nodal ($k = (0, \pi)$) to antinodal ($k = (\pi/2, \pi/2)$) points. This data indicates that as the temperature is lowered, a momentum dependent gap begins to open at the nodal point.

This data can be supported by Matsubara frequency data, particularly the Matsubara self-energy, $\Sigma(i\omega_n, k$. Although less physically intuitive, this data is free from the complications and ambiguities that arise from the analytic continuation used to obtain the spectral functions. A general criteria that is used to characterize a state based on the Matsubara self-energy is to examine the behavior of the imaginary part near $\omega_n = 0$. When this quantity goes to zero we can characterize the state as metallic, whereas a down turn in the self-energy signals insulating behavior. Since

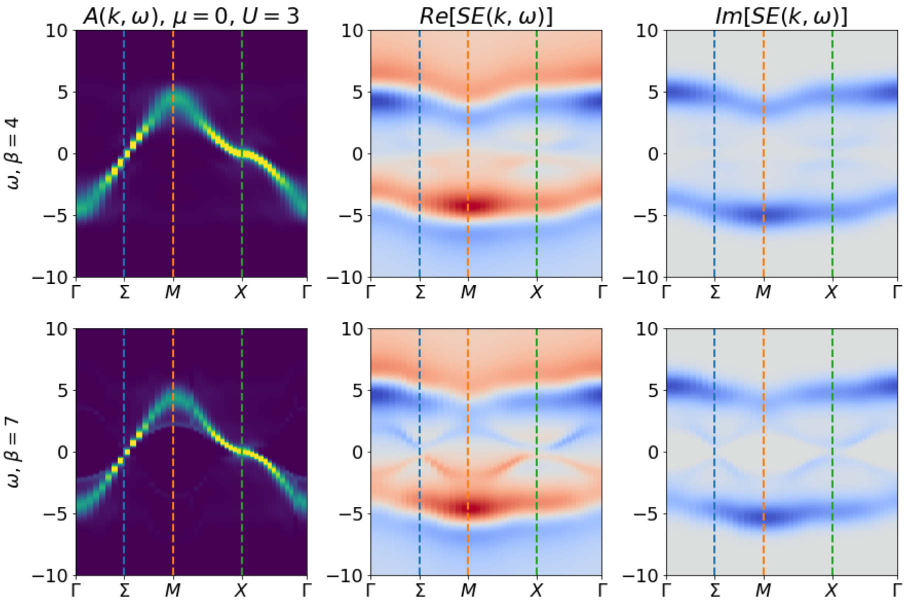

Figure 5.7: Comparison of the evolution of the spectral function and the real frequency self-energy along a high symmetry cut in momentum space. As the temperature is lowered a splitting of the energy band is observed concurrently with the formation of structure in the self-energy.

we only have access to the discrete Matsubara points, $\omega_n = \frac{(2n+1)\pi}{\beta}$, we can compare the lowest two Matsubara frequencies - when $Im\Sigma(i\omega_0) > Im\Sigma(i\omega_1)$ we have a Fermi liquid, or metallic state, whereas when $Im\Sigma(i\omega_0) < Im\Sigma(i\omega_1)$ we have an insulating, or at least non-Fermi liquid like state [3].

Figures 5.9 and 5.10 show the behavior of the Matsubara self-energy for the $U = 3t$ Hubbard model at half-filling, as obtained from dual fermions. From Fig. 5.10 we see that as the temperature is lowered the $k = (0,\pi)$ point is the first for which $Im\Sigma(i\omega_0) < Im\Sigma(i\omega_1)$. Fig. 5.9 shows in the detail the imaginary part of the self-energy at the nodal, anti-nodal, and intermediate momentum points. This Matsubara data thus agrees with the real frequency spectra in predicting that the nodal point becomes insulating first, indicating a momentum dependent metal insulator transition.

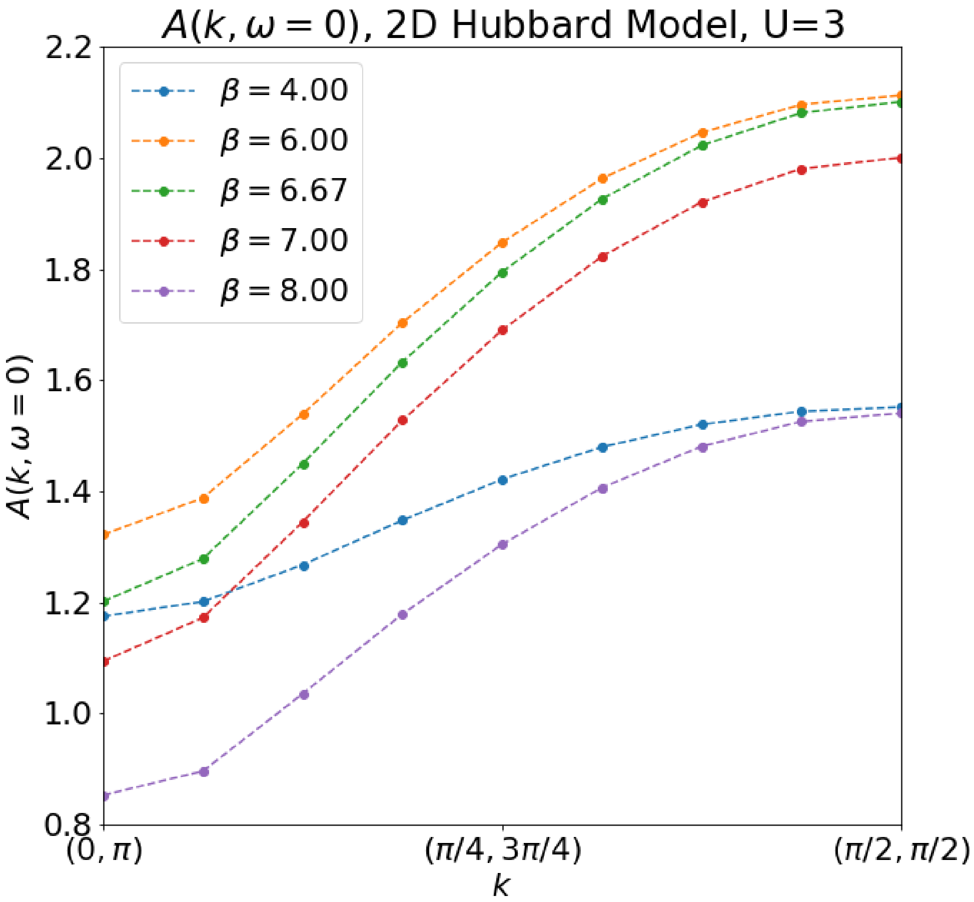

Figure 5.8: Change in the spectral function along momentum space cut between the nodal and anti-nodal points. At lower temperatures we see a momentum dependent reduction in the available electronic states, with an insulating gap beginning to form first at $k = (0, \pi)$.

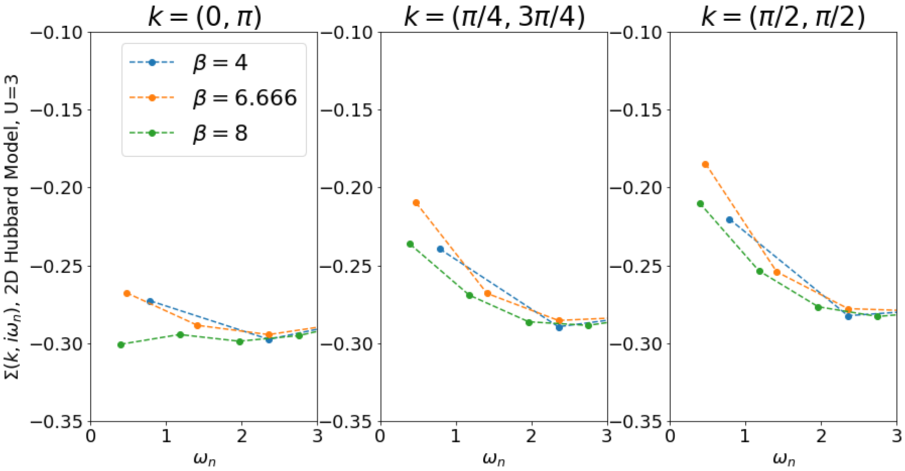

Figure 5.9: Matsubara self-energy at momentum points along a line from the nodal to anti-nodal points. A positive slope in the self-energy at small Matsubara frequencies indicates the formation of an insulator. This data indicates that as the temperature is lowered, the $k = (0, \pi)$ point is the first area of the Brillouin zone to become insulating.

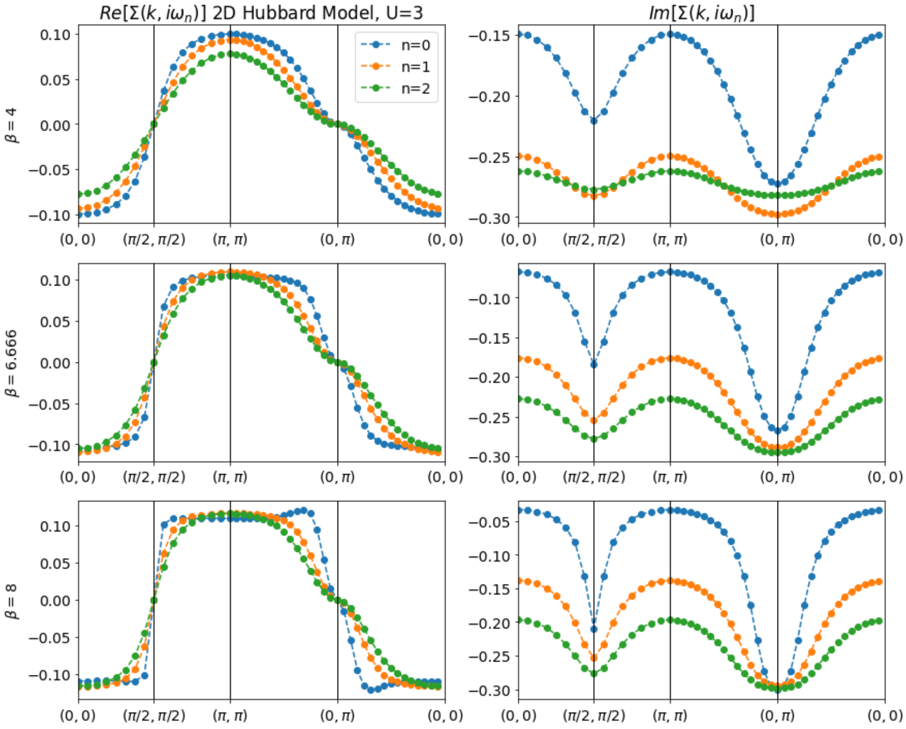

Figure 5.10: Behavior of the first three Matsubara frequency points of the self-energy through a high symmetry cut of momentum space. Insulating behavior is marked by $Im\Sigma(k, i\omega_0) < Im\Sigma(k, i\omega_1)$.

Full access to the Brillouin zone also allows us to study how the global structure of the Fermi surface evolves, as well as track quantities along the entire Fermi surface, such as the renormalized mass. Fig. 5.11 shows a series of $\omega = 0$ cuts of the spectral function, $A(\omega, k)$, which tells us where the states that make up the Fermi surface reside in momentum space. This data is obtained from $N_k = 64 \times 64$ dual fermions calculations, followed by an interpolation routine to smooth out the results. We can see that as the chemical potential is increased the Fermi surface smoothly transitions from electron-like to hole-like for smaller interaction strengths, U. At $U = 8$ however, we see an intermediate regime around half-filling where the Fermi surfaces seems to be composed of arcs, due to the momentum dependent insulating behavior that arises near the $k = (0, \pi)$ points.

In Matsubara space the ratio between the renormalized mass, $m^*(k)$, and the base electron mass, m, is given by the low frequency behavior of the self-energy. It is also related to the quasiparticle weight, Z_k, as follows [3, 182].

$$\frac{m^*(k)}{m} = Z_k^{-1} = 1 - \frac{\partial Im\Sigma(i\omega_n, k)}{\partial \omega_n}|_{\omega_n \to 0} \tag{5.34}$$

The final figure, Fig. 5.12, shows how the renormalized mass, evaluated along the Fermi surface, changes along the same U and μ values. Shown are the values of the renormalized mass ratio along a path in momentum space that traces the Fermi surface from the point $k = (0, \pi)$ to $k = (\pi, 0)$. We see that the renormalized mass is large and significantly momentum dependent at larger interaction strengths near half-filling, and that it tends to be larger near the $k = (0, \pi)$ (nodal) point than the $k = (\pi/2, \pi/2)$ (anti-nodal) point.

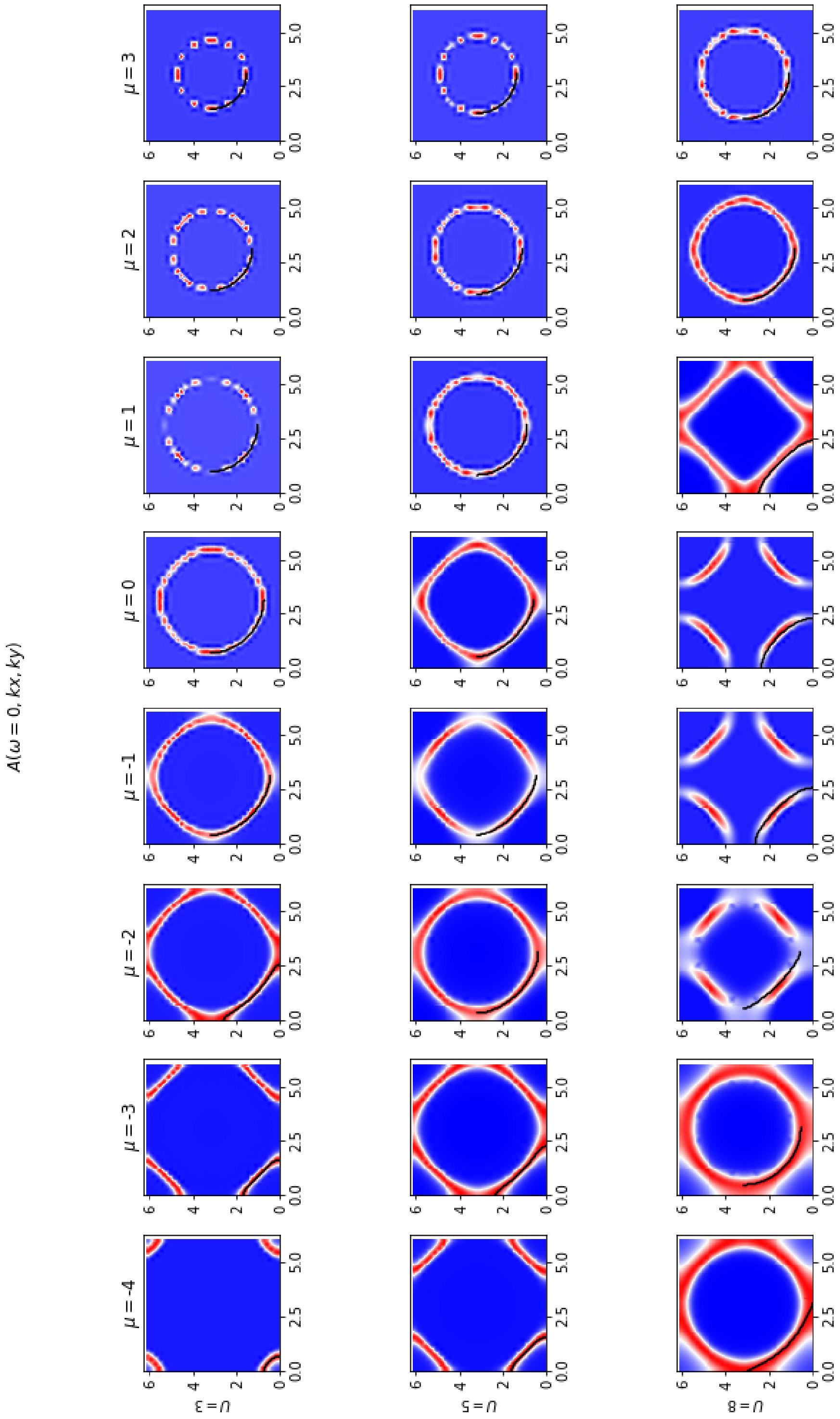

Figure 5.11: Evolution of the Fermi surface, $A(k, \omega = 0)$, as a function of interaction strength, U, and chemical potential, μ.

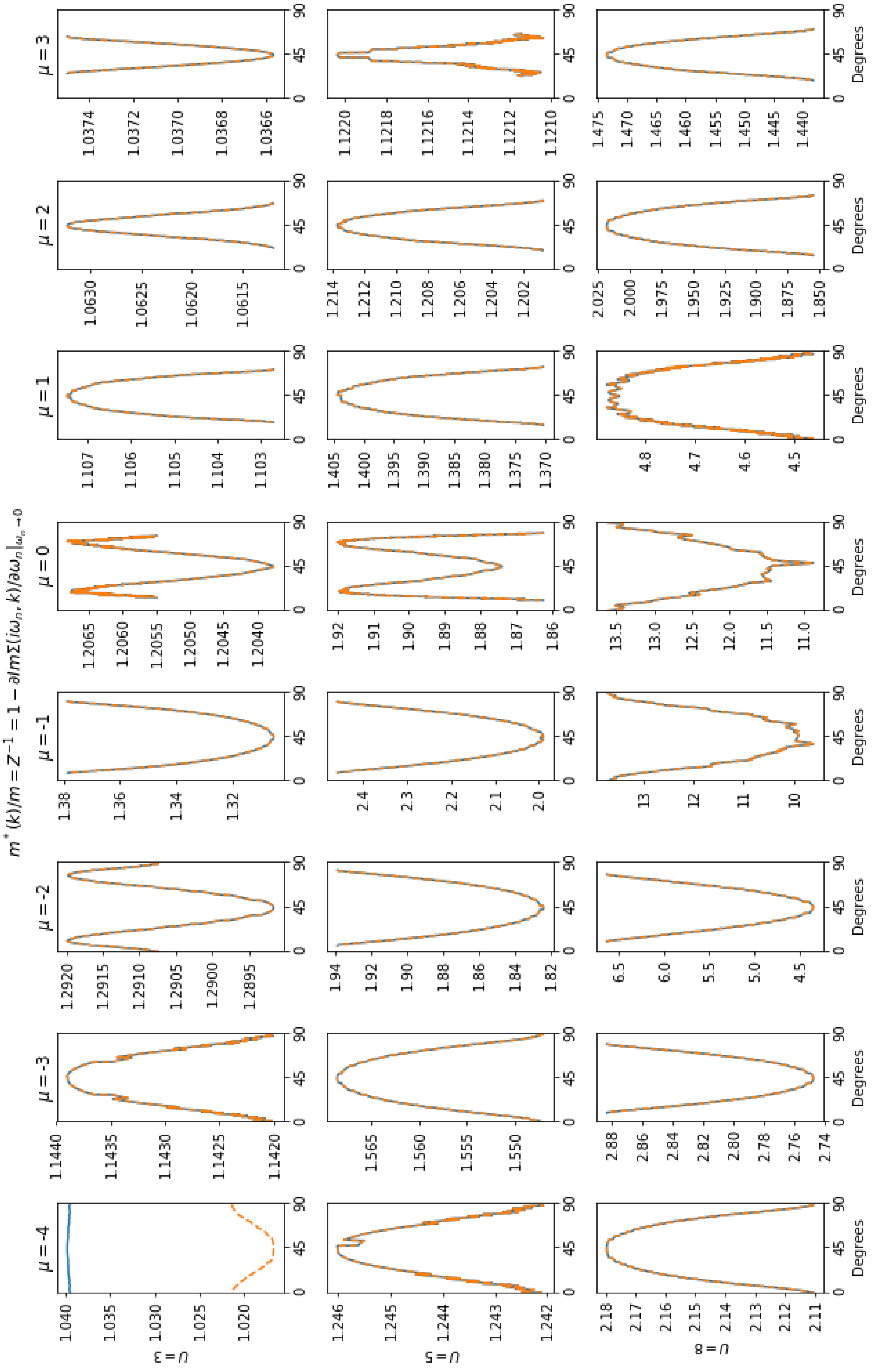

Figure 5.12: The renormalized mass obtained from the Matsubara self-energy along the Fermi surface, from the $k = (0, \pi)$ to $k = (\pi, 0)$ points.

Chapter 6

Conclusion

This thesis described several attempts to enhance our ability to study the physics of the 2D Hubbard model and its extensions. Although the Hubbard model represents a dramatic simplification of real materials, it remains an important arena for understanding strongly correlated electron physics due to its complex phase diagram and an display of strongly correlated phenomena known to occur in nature, such as the Mott transition and superconductivity.

Chapter 1 provided a high-level overview of strongly correlated phenomena, i.e. physical properties of certain materials that cannot be understood within an independent quasi-particle picture or perturbative techniques. Chapter 2 provided background on many of the theories and numerical techniques used throughout the work, including the Dynamical Mean Field Theory, the Dynamical Cluster Approximation, Quantum Monte Carlo methods and the Continuous Time Auxiliary Field algorithm, and the Maximum Entropy Method for numerical analytic continuation.

Chapter 3 described work to suppress the severe finite size effects that arise in simulating the Hubbard model with DCA. We presented Twisted Boundary Conditions as a potential method for decreasing these finite size errors by averaging quantities obtained for a single cluster size over boundary conditions. This may allow us to delay the challenges posed by algorithmic scaling and the fermion sign problem by obtaining large cluster results from simulations on small clusters. We presented detailed derivations and descriptions for how TBC can be implemented with Betts clusters and how the DCA numerical algorithms are modified. We also presented results obtained by implementing TBC with exact diagonalization, second order perturbation theory, and DMFT with a modified Continuous Time Auxiliary

Field impurity solver. Future work in this direction is to quantify the extent to which TBC can help extrapolate finite size simulation results to infinite system sizes.

Chapter 4 presented methods and results for studying the 2D Extended Hubbard Model on a square lattice, which adds in non-local density interactions, V, that model the non-local nature of the Coulomb interaction. We described how to perform QMC simulations on this system as well as how to extend submatrix updates to make spin flip updates more efficient. We presented a detailed study of the phase diagrams and energetics of the charge order transition away from half-filling. We also presented results on the phase boundaries between the paramagnetic metallic state and the insulating antiferromagnetic state, as well as between the antiferromagnetic and charge order states, at half-filling. We found hysteresis along the antiferromagnet/charge order and normal/charge order phase boundaries, indicating first order phase transitions. We showed that nearest neighbor interactions lower the critical temperature for the antiferromagnetic phase transition. Finally, we demonstrated the effect of nearest neighbor interactions on the antiferromagnetic phase boundary and for the evolution of spectral functions and energetics across the phase transitions. An potentially interesting extension of this work would be to more closely study how the transition between normal and charge ordered states changes as the local interaction strength, U, is increased.

Chapter 5 contained a discussion and pedagogical derivation on the Dual Fermions technique, a diagrammatic expansion about the single site impurity problems used in techniques such as DMFT. This method perturbatively re-introduces non-local correlations and provides a numerically cheap method of obtaining high resolution momentum space information, especially compared to cluster methods such as DCA. We presented the Dual Fermions Ladder Approximation and saw how the method both corrects the results from single-site DMFT and provides the ability to study how quantities, such as the spectral function, behave throughout momentum space. We presented results on the momentum dependent shift in the spectral function along the Fermi surface as the metal-insulator transition is approached, as well as the evolution of the entire band structure and momentum dependent mass renormalization versus temperature and chemical doping. This work demonstrates some of the new information that can be obtained from numerical simulations based on the DMFT, but more thought is required to identify interesting specific systems or physical observables to study and compare to experiments.

Appendix A

Calculating Energies

The outputs of DMFT are generally greens functions, $G_\sigma(k, i\omega_n)$, and self-energies, $\Sigma_\sigma(k, i\omega_n)$, in momentum and Matsubara space. From these outputs, we would like to be able to calculate various observables, the most obvious being the energy of the system.

The energy per site is given by the expectation value of the Hamiltonian, which in our case is given by the Hubbard Hamiltonian.

$$E = \langle H \rangle \tag{A.1}$$

$$H = \sum_{k\sigma} \left(\epsilon(k) - \mu\right) c^\dagger_{k\sigma} c_{k\sigma} + U \sum_i \left(n_{i\uparrow} - \frac{1}{2}\right)\left(n_{i\downarrow} - \frac{1}{2}\right) \tag{A.2}$$

We can split the total energy into kinetic and potential energies as follows.

$$E = E_K + E_V \tag{A.3}$$

$$E_K = \left\langle \sum_{k\sigma} \left(\epsilon(k) - \mu\right) c^\dagger_{k\sigma} c_{k\sigma} \right\rangle \tag{A.4}$$

$$E_V = \left\langle U \sum_i \left(n_{i\uparrow} - \frac{1}{2}\right)\left(n_{i\downarrow} - \frac{1}{2}\right) \right\rangle \tag{A.5}$$

We would like to write these formulas in terms of $G_\sigma(k, i\omega_n)$ and $\Sigma_\sigma(k, i\omega_n)$. Begin by rearranging the expressions, noting that $G^{-1}_\sigma(k, i\omega_n) = i\omega_n - \epsilon(k) + \mu - \Sigma_\sigma(k, i\omega_n)$, and using translational invariance.

$$
\begin{aligned}
E_K &= \sum_{k\sigma} (\epsilon(k) - \mu) \left\langle c_{k\sigma}^{\dagger} c_{k\sigma} \right\rangle \\
&= \sum_{k\sigma} (\epsilon(k) - \mu) \langle n_{k\sigma} \rangle \\
&= \sum_{k\sigma} \big(i\omega_n - \Sigma_\sigma(k, i\omega_n) - G_\sigma^{-1}(k, i\omega_n) \big) \langle n_{k\sigma} \rangle
\end{aligned}
\tag{A.6}
$$

$$
\begin{aligned}
E_V &= \left\langle U \sum_i \left(n_{i\uparrow} n_{i\downarrow} - \frac{1}{2} n_{i\uparrow} - \frac{1}{2} n_{i\downarrow} + \frac{1}{4} \right) \right\rangle \\
&= \frac{UN}{4} - \frac{U}{2} \sum_{i\sigma} \langle n_{i\sigma} \rangle + U \sum_i \langle n_{i\uparrow} n_{i\downarrow} \rangle \\
&= \frac{UN}{4} - \frac{U}{2} \sum_{k\sigma} \langle n_{k\sigma} \rangle + U \sum_i \langle n_{i\uparrow} n_{i\downarrow} \rangle
\end{aligned}
\tag{A.7}
$$

So we really just need to express $\langle n_{k\sigma} \rangle$ and $\langle n_{i\uparrow} n_{i\downarrow} \rangle$ in terms of $G_\sigma(k, i\omega_n)$ and $\Sigma_\sigma(k, i\omega_n)$. The expectation value of the density is the easier value to calculate. Starting with the definition of the Greens function in imaginary time,

$$
G_\sigma(k, \tau) = -\left\langle T_\tau c_{k\sigma}(\tau) c_{k\sigma}^{\dagger}(0) \right\rangle \tag{A.8}
$$

$$
G_\sigma(k, \tau + \beta) = -G_\sigma(k, \tau) \tag{A.9}
$$

$$
G_\sigma(k, \tau) = \frac{1}{\beta} \sum_n G_\sigma(k, i\omega_n) e^{-i\omega_n \tau} \tag{A.10}
$$

We can calculate

$$\begin{aligned}\langle n_{k\sigma}\rangle &= \left\langle c^{\dagger}_{k\sigma} c_{k\sigma} \right\rangle \\ &= \left\langle c^{\dagger}_{k\sigma}(0) c_{k\sigma}(\tau = 0^{-}) \right\rangle \\ &= -\left\langle T_{\tau} c_{k\sigma}(\tau = 0^{-}) c^{\dagger}_{k\sigma}(0) \right\rangle \\ &= G_{\sigma}(k, \tau \to 0^{-}) \\ &= \frac{1}{\beta} \sum_{n} G_{\sigma}(k, i\omega_n) e^{i\omega_n 0^{+}} \\ &= \frac{1}{\beta} \sum_{n} G_{\sigma}(k, i\omega_n)\end{aligned} \tag{A.11}$$

In order to write $\langle n_{i\uparrow} n_{i\downarrow}\rangle$ in terms of $G_{\sigma}(k, i\omega_n)$ and $\Sigma_{\sigma}(k, i\omega_n)$, we make use of two identities (that you can find in Coleman),

$$\sum_{k\sigma} c^{\dagger}_{k\sigma} \left[H_0, c_{k\sigma}\right] = -H_0 \tag{A.12}$$

$$-2V = \sum_{k\sigma} c^{\dagger}_{k\sigma} \left[V, c_{k\sigma}\right] \tag{A.13}$$

Where H_0 is the non-interacting part of the Hamiltonian and V is a general interaction of the form

$$V = \sum_{k_1 k_2 k_3 k_4} V(k_1, k_2, k_3, k_4) c^{\dagger}_{k_1} c^{\dagger}_{k_2} c_{k_3} c_{k_4} \tag{A.14}$$

where the k_i indices stand for all relevant state indices, i.e. momentum and spin. We also use the equation of motion for an operator O,

$$\frac{\partial O}{\partial \tau} = [H, O] \tag{A.15}$$

In our case,

$$V = \sum_{i} n_{i\uparrow} n_{i\downarrow} = H - H_0 - \frac{UN}{4} + \frac{U}{2} \sum_{k\sigma} n_{k\sigma} \tag{A.16}$$

$$
\begin{aligned}
H_0 &= \sum_{k\sigma} \big(i\omega_n - \Sigma_\sigma(k,i\omega_n) - G_\sigma^{-1}(k,i\omega_n)\big)\, n_{k\sigma} \\
&= \frac{1}{\beta}\sum_{nk\sigma} \left[-1e^{i\omega_n 0^+} + (i\omega_n - \Sigma_\sigma(k,i\omega_n))\, G_\sigma(k,i\omega_n) e^{i\omega_n 0^+}\right]
\end{aligned}
\tag{A.17}
$$

So,

$$
\begin{aligned}
\left\langle \sum_i n_{i\uparrow} n_{i\downarrow} \right\rangle &= \langle V \rangle \\
&= \left\langle -\frac{1}{2}\sum_{k\sigma} c^\dagger_{k\sigma}\left[\sum_i n_{i\uparrow}n_{i\downarrow}, c_{k\sigma}\right]\right\rangle \\
&= \frac{-1}{2}\sum_{k\sigma}\left\langle c^\dagger_{k\sigma}\left[H - H_0 - \frac{UN}{4} + \frac{U}{2}\sum_{k\sigma} n_{k\sigma}, c_{k\sigma}\right]\right\rangle \\
&= \frac{-1}{2}\sum_{k\sigma}\left\langle c^\dagger_{k\sigma}\left[H, c_{k\sigma}\right]\right\rangle - \left\langle c^\dagger_{k\sigma}\left[H_0, c_{k\sigma}\right]\right\rangle + \frac{U}{2}\left\langle c^\dagger_{k\sigma}\left[\sum_{k\sigma} n_{k\sigma}, c_{k\sigma}\right]\right\rangle \\
&= -\frac{1}{2}\left(\sum_{k\sigma}\left[\left(\frac{\partial G_\sigma(k,\tau)}{\partial\tau}\right)_{\tau\to 0^-} - \frac{U}{2}\langle n_{k\sigma}\rangle\right] + H_0\right) \\
&= -\frac{1}{2}\sum_{nk\sigma}\left[\frac{-i\omega_n}{\beta} G_\sigma(k,i\omega_n) e^{i\omega_n 0^+} - \frac{U}{2\beta} G_\sigma(k,i\omega_n) e^{i\omega_n 0^+}\right] \\
&+ -\frac{1}{2\beta}\sum_{nk\sigma}\left[-1e^{i\omega_n 0^+} + (i\omega_n - \Sigma_\sigma(k,i\omega_n))\, G_\sigma(k,i\omega_n) e^{i\omega_n 0^+}\right] \\
&= \frac{1}{2\beta}\sum_{nk\sigma}\Sigma_\sigma(k,i\omega_n) G_\sigma(k,i\omega_n) + \frac{U}{4\beta}\sum_{nk\sigma} G_\sigma(k,i\omega_n)
\end{aligned}
\tag{A.18}
$$

Where we used that

$$
\frac{1}{\beta}\sum_n e^{i\omega_n 0^+} = -\frac{1}{2\pi i}\int dz \frac{e^{z0^+}}{e^{\beta z}+1} \tag{A.19}
$$

By the residue theorem, with a contour that encompasses the poles at $e^{\beta z} = -1$, $\beta z = i(2n+1)\pi$, $z = i(2n+1)/\beta = i\omega_n$, along the imaginary axis. If we reverse the direction of the contour, we would instead pick up the poles outside of this contour, those belonging to e^{z0^+}. But this function has no poles, and thus no residues. So,

$$\frac{1}{\beta}\sum_{n} e^{i\omega_n 0^+} = 0 \tag{A.20}$$

Our final results for the energy in terms of $G_\sigma(k, i\omega_n) and \Sigma_\sigma(k, i\omega_n)$ are then:

$$E = E_K + E_V \tag{A.21}$$

$$E_K = \frac{1}{\beta}\sum_{nk\sigma} \left[-1 + \left(i\omega_n - \Sigma_\sigma(k, i\omega_n)\right) G_\sigma(k, i\omega_n)\right] \tag{A.22}$$

$$\begin{aligned} E_V &= \frac{UN}{4} - \frac{U}{2\beta}\sum_{nk\sigma} G_\sigma(k, i\omega_n) + \frac{1}{2\beta}\sum_{nk\sigma} \Sigma_\sigma(k, i\omega_n) G_\sigma(k, i\omega_n) + \frac{U}{4\beta}\sum_{nk\sigma} G_\sigma(k, i\omega_n) \\ &= \frac{UN}{4} - \frac{U}{4\beta}\sum_{nk\sigma} G_\sigma(k, i\omega_n) + \frac{1}{2\beta}\sum_{nk\sigma} \Sigma_\sigma(k, i\omega_n) G_\sigma(k, i\omega_n) \end{aligned} \tag{A.23}$$

The energy should be a real valued quantity, and one can check that the above formulas satisfy this constraint by using that

$$G^*(i\omega_n) = G(-i\omega_n) \tag{A.24}$$

$$\Sigma^*(i\omega_n) = \Sigma(-i\omega_n) \tag{A.25}$$

Since the frequency sums kill any terms that have odd frequency parity, only certain combinations of real ($\Re$) and imaginary ($\Im$) parts survive.

$$E_K = \frac{2}{\beta}\sum_{n\geq 0, k\sigma} \left[-1 - \Re\Sigma\Re G - \omega_n \Im G + \Im\Sigma\Im G\right] \tag{A.26}$$

$$E_V = \frac{UN}{4} - \frac{2U}{4\beta}\sum_{n\geq 0, k\sigma} \Re G + \frac{2}{2\beta}\sum_{n\geq 0, k\sigma} \left(\Re\Sigma\Re G - \Im\Sigma\Im G\right) \tag{A.27}$$

So there are really three terms that we need to compute

$$I_1 = 2\sum_{n\geq 0, k\sigma} \left[-1 - \omega_n \Im G\right] \tag{A.28}$$

$$I_2 = 2 \sum_{n \geq 0, k\sigma} (\Re\Sigma\Re G - \Im\Sigma\Im G) \tag{A.29}$$

$$I_3 = 2 \sum_{n \geq 0, k\sigma} \Re G \tag{A.30}$$

So,

$$E_K = \frac{I_1}{\beta} - \frac{I_2}{\beta} \tag{A.31}$$

$$E_V = \frac{UN}{4} - \frac{U}{4\beta} I_3 + \frac{1}{2\beta} I_2 \tag{A.32}$$

Appendix B

High Frequency Tails

The above formulas tell us how to calculate the energy theoretically, but on a computer we cannot actually do the full summation over Matsubara frequencies. The stored greens functions and self-energies are always truncated at some maximum frequency, $i\omega_{n_m}$. We cannot simply truncate the sum, however, because these functions decay slowly as a function of $i\omega_n$ due to the discontinuity in $G_\sigma(k,\tau)$ at $\tau = 0$.

We solve this problem by utilizing analytic high frequency tails for $G_\sigma(k, i\omega_n)$ and $\Sigma_\sigma(k, i\omega_n)$, [105]

$$\Sigma_\sigma^{tail}(k, i\omega_n) = \Sigma_\sigma^0(k) + \frac{\Sigma_\sigma^0(k)}{i\omega_n} + \mathcal{O}\left(\frac{1}{(i\omega_n)^2}\right) \tag{B.1}$$

$$G_\sigma^{tail}(k, i\omega_n) = \frac{c_\sigma^1(k)}{i\omega_n} + \frac{c_\sigma^2(k)}{(i\omega_n)^2} + \frac{c_\sigma^3(k)}{(i\omega_n)^3} + \mathcal{O}\left(\frac{1}{(i\omega_n)^4}\right) \tag{B.2}$$

The coefficients in these expansions can be calculated by hand (though it is tedious, see Emanuel's thesis for details), and are computed during the DMFT program and stored with the GFTools greens functions. In the following, we explicitly use that $c_\sigma^1(k) = 1$.

The tails enable us to write the frequency sums as

$$\sum_n f(i\omega_n) = \sum_{n \le n_m} f(i\omega_n) + \sum_{n > n_m} f^{tail}(i\omega_n) \tag{B.3}$$

The energy terms can now be written as (suppressing momentum and spin, and only keeping up to order $1/\omega_n^2$ terms)

$$\begin{aligned}
I_1 &= 2\sum_{n_m \geq n \geq 0}\left[-1-\omega_n \Im G\right] + 2\sum_{n>n_m}\left[-1-\omega_n \Im G^{tail}\right] \\
&= 2\sum_{n_m \geq n \geq 0}\left[-1-\omega_n \Im G\right] - 2\sum_{n>n_m}\frac{c_3}{\omega_n^2} \\
&= 2\sum_{n_m \geq n \geq 0}\left[-1-\omega_n \Im G\right] - 2c_3\Psi
\end{aligned} \tag{B.4}$$

$$\begin{aligned}
I_2 &= 2\sum_{n_m \geq n \geq 0}\left(\Re\Sigma\Re G - \Im\Sigma\Im G\right) + 2\sum_{n>n_m}\left(\Re\Sigma^{tail}\Re G^{tail} - \Im\Sigma^{tail}\Im G^{tail}\right) \\
&= 2\sum_{n_m \geq n \geq 0}\left(\Re\Sigma\Re G - \Im\Sigma\Im G\right) + 2\sum_{n>n_m}\left(\frac{-c^1\Sigma^1}{\omega_n^2} - \frac{\Sigma^0 c^2}{\omega_n^2}\right) \\
&= 2\sum_{n_m \geq n \geq 0}\left(\Re\Sigma\Re G - \Im\Sigma\Im G\right) + 2\left(-c^1\Sigma^1 - \Sigma^0 c^2\right)\Psi
\end{aligned} \tag{B.5}$$

$$\begin{aligned}
I_3 &= 2\sum_{n_m \geq n \geq 0}\Re G + 2\sum_{n>n_m}\Re G^{tail} \\
&= 2\sum_{n_m \geq n \geq 0}\Re G - 2\sum_{n>n_m}\frac{c_2}{\omega_n^2} \\
&= 2\sum_{n_m \geq n \geq 0}\Re G - 2c_2\Psi
\end{aligned} \tag{B.6}$$

Where

$$\begin{aligned}
\Psi &= \sum_{n>n_m}\frac{1}{\omega_n^2} \\
&= \frac{\beta^2}{\pi^2 4}\sum_{k=0}^{\infty}\frac{1}{\left(n_m+0.5+k\right)^2} \\
&= \frac{\beta^2}{\pi^2 4}\psi^{(1)}\left(n_m+0.5\right)
\end{aligned} \tag{B.7}$$

Where $\psi^{(n)}(x)$ is the digamma function, which can be computed with a GSL function call (gsl_sf_psi_n).

Bibliography

[1] J. Martin, *When condensed matter became king*, *Physics Today* **72** (January, 2019) 30.

[2] U. Rössler, *Solid state theory: an introduction.* Springer Science & Business Media, 2009.

[3] P. Coleman, *Introduction to Many-Body Physics.* Cambridge University Press, 2015.

[4] P. J. Ray, *Master's thesis: Structural investigation of la(2-x)sr(x)cuo(4+y) - following staging as a function of temperature.*, .

[5] J. Mitchell, D. Argyriou, A. Berger, K. Gray, R. Osborn, and U. Welp, *Spin, charge, and lattice states in layered magnetoresistive oxides*, .

[6] S. Nakatsuji and Y. Maeno, *Quasi-two-dimensional mott transition system ca 2- x sr x ruo 4*, *Physical review letters* **84** (2000), no. 12 2666.

[7] S. Nakatsuji, V. Dobrosavljević, D. Tanasković, M. Minakata, H. Fukazawa, and Y. Maeno, *Mechanism of hopping transport in disordered mott insulators*, *Physical review letters* **93** (2004), no. 14 146401.

[8] M. L. Foo, Y. Wang, S. Watauchi, H. Zandbergen, T. He, R. Cava, and N. Ong, *Charge ordering, commensurability, and metallicity in the phase diagram of the layered na x co o 2*, *Physical review letters* **92** (2004), no. 24 247001.

[9] P. Limelette, P. Wzietek, S. Florens, A. Georges, T. Costi, C. Pasquier, D. Jérome, C. Mézière, and P. Batail, *Mott transition and transport crossovers in the organic compound κ-(b e d t- t t f) 2 c u [n (c n) 2] c l*, *Physical review letters* **91** (2003), no. 1 016401.

[10] V. Sidorov, M. Nicklas, P. Pagliuso, J. Sarrao, Y. Bang, A. Balatsky, and J. Thompson, *Superconductivity and quantum criticality in c e c o i n 5*, *Physical review letters* **89** (2002), no. 15 157004.

[11] E. Dagotto, *Complexity in strongly correlated electronic systems*, *Science* **309** (Jul, 2005) 257–262.

[12] R. Comin, R. Sutarto, F. He, E. da Silva Neto, L. Chauviere, A. Frano, R. Liang, W. Hardy, D. Bonn, Y. Yoshida, et al., *Symmetry of charge order in cuprates*, *Nature materials* **14** (2015), no. 8 796.

[13] E. d. S. Neto, P. Aynajian, A. Frano, R. Comin, E. Schierle, E. Weschke, A. Gyenis, J. Wen, J. Schneeloch, Z. Xu, S. Ono, J. G. Gu, M. Le Tacon, and A. Yazdani, *Ubiquitous interplay between charge ordering and high-temperature superconductivity in cuprates*, *Science* **343** (01, 2014).

[14] T. Maier, M. Jarrell, T. Pruschke, and M. H. Hettler, *Quantum cluster theories*, *Rev. Mod. Phys.* **77** (Oct, 2005) 1027–1080.

[15] C. Lin, F. Zong, and D. Ceperley, *Twist-averaged boundary conditions in continuum quantum monte carlo algorithms*, *Physical Review E* **64** (2001), no. 1 016702.

[16] **Simons Collaboration on the Many-Electron Problem** Collaboration, J. P. F. LeBlanc, A. E. Antipov, F. Becca, I. W. Bulik, G. K.-L. Chan, C.-M. Chung, Y. Deng, M. Ferrero, T. M. Henderson, C. A. Jiménez-Hoyos, E. Kozik, X.-W. Liu, A. J. Millis, N. V. Prokof'ev, M. Qin, G. E. Scuseria, H. Shi, B. V. Svistunov, L. F. Tocchio, I. S. Tupitsyn, S. R. White, S. Zhang, B.-X. Zheng, Z. Zhu, and E. Gull, *Solutions of the two-dimensional hubbard model: Benchmarks and results from a wide range of numerical algorithms*, *Phys. Rev. X* **5** (Dec, 2015) 041041.

[17] H. Strand, *Many body theory vt 2010: Iterated perturbation theory and dynamical mean field theory*, .

[18] C. Gros, *Control of the finite-size corrections in exact diagonalization studies*, *Physical Review B* **53** (1996), no. 11 6865.

[19] **Simons Collaboration on the Many-Electron Problem** Collaboration, J. P. F. LeBlanc, A. E. Antipov, F. Becca, I. W. Bulik, G. K.-L. Chan, C.-M. Chung, Y. Deng, M. Ferrero, T. M. Henderson, C. A. Jiménez-Hoyos, E. Kozik, X.-W. Liu, A. J. Millis, N. V. Prokof'ev, M. Qin, G. E. Scuseria, H. Shi, B. V. Svistunov, L. F. Tocchio, I. S. Tupitsyn, S. R. White, S. Zhang, B.-X. Zheng, Z. Zhu, and E. Gull, *Solutions of the two-dimensional hubbard model: Benchmarks and results from a wide range of numerical algorithms*, *Phys. Rev. X* **5** (Dec, 2015) 041041.

[20] E. G. C. P. van Loon, A. I. Lichtenstein, M. I. Katsnelson, O. Parcollet, and H. Hafermann, *Beyond extended dynamical mean-field theory: Dual boson approach to the two-dimensional extended hubbard model*, *Phys. Rev. B* **90** (Dec, 2014) 235135.

[21] T. Ayral, S. Biermann, and P. Werner, *Screening and nonlocal correlations in the extended hubbard model from self-consistent combined gw and dynamical mean field theory*, *Phys. Rev. B* **87** (Mar, 2013) 125149.

[22] R. A. Bari, *Effects of short-range interactions on electron-charge ordering and lattice distortions in the localized state*, *Phys. Rev. B* **3** (Apr, 1971) 2662–2670.

[23] H. Terletska, T. Chen, and E. Gull, *Charge ordering and correlation effects in the extended hubbard model*, *Phys. Rev. B* **95** (Mar, 2017) 115149.

[24] E. Gull, A. J. Millis, A. I. Lichtenstein, A. N. Rubtsov, M. Troyer, and P. Werner, *Continuous-time monte carlo methods for quantum impurity models*, *Rev. Mod. Phys.* **83** (May, 2011) 349–404.

[25] E. Gull, P. Staar, S. Fuchs, P. Nukala, M. S. Summers, T. Pruschke, T. C. Schulthess, and T. Maier, *Submatrix updates for the continuous-time auxiliary-field algorithm*, *Phys. Rev. B* **83** (Feb, 2011) 075122.

[26] D. Natelson, *Commentary: Condensed matters image problem*, *Physics Today* (December, 2018).

[27] J. Martin, *Solid State Insurrection: How the Science of Substance Made American Physics Matter.* University of Pittsburgh Press, 2018.

[28] J. T. S. W. Z. W. Lillian Hoddeson, Ernest Braun, *Out of the crystal maze: Chapters from the history of solidstate physics*, *American Journal of Physics* (1993).

[29] D. S. Abraham, *The Elements of Power Gadgets, Guns, and the Struggle for a Sustainable Future in the Rare Metal Age.* Yale University Press, 2015.

[30] J. D. Martin, *Prestige asymmetry in american physics: Aspirations, applications, and the purloined letter effect*, *Science in Context* **30** (2017), no. 4 475506.

[31] S. N. Patrick J. Mulvey, *Trends in physics phds*, .

[32] R. M. Martin, L. Reining, and D. M. Ceperley, *Interacting Electrons: Theory and Computational Approaches.* Cambridge University Press, 2016.

[33] J. Negele, *Quantum Many-particle Systems.* CRC Press, 2018.

[34] P. Nozieres, *Theory of Interacting Fermi Systems.* Addison-Wesley, 1964.

[35] N. Ashcroft and N. Mermin, *Solid state physics (brooks cole, 1976)*, *Cited on* **45** (1993).

[36] G. Kotliar and D. Vollhardt, *Strongly Correlated Materials: Insights From Dynamical Mean-Field Theory*, *Physics Today* **57** (Mar., 2004) 53–59.

[37] W. Kohn and L. J. Sham, *Self-consistent equations including exchange and correlation effects*, *Physical review* **140** (1965), no. 4A A1133.

[38] R. M. Martin, *Electronic structure: basic theory and practical methods.* Cambridge university press, 2004.

[39] R. O. Jones, *Density functional theory: Its origins, rise to prominence, and future*, *Rev. Mod. Phys.* **87** (Aug, 2015) 897–923.

[40] V. Antonov, L. Bekenov, and A. Yaresko, *Electronic structure of strongly correlated systems*, *Advances in Condensed Matter Physics* **2011** (2011).

[41] D. Vollhardt, *Dynamical meanfield theory of electronic correlations in models and materials*, *AIP Conference Proceedings* **1297** (2010), no. 1 339–403, [https://aip.scitation.org/doi/pdf/10.1063/1.3518901].

[42] P. A. Lee, N. Nagaosa, and X.-G. Wen, *Doping a mott insulator: Physics of high-temperature superconductivity*, *Rev. Mod. Phys.* **78** (Jan, 2006) 17–85.

[43] Q. Si and F. Steglich, *Heavy fermions and quantum phase transitions*, *Science* **329** (2010), no. 5996 1161–1166.

[44] K. T. Moore and G. van der Laan, *Nature of the* $5f$ *states in actinide metals*, *Rev. Mod. Phys.* **81** (Feb, 2009) 235–298.

[45] D. C. Johnston, *The puzzle of high temperature superconductivity in layered iron pnictides and chalcogenides*, *Advances in Physics* **59** (2010), no. 6 803–1061.

[46] T. Timusk and B. Statt, *The pseudogap in high-temperature superconductors: an experimental survey*, *Reports on Progress in Physics* **62** (jan, 1999) 61–122.

[47] M. Imada, A. Fujimori, and Y. Tokura, *Metal-insulator transitions*, *Rev. Mod. Phys.* **70** (Oct, 1998) 1039–1263.

[48] A. Millis, *Towards a classification of the effects of disorder on materials properties*, *Solid state communications* **126** (2003), no. 1-2 3–8.

[49] G. Zhang, S. Dai, N. Song, Z. Zhu, J. Zhang, W. Guo, D. Zhang, Z. Zhang, L. Xiao, and L. Lin, *The construction progress of a high-tc superconducting power substation in china*, *IEEE Transactions on Applied Superconductivity* **21** (June, 2011) 2824–2827.

[50] S. Manzeli, D. Ovchinnikov, D. Pasquier, O. V. Yazyev, and A. Kis, *2D transition metal dichalcogenides*, *Nature Reviews Materials* **2** (Aug., 2017) 17033.

[51] D. Pines, *Emergent behavior in strongly correlated electron systems*, *Reports on Progress in Physics* **79** (2016), no. 9 092501.

[52] T. Vicsek, *Complexity: The bigger picture*, *Nature* **418** (July, 2002) 131, [`arXiv:1006.5944`].

[53] P. W. Anderson, *More is different*, *Science* **177** (1972), no. 4047 393–396.

[54] G. R. Stewart, *Non-fermi-liquid behavior in d- and f-electron metals*, *Rev. Mod. Phys.* **73** (Oct, 2001) 797–855.

[55] E. J. W. Verwey, *Electronic Conduction of Magnetite (Fe_3O_4) and its Transition Point at Low Temperatures*, *Nature* **144** (Aug., 1939) 327–328.

[56] E. Wigner, *On the interaction of electrons in metals*, *Phys. Rev.* **46** (Dec, 1934) 1002–1011.

[57] Z. Lenac and M. Šunjić, *Melting of the wigner lattice at $T = 0$*, *Phys. Rev. B* **52** (Oct, 1995) 11238–11247.

[58] Y. Tomioka, A. Asamitsu, Y. Moritomo, H. Kuwahara, and Y. Tokura, *Collapse of a charge-ordered state under a magnetic field in* $\mathrm{pr}_{1/2}\mathrm{sr}_{1/2}\mathrm{mno}_3$, *Phys. Rev. Lett.* **74** (Jun, 1995) 5108–5111.

[59] C. H. Chen and S.-W. Cheong, *Commensurate to incommensurate charge ordering and its real-space images in* $\mathrm{la}_{0.5}\mathrm{ca}_{0.5}mn\mathrm{o}_3$, *Phys. Rev. Lett.* **76** (May, 1996) 4042–4045.

[60] C. Renner, G. Aeppli, B. G. Kim, Y.-A. Soh, and S. W. Cheong, *Atomic-scale images of charge ordering in a mixed-valence manganite*, *Nature* **416** (04, 2002) 518–521.

[61] E. Dagotto, T. Hotta, and A. Moreo, *Colossal magnetoresistant materials: the key role of phase separation*, *Physics Reports* **344** (2001), no. 13 1 – 153.

[62] H. Guo, W. Schmidt, L. H. Tjeng, and A. C. Komarek, *Charge correlations in cobaltates la2xsrx coo4*, *physica status solidi (RRL) Rapid Research Letters* **9** (2015), no. 10 580–582.

[63] Y. Ikeda, S. Suzuki, T. Nakabayashi, H. Yoshizawa, T. Yokoo, and S. Itoh, *Transport and thermodynamic studies of stripe and checkerboard ordering in layered nickel oxides r2xsrxnio4 (r = la and nd)*, *Journal of the Physical Society of Japan* **84** (2015), no. 2 023706.

[64] S.-H. Lee and S.-W. Cheong, *Melting of quasi-two-dimensional charge stripes in* $\mathrm{la}_{5/3}\mathrm{sr}_{1/3}\mathrm{nio}_4$, *Phys. Rev. Lett.* **79** (Sep, 1997) 2514–2517.

[65] J. Zhang, Y.-S. Chen, D. Phelan, H. Zheng, M. R. Norman, and J. F. Mitchell, *Stacked charge stripes in the quasi-2d trilayer nickelate la4ni3o8*, *Proceedings of the National Academy of Sciences* **113** (2016), no. 32 8945–8950.

[66] J. Li, H. Chen, H. Zhang, H. Yu, Y. Shi, L. Liu, H. Tian, Y. Zhu, and J. Tranquada, *Structural properties and charge ordered states in {RMnO3} (r=la, pr, nd, ca, sr) and (la, sr)2nio4*, *Micron* **35** (2004), no. 6 419 – 424. International Wuhan Symposium on Advanced Electron Microscopy.

[67] D. Jérome, *Organic conductors: from charge density wave ttftcnq to superconducting (tmtsf)2pf6*, *Chemical Reviews* **104** (2004), no. 11 5565–5592.

[68] K. Hiraki and K. Kanoda, *Wigner crystal type of charge ordering in an organic conductor with a quarter-filled band:* $(\mathrm{DI}-\mathrm{DCNQI})_2\mathrm{Ag}$, *Phys. Rev. Lett.* **80** (May, 1998) 4737–4740.

[69] C. Hotta, *Theories on frustrated electrons in two-dimensional organic solids*, *Crystals* **2** (2012), no. 3 1155.

[70] S. Kaiser, M. Dressel, Y. Sun, A. Greco, J. A. Schlueter, G. L. Gard, and N. Drichko, *Bandwidth tuning triggers interplay of charge order and superconductivity in two-dimensional organic materials*, *Phys. Rev. Lett.* **105** (Nov, 2010) 206402.

[71] M. Takano, J. Kawachi, N. Nakanishi, and Y. Takeda, *Valence state of the fe ions in sr1ylayfeo3*, *Journal of Solid State Chemistry* **39** (1981), no. 1 75 – 84.

[72] R. J. McQueeney, J. Ma, S. Chang, J.-Q. Yan, M. Hehlen, and F. Trouw, *Stabilization of charge ordering in* $\mathrm{la}_{1/3}\mathrm{sr}_{2/3}\mathrm{feo}_{3\text{-}\delta}$ *by magnetic exchange*, *Phys. Rev. Lett.* **98** (Mar, 2007) 126402.

[73] E. Morosan, H. W. Zandbergen, B. S. Dennis, J. W. G. Bos, Y. Onose, T. Klimczuk, A. P. Ramirez, N. P. Ong, and R. J. Cava, *Superconductivity in cuxtise2*, *Nat Phys* **2** (08, 2006) 544–550.

[74] H. Fjellvg, E. Gulbrandsen, S. Aasland, A. Olsen, and B. C. Hauback, *Crystal structure and possible charge ordering in one-dimensional ca3co2o6*, *Journal of Solid State Chemistry* **124** (1996), no. 1 190 – 194.

[75] Y. Shibata, S. Nishimoto, and Y. Ohta, *Charge ordering in the one-dimensional extended hubbard model: Implication to the tmttf family of organic conductors*, *Phys. Rev. B* **64** (Nov, 2001) 235107.

[76] J. M. Tranquada, B. J. Sternlieb, J. D. Axe, Y. Nakamura, and S. Uchida, *Evidence for stripe correlations of spins and holes in copper oxide superconductors*, *Nature* **375** (06, 1995) 561–563.

[77] Y. Kohsaka, C. Taylor, K. Fujita, A. Schmidt, C. Lupien, T. Hanaguri, M. Azuma, M. Takano, H. Eisaki, H. Takagi, S. Uchida, and J. C. Davis, *An intrinsic bond-centered electronic glass with unidirectional domains in underdoped cuprates*, *Science* **315** (03, 2007) 1380–1385.

[78] E. da Silva Neto, R. Comin, F. He, R. Sutarto, Y. Jiang, R. Greene, G. A. Sawatzky, and A. Damascelli, *Charge ordering in the electron-doped superconductor nd2xcexcuo4*, *Science* **347** (01, 2015).

[79] T. Y. Chien, L. Kourkoutis, J. Chakhalian, B. Gray, N. P. Kareev, N. P. Guisinger, D. A. Muller, and J. W. Freeland, *Visualizing short-range charge transfer at the interfaces between ferromagnetic and superconducting oxides*, *Nature Communication* (2013), no. 4 2336.

[80] I. M. Vishik, *Photoemission perspective on pseudogap, superconducting fluctuations, and charge order in cuprates: a review of recent progress*, *Reports on Progress in Physics* **81** (apr, 2018) 062501.

[81] A. Georges, G. Kotliar, W. Krauth, and M. J. Rozenberg, *Dynamical mean-field theory of strongly correlated fermion systems and the limit of infinite dimensions*, *Rev. Mod. Phys.* **68** (Jan, 1996) 13–125.

[82] U. Schollwöck, *The density-matrix renormalization group*, *Rev. Mod. Phys.* **77** (Apr, 2005) 259–315.

[83] A. N. Rubtsov, V. V. Savkin, and A. I. Lichtenstein, *Continuous-time quantum monte carlo method for fermions*, *Phys. Rev. B* **72** (Jul, 2005) 035122.

[84] N. Prokof'ev and B. Svistunov, *Bold diagrammatic monte carlo technique: When the sign problem is welcome*, *Phys. Rev. Lett.* **99** (Dec, 2007) 250201.

[85] R. J. Bartlett and M. Musiał, *Coupled-cluster theory in quantum chemistry*, *Rev. Mod. Phys.* **79** (Feb, 2007) 291–352.

[86] L. Reining, *The gw approximation: content, successes and limitations*, *Wiley Interdisciplinary Reviews: Computational Molecular Science* **8** (2018), no. 3 e1344, [`https://onlinelibrary.wiley.com/doi/pdf/10.1002/wcms.1344`].

[87] I. Kosztin, B. Faber, and K. Schulten, *Introduction to the diffusion monte carlo method*, *American Journal of Physics* **64** (1996), no. 5 633–644.

[88] Y. Yan and D. Blume, *Path integral monte carlo ground state approach: formalism, implementation, and applications*, *Journal of Physics B: Atomic, Molecular and Optical Physics* **50** (oct, 2017) 223001.

[89] A. N. Rubtsov, M. I. Katsnelson, A. I. Lichtenstein, and A. Georges, *Dual fermion approach to the two-dimensional hubbard model: Antiferromagnetic fluctuations and fermi arcs*, *Phys. Rev. B* **79** (Jan, 2009) 045133.

[90] J. Hubbard and B. H. Flowers, *Electron correlations in narrow energy bands*, *Proceedings of the Royal Society of London. Series A. Mathematical and Physical Sciences* **276** (1963), no. 1365 238–257, [`https://royalsocietypublishing.org/doi/pdf/10.1098/rspa.1963.0204`].

[91] A. Altland and B. D. Simons, *Condensed Matter Field Theory*. Cambridge University Press, 2 ed., 2010.

[92] A. Macridin, M. Jarrell, T. Maier, and G. A. Sawatzky, *Physics of cuprates with the two-band hubbard model: The validity of the one-band hubbard model*, *Phys. Rev. B* **71** (Apr, 2005) 134527.

[93] J. Quintanilla and C. Hooley, *The strong-correlations puzzle*, *Physics World* **22** (jun, 2009) 32–37.

[94] H. Terletska, T. Chen, J. Paki, and E. Gull, *Charge ordering and nonlocal correlations in the doped extended hubbard model*, *Phys. Rev. B* **97** (3, 2018) 115117.

[95] J. Paki, H. Terletska, S. Iskakov, and E. Gull, *Charge order and antiferromagnetism in the extended hubbard model*, *arXiv preprint arXiv:1904.02249* (2019).

[96] G. C. T. C. X. C. Q. D. L. G. J. G. R. I. S. I. J. P. E. G. Alexander Gaenko, Andrey E Antipov, *Updated core libraries of the alps project*, *Computer Physics Communications* **213** (2017) 235–251.

[97] A. G. J. K. I. K. R. L. J. L. H. S. S. T. T. C. X. C. J. P. F. L. J. E. P. H. T. M. T. E. G. Markus Wallerberger, Sergei Iskakov, *Updated core libraries of the alps project*, *arXiv preprint arXiv:1811.08331* (2018).

[98] P. K. V. V. Nukala, T. A. Maier, M. S. Summers, G. Alvarez, and T. C. Schulthess, *Fast update algorithm for the quantum monte carlo simulation of the hubbard model*, *Phys. Rev. B* **80** (Nov, 2009) 195111.

[99] M. Jarrell, *Maximum entropy analytic continuation of quantum monte carlo data*, *Lectures on the Physics of Strongly Correlated Systems XII* (2005).

[100] R. Levy, J. LeBlanc, and E. Gull, *Implementation of the maximum entropy method for analytic continuation*, *Computer Physics Communications* **215** (2017) 149 – 155.

[101] Z.-X. Li and H. Yao, *Sign-problem-free fermionic quantum monte carlo: Developments and applications*, *Annual Review of Condensed Matter Physics* **10** (2019), no. 1 337–356, [https://doi.org/10.1146/annurev-conmatphys-033117-054307].

[102] W. Metzner and D. Vollhardt, *Correlated lattice fermions in $d = \infty$ dimensions*, *Phys. Rev. Lett.* **62** (Jan, 1989) 324–327.

[103] M. H. Hettler, M. Mukherjee, M. Jarrell, and H. R. Krishnamurthy, *Dynamical cluster approximation: Nonlocal dynamics of correlated electron systems*, *Phys. Rev. B* **61** (May, 2000) 12739–12756.

[104] G. Baym and L. P. Kadanoff, *Conservation laws and correlation functions*, *Phys. Rev.* **124** (Oct, 1961) 287–299.

[105] E. Gull, M. Ferrero, O. Parcollet, A. Georges, and A. J. Millis, *Momentum-space anisotropy and pseudogaps: A comparative cluster dynamical mean-field analysis of the doping-driven metal-insulator transition in the two-dimensional hubbard model*, *Phys. Rev. B* **82** (Oct, 2010) 155101.

[106] P. W. Anderson, *Localized magnetic states in metals*, *Phys. Rev.* **124** (Oct, 1961) 41–53.

[107] R. Arita, S. Onari, K. Kuroki, and H. Aoki, *Off-site repulsion-induced triplet superconductivity: A possibility for chiral p_{x+y}-wave pairing in* $\mathrm{sr_2ruo_4}$, *Phys. Rev. Lett.* **92** (Jun, 2004) 247006.

[108] W. Wu and A.-M. S. Tremblay, *Phase diagram and fermi liquid properties of the extended hubbard model on the honeycomb lattice*, *Phys. Rev. B* **89** (May, 2014) 205128.

[109] G. Kotliar, S. Y. Savrasov, K. Haule, V. S. Oudovenko, O. Parcollet, and C. Marianetti, *Electronic structure calculations with dynamical mean-field theory*, *Reviews of Modern Physics* **78** (2006), no. 3 865.

[110] C. J. Geyer, *Introduction to markov chain monte carlo*, .

[111] N. Metropolis, A. W. Rosenbluth, M. N. Rosenbluth, A. H. Teller, and E. Teller, *Equation of State Calculations by Fast Computing Machines*, *JCP* **21** (June, 1953) 1087–1092.

[112] M. Troyer and U.-J. Wiese, *Computational complexity and fundamental limitations to fermionic quantum monte carlo simulations*, *Phys. Rev. Lett.* **94** (May, 2005) 170201.

[113] J. Skilling, *Maximum Entropy and Bayesian Methods.* Kluwer Academic, Dordrecht, 1989.

[114] R. K. Bryan, *Maximum entropy analysis of oversampled data problems*, *European Biophysics Journal* **18** (Apr, 1990) 165–174.

[115] N. D. Drummond, R. J. Needs, A. Sorouri, and W. M. C. Foulkes, *Finite-size errors in continuum quantum monte carlo calculations*, *Phys. Rev. B* **78** (Sep, 2008) 125106.

[116] S. Chiesa, D. M. Ceperley, R. M. Martin, and M. Holzmann, *Finite-size error in many-body simulations with long-range interactions*, *Phys. Rev. Lett.* **97** (Aug, 2006) 076404.

[117] *Twisted boundary conditions in lattice simulations*, *Physics Letters B* **609** (2005), no. 1 73 – 85.

[118] S. Freund and S. Teufel, *Peierls substitution for magnetic bloch bands*, *Analysis & PDE* **9.4** (2016) 773–811.

[119] R. Peierls, *Zur theorie des diamagnetismus von leitungselektronen*, *Zeitschrift fur Physik* **80** (Nov., 1933) 763–791.

[120] J. Ibanez-Azpiroz, A. Eiguren, A. Bergara, G. Pettini, and M. Modugno, *Breakdown of the peierls substitution for the haldane model with ultracold atoms*, *Phys. Rev. A* **90** (Sep, 2014) 033609.

[121] D. D. Betts, H. Q. Lin, and J. S. Flynn, *Improved finite-lattice estimates of the properties of two quantum spin models on the infinite square lattice*, *Canadian Journal of Physics* **77** (1999), no. 5 353–369, [`https://doi.org/10.1139/p99-041`].

[122] A. E. Antipov and I. Krivenko, *pomerol: 1.1*, .

[123] P. Leung, Z. Liu, E. Manousakis, M. Novotny, and P. E. Oppenheimer, *Density of states of the two-dimensional hubbard model on a 4× 4 lattice*, *Physical Review B* **46** (1992), no. 18 11779.

[124] S. A. Jafari, *Introduction to hubbard model and exact diagonalization*, *arXiv preprint arXiv:0807.4878* (2008).

[125] H. Alloul, *What is the simplest model that captures the basic experimental facts of the physics of underdoped cuprates?*, *Comptes Rendus Physique* **15** (2014), no. 6 519 – 524.

[126] A. Georges and G. Kotliar, *Hubbard model in infinite dimensions*, *Phys. Rev. B* **45** (Mar, 1992) 6479–6483.

[127] A. Georges, *Strongly correlated electron materials: Dynamical meanfield theory and electronic structure*, *AIP Conference Proceedings* **715** (2004), no. 1 3–74, [https://aip.scitation.org/doi/pdf/10.1063/1.1800733].

[128] X. Chen, J. P. F. LeBlanc, and E. Gull, *Superconducting fluctuations in the normal state of the two-dimensional hubbard model*, *Phys. Rev. Lett.* **115** (Sep, 2015) 116402.

[129] E. Gull, O. Parcollet, P. Werner, and A. J. Millis, *Momentum-sector-selective metal-insulator transition in the eight-site dynamical mean-field approximation to the hubbard model in two dimensions*, *Phys. Rev. B* **80** (Dec, 2009) 245102.

[130] T. Goto and B. Lthi, *Charge ordering, charge fluctuations and lattice effects in strongly correlated electron systems*, *Advances in Physics* **52** (2003), no. 2 67–118, [https://doi.org/10.1080/0001873021000057114].

[131] A. Damascelli, Z. Hussain, and Z.-X. Shen, *Angle-resolved photoemission studies of the cuprate superconductors*, *Rev. Mod. Phys.* **75** (Apr, 2003) 473–541.

[132] P. Battle, T. Gibb, and P. Lightfoot, *The crystal and magnetic structures of sr2lafe3o8*, *Journal of Solid State Chemistry* **84** (1990), no. 2 237 – 244.

[133] B. J. Sternlieb, J. P. Hill, U. C. Wildgruber, G. M. Luke, B. Nachumi, Y. Moritomo, and Y. Tokura, *Charge and magnetic order in* $la_{0.5}sr_{1.5}mno_4$, *Phys. Rev. Lett.* **76** (Mar, 1996) 2169–2172.

[134] B. Raveau and A. M. Seikh, *Charge ordering in cobalt oxides: Impact on structure, magnetic and transport properties*, *Z. Anorg. Allg. Chem.* **641** (2015).

[135] H. Chu, L. Zhao, A. de la Torre, T. Hogan, S. D. Wilson, and D. Hsieh, *A charge density wave-like instability in a doped spin–orbit-assisted weak mott insulator*, *Nature Materials* **16** (01, 2017) 200 EP –.

[136] J. Leshen, M. Kavai, I. Giannakis, Y. Kaneko, Y. Tokura, S. Mukherjee, W.-C. Lee, and P. Aynajian, *Emergent charge order near the doping-induced mott-insulating quantum phase transition in sr3ru2o7*, *Communications Physics* **2** (2019), no. 1 36.

[137] J. G. Bednorz and K. A. Müller, *Possible hightc superconductivity in the balacuo system*, *Zeitschrift für Physik B Condensed Matter* **64** (Jun, 1986) 189–193.

[138] D. JÉROME, *The physics of organic superconductors*, *Science* **252** (1991), no. 5012 1509–1514, [http://science.sciencemag.org/content/252/5012/1509.full.pdf].

[139] W. Yu, F. Zhang, F. Zamborszky, B. Alavi, A. Baur, C. A. Merlic, and S. E. Brown, *Electron-lattice coupling and broken symmetries of the molecular salt* $(\mathrm{TMTTF})_2\mathrm{sbf}_6$, *Phys. Rev. B* **70** (Sep, 2004) 121101.

[140] F. Nad and P. Monceau, *Dielectric response of the charge ordered state in quasi-one-dimensional organic conductors*, *Journal of the Physical Society of Japan* **75** (2006), no. 5 051005, [https://doi.org/10.1143/JPSJ.75.051005].

[141] N. Matsunaga, S. Hirose, N. Shimohara, T. Satoh, T. Isome, M. Yamomoto, Y. Liu, A. Kawamoto, and K. Nomura, *Charge ordering and antiferromagnetism in* $(tmttf)_2sbf_6$, *Phys. Rev. B* **87** (Apr, 2013) 144415.

[142] H. Seo, *Charge ordering in organic et compounds*, *Journal of the Physical Society of Japan* **69** (2000), no. 3 805–820, [https://doi.org/10.1143/JPSJ.69.805].

[143] M. Dressel and N. Drichko, *Optical properties of two-dimensional organic conductors: Signatures of charge ordering and correlation effects*, *Chemical Reviews* **104** (2004), no. 11 5689–5716, [https://doi.org/10.1021/cr030642f]. PMID: 15535665.

[144] R. H. McKenzie, J. Merino, J. B. Marston, and O. P. Sushkov, *Charge ordering and antiferromagnetic exchange in layered molecular crystals of the* θ *type*, *Phys. Rev. B* **64** (Aug, 2001) 085109.

[145] E. H. da Silva Neto, B. Yu, M. Minola, R. Sutarto, E. Schierle, F. Boschini, M. Zonno, M. Bluschke, J. Higgins, Y. Li, G. Yu, E. Weschke, F. He, M. Le Tacon, R. L. Greene, M. Greven, G. A. Sawatzky, B. Keimer, and A. Damascelli, *Doping-dependent charge order correlations in electron-doped cuprates*, *Science Advances* **2** (2016), no. 8 [https://advances.sciencemag.org/content/2/8/e1600782.full.pdf].

[146] **Simons Collaboration on the Many-Electron Problem** Collaboration, M. Motta, D. M. Ceperley, G. K.-L. Chan, J. A. Gomez, E. Gull, S. Guo, C. A. Jiménez-Hoyos, T. N. Lan, J. Li, F. Ma, A. J. Millis, N. V. Prokof'ev, U. Ray, G. E. Scuseria, S. Sorella, E. M. Stoudenmire, Q. Sun, I. S. Tupitsyn, S. R. White, D. Zgid, and S. Zhang, *Towards the solution of the many-electron problem in real materials: Equation of state of the hydrogen chain with state-of-the-art many-body methods*, *Phys. Rev. X* **7** (Sep, 2017) 031059.

[147] O. Gunnarsson, T. Schäfer, J. P. F. LeBlanc, E. Gull, J. Merino, G. Sangiovanni, G. Rohringer, and A. Toschi, *Fluctuation diagnostics of the electron self-energy: Origin of the pseudogap physics*, *Phys. Rev. Lett.* **114** (Jun, 2015) 236402.

[148] W. Wu, M. Ferrero, A. Georges, and E. Kozik, *Controlling feynman diagrammatic expansions: Physical nature of the pseudogap in the two-dimensional hubbard model*, *Phys. Rev. B* **96** (Jul, 2017) 041105.

[149] B.-X. Zheng, C.-M. Chung, P. Corboz, G. Ehlers, M.-P. Qin, R. M. Noack, H. Shi, S. R. White, S. Zhang, and G. K.-L. Chan, *Stripe order in the underdoped region of the two-dimensional hubbard model*, *Science* **358** (2017), no. 6367 1155–1160, [`http://science.sciencemag.org/content/358/6367/1155.full.pdf`].

[150] M. H. Hettler, A. N. Tahvildar-Zadeh, M. Jarrell, T. Pruschke, and H. R. Krishnamurthy, *Nonlocal dynamical correlations of strongly interacting electron systems*, *Phys. Rev. B* **58** (Sep, 1998) R7475–R7479.

[151] S. Fuchs, E. Gull, M. Troyer, M. Jarrell, and T. Pruschke, *Spectral properties of the three-dimensional hubbard model*, *Phys. Rev. B* **83** (Jun, 2011) 235113.

[152] E. Gull, P. Werner, O. Parcollet, and M. Troyer, *Continuous-time auxiliary-field monte carlo for quantum impurity models*, *EPL (Europhysics Letters)* **82** (2008), no. 5 57003.

[153] D. Medvedeva, S. Iskakov, F. Krien, V. V. Mazurenko, and A. I. Lichtenstein, *Exact diagonalization solver for extended dynamical mean-field theory*, *Phys. Rev. B* **96** (Dec, 2017) 235149.

[154] T. Ayral, S. Biermann, P. Werner, and L. Boehnke, *Influence of fock exchange in combined many-body perturbation and dynamical mean field theory*, *Phys. Rev. B* **95** (Jun, 2017) 245130.

[155] U. Wolff, *Saddle point mean field calculation in the hubbard model*, *Nuclear Physics B* **225** (1983), no. 3 391 – 408.

[156] X.-Z. Yan, *Theory of the extended hubbard model at half filling*, *Phys. Rev. B* **48** (Sep, 1993) 7140–7147.

[157] E. G. C. P. van Loon, M. I. Katsnelson, and M. Lemeshko, *Ultralong-range order in the fermi-hubbard model with long-range interactions*, *Phys. Rev. B* **92** (Aug, 2015) 081106.

[158] M. Schüler, E. G. C. P. van Loon, M. I. Katsnelson, and T. O. Wehling, *First-order metal-insulator transitions in the extended Hubbard model due to self-consistent screening of the effective interaction*, *ArXiv e-prints* (June, 2017) [`arXiv:1706.09644`].

[159] E. Morosan, H. W. Zandbergen, B. S. Dennis, J. W. G. Bos, Y. Onose, T. Klimczuk, A. P. Ramirez, N. P. Ong, and R. J. Cava, *Superconductivity in cuxtise2*, *Nature Physics* **2** (07, 2006) 544 EP –.

[160] K. C. D. Beach, *Identifying the maximum entropy method as a special limit of stochastic analytic continuation*, *arXiv:cond-mat/0403055* (2005).

[161] A. I. Lichtenstein and M. I. Katsnelson, *Antiferromagnetism and* $\boldsymbol{d}$ *-wave superconductivity in cuprates: A cluster dynamical mean-field theory*, *Phys. Rev. B* **62** (Oct, 2000) R9283–R9286.

[162] T. A. Maier, M. Jarrell, T. C. Schulthess, P. R. C. Kent, and J. B. White, *Systematic study of d-wave superconductivity in the 2d repulsive hubbard model*, *Phys. Rev. Lett.* **95** (Nov, 2005) 237001.

[163] J. Merino and R. H. McKenzie, *Superconductivity mediated by charge fluctuations in layered molecular crystals*, *Phys. Rev. Lett.* **87** (Nov, 2001) 237002.

[164] X.-Z. Yan, *Theory of the extended hubbard model at half filling*, *Phys. Rev. B* **48** (Sep, 1993) 7140–7147.

[165] K. Haule, *Quantum monte carlo impurity solver for cluster dynamical mean-field theory and electronic structure calculations with adjustable cluster base*, *Phys. Rev. B* **75** (Apr, 2007) 155113.

[166] E. Gull, P. Werner, X. Wang, M. Troyer, and A. J. Millis, *Local order and the gapped phase of the hubbard model: A plaquette dynamical mean-field investigation*, *EPL (Europhysics Letters)* **84** (2008), no. 3 37009.

[167] T. A. Maier, M. Jarrell, T. C. Schulthess, P. R. C. Kent, and J. B. White, *Systematic study of d-wave superconductivity in the 2d repulsive hubbard model*, *Phys. Rev. Lett.* **95** (Nov, 2005) 237001.

[168] P. Staar, T. A. Maier, and T. C. Schulthess, *Efficient non-equidistant FFT approach to the measurement of single- and two-particle quantities in continuous time quantum monte carlo methods*, *Journal of Physics: Conference Series* **402** (dec, 2012) 012015.

[169] P. Staar, T. Maier, and T. C. Schulthess, *Dynamical cluster approximation with continuous lattice self-energy*, *Phys. Rev. B* **88** (Sep, 2013) 115101.

[170] P. Haase, S.-X. Yang, T. Pruschke, J. Moreno, and M. Jarrell, *Dual-fermion approach to the anderson-hubbard model*, *Phys. Rev. B* **95** (Jan, 2017) 045130.

[171] H. Hafermann, G. Li, A. N. Rubtsov, M. I. Katsnelson, A. I. Lichtenstein, and H. Monien, *Efficient perturbation theory for quantum lattice models*, *Phys. Rev. Lett.* **102** (May, 2009) 206401.

[172] E. G. C. P. van Loon, M. I. Katsnelson, and H. Hafermann, *Second-order dual fermion approach to the mott transition in the two-dimensional hubbard model*, *Phys. Rev. B* **98** (Oct, 2018) 155117.

[173] A. E. Antipov, J. P. LeBlanc, and E. Gull, *Opendf - an implementation of the dual fermion method for strongly correlated systems*, *Physics Procedia* **68** (2015) 43 – 51. Proceedings of the 28th Workshop on Computer Simulation Studies in Condensed Matter Physics (CSP2015).

[174] A. Rubtsov, M. Katsnelson, and A. Lichtenstein, *Dual boson approach to collective excitations in correlated fermionic systems*, *Annals of Physics* **327** (2012), no. 5 1320–1335.

[175] C. Jung, A. Lieder, S. Brener, H. Hafermann, B. Baxevanis, A. Chudnovskiy, A. Rubtsov, M. Katsnelson, and A. Lichtenstein, *Dual-fermion approach to non-equilibrium strongly correlated problems*, *Annalen der Physik* **524** (2012), no. 1 49–61, [https://onlinelibrary.wiley.com/doi/pdf/10.1002/andp.201100045].

[176] K. A. Takemori, N. and H. Hafermann, *Intersite electron correlations on inhomogeneous lattices a real-space dual fermion approach*, *arXiv preprint arXiv:1801.02441* (2018).

[177] E. G. C. P. van Loon, H. Hafermann, and M. I. Katsnelson, *Precursors of the insulating state in the square-lattice hubbard model*, *Phys. Rev. B* **97** (Feb, 2018) 085125.

[178] T. Ayral and O. Parcollet, *Mott physics and spin fluctuations: A functional viewpoint*, *Physical Review B* **93** (2016), no. 23 235124.

[179] *Path integrals and dual fermions*, .

[180] H. Hafermann, F. Lechermann, A. N. Rubtsov, M. I. Katsnelson, A. Georges, and A. I. Lichtenstein, *Strong electronic correlations: Dynamical mean-field theory and beyond*, in *Modern Theories of Many-Particle Systems in Condensed Matter Physics*, pp. 145–214. Springer, 2012.

[181] S. Iskakov, A. E. Antipov, and E. Gull, *Diagrammatic monte carlo for dual fermions*, *Phys. Rev. B* **94** (Jul, 2016) 035102.

[182] M.-T. Philipp, M. Wallerberger, P. Gunacker, and K. Held, *Mott-hubbard transition in the mass-imbalanced hubbard model*, *The European Physical Journal B* **90** (Jun, 2017) 114.